Solid-State Multimission Magnetometer (SSM^3): Application to Groundwater Exploration on Mars

FINAL REPORT

Submitted by

Blackhawk Geoservices, Inc.
301 B Commercial Rd.
Golden, CO 80401

Submitted to

Planetary Instrument Definition and Design Program
National Aeronautics and Space Administration
300 E Street SW
Washington, DC 20546

Contract NASW-98019

January 28, 2002

1. SUMMARY

This project sought (1) to develop spin-dependent tunneling (SDT) magnetic sensors into useful wideband magnetometers, (2) to develop a high-impedance electrometer for electric-field measurements at very resistive planetary surfaces, and (3) to develop an understanding of how to apply electric- and magnetic-field measurements to EM sounding for groundwater on Mars.

Magnetoresistance is a change in the electrical resistance of a material as a function of an externally applied magnetic field. Magnetoresistive sensors are now commonly used in industry, especially magnetic disk read-write heads. The latest generation of these devices operates using quantum-mechanical tunneling (SDT). A principal goal was to improve the noise floor and bandwidth of SDT devices and indeed during the course of this project nearly two orders of magnitude improvement was achieved. The sensitivity of the devices to temperature fluctuations and radiation was also characterized. While SDTs have been shown to give useful responses over a wider bandwidth (mHz – MHz) than any other single sensor, they still cannot outperform sensors designed for particular niche bands. Further improvement to the noise floor of SDTs can likely be achieved with better selection of materials and better control on their construction.

Geophysical electric-field measurements are routinely made using grounded metal stakes or porous electrolyte pots, but such galvanic contact will be impossible at extremely dry, electrically resistive surface of Mars. A prototype electrometer was constructed under this project that features a shielded-plate electrode that is driven with the output of the first stage of the input amplifier, forming a voltage-follower circuit. In this way input impedances up to 300 GΩ are transformed to an acceptable level in a near-unity gain amplifier. Related methods have been used in resistive ground in Antarctica. This prototype can be viewed as transitional between the traditional large-offset grounded electrodes and fully noncontacting, weakly galvanic to capacitative measurements necessary at the surface of Mars.

Theoretical modeling of rock-ice-water mixtures indicates that groundwater on Mars can be readily detected using either artificial- or natural-source EM methods; the optimal bandwidth is 100 Hz – 1 kHz, although signatures of water can span the interval from 10 mHz to >10 kHz. Abundant natural EM sources for passive (sensor-only) soundings likely exist on Mars, although their exact nature and distribution will affect the ability to resolve groundwater. Artificial-source methods offer higher signal-to-noise at the cost of modestly increased mass and power. Low-frequency EM methods can provide the "ground truth" in a 2007 launch to follow up on inferences from orbital radars currently planned for the 2003 and 2005 opportunities.

2. TABLE OF CONTENTS

3. INTRODUCTION

Electromagnetic-field measurements are fundamental to space exploration and utilization. Magnetometers and electrometers are principal tools in space physics for studying the solar wind, planetary magnetospheres and ionospheres, and the mutual interactions of these structures. In solid-earth geophysics, electromagnetic fields play important roles in understanding the geodynamo, crustal formation, and geoelectric sections. The last in turn constrains the compositional and thermal structure of planetary interiors. Striking recent work in planetary magnetic fields includes the discovery of strong crustal remanance on Mars (*Acuña et al.*, 1999) and the inference of an electrically conductive ocean beneath one or more of the galilean satellites of Jupiter (*Khurana et al.*, 1998). Magnetometers are also used for economical attitude sensing of earth-orbiting spacecraft (e.g., *Eterno et al.*, 1992).

Many magnetic fields are time-variable and so magnetometer frequency response is important. Fluxgate and vapor/liquid instruments responding in the ULF band (say, < 10 Hz) adequately map the structures of ionospheres and magnetospheres, as well as "DC" components like crustal magnetism. However, characteristic plasma frequencies commonly exceed 10 kHz in planetary magnetospheres; synchrotron radiation from Jupiter extends to near 10 GHz (*Carr et al.*, 1983). In practice, plasma responses are measured by electric-field and particle detectors. Geoelectric soundings depend strongly on broadband measurement of magnetic fields, as the effective penetration, or skin depth, is inversely proportional to the square root of frequency. Natural-field geoelectric soundings use frequencies varying from ULF to VLF (approx 1 mHz to 10 kHz), whereas artificial-source surveys can exploit frequencies >100 kHz for shallow soundings. Magnetic fields from geoelectric soundings are typically measured with large induction coils.

Magnetometry as a whole is considered very mature because existing instruments are good at making niche measurements in specialized areas of investigation. A revolutionary advance would engender an instrument capable of multiple investigations, i.e., one with a very broadband frequency response and dynamic range. At the same time, such an instrument should achieve order-of-magnitude reductions in mass, volume, and power. Such compact instruments will be especially important in a next generation of small, networked spacecraft (an orbiting constellation or tiny hard-landers like DS-2) that would study planetary magnetic fields on a global scale. Indeed, the size and mass constraints on such spacecraft could be so tight that an extendable boom might be prohibited, thus raising the level of magnetic noise. The MGS spacecraft has already faced this restriction; with its magnetometers on the solar panels, noise levels are ~0.3 nT (M. Acuña, personal communication, 2000). If the magnetometers were truly small (10s g), then several could be distributed around the spacecraft and allow a difference-mode rejection filter or even better direct modeling of the spacecraft fields.

A revolutionary magnetometer that could respond to 1 MHz and above would open up entirely new avenues of investigation at radio frequencies that were previously measured only by electric antennae. For example, a magnetometer with a 1 pT high-frequency noise floor could detect a 1 W radiated signal at a distance of 30 m. This could allow the receivers of ground-penetrating radars to be much more compact, or at least provide complementary magnetic-field information that can both help eliminate noise and better constrain the subsurface. Similarly, magnetic-field measurements at plasma frequencies could be made, and Jupiter's radioburst emissions at 1-10 MHz (*Carr et al.*, 1983) would be detectable to distances of 1-10 million km.

The fluxgate magnetometer is firmly established as the standard instrument for spacecraft vector measurements. Fluxgates typically have masses of a few to several kilograms and consume a few hundred milliwatts or more of power at full duty. Noise levels are a few pT/$\sqrt{\text{Hz}}$ at 1 Hz which is equivalent to a few pT RMS noise in a 1-Hz bandwidth (unless otherwise stated, all field levels will henceforth be reported as RMS values in a 1-Hz bandwidth at 1 Hz). Fluxgates are made considerably smaller for covert surveillance of people and vehicles at the expense of degraded performance: masses of tens of grams, volumes <100 cm^3, power consumption ~10 mW, and noise ~0.1 nT.

Most fluxgates are restricted to low frequencies, typically less than 100 Hz, because they are actively driven to saturation by coils at frequencies of a kilohertz or so. Large (~1 m long, 10-cm diameter, 10 kg) coils are used for broadband measurements in terrestrial geoelectric sounding. However, two or three different, specialized coils may be necessary to span this large bandwidth. At high frequency, they have noise floors comparable to SQUIDS (~ 10 fT/$\sqrt{\text{Hz}}$) and RMS noise at 1 Hz ~0.1-1 pT. But again, performance can be traded off against size: as the noise floor is roughly inversely proportional to both coil weight and diameter for the same bandwidth (*Becker*, 1967), a compact (~10 g, 10 cm^3) coil would have RMS noise of ~0.1-1 nT at 1 Hz.

Therefore it is apparent that miniaturized fluxgate magnetometers and/or induction coils can achieve broadband sensing of magnetic fields, albeit at reduced performance. There are several drawbacks to this approach, however. The different instruments have different frequency-noise characteristics and dynamic ranges. Furthermore, a composite instrument with several individual sensors would be needed, one such group for each axis, and could require additional separation or shielding to prevent interference. Some savings in redundancy may be acheived by using the excitation coil of the fluxgate as a search coil, but the scaling relations above indicate that this very small, light coil will have a high noise floor.

Other options are limited for broadband magnetometers with reduced size, mass, and power. APL's New Millenium xylophone magnetometer, based on Lorenz-force deflection, is expected to have 1 nT noise and weigh 10s g, yet requires 200 mW (M. Buehler, personal communication, 1997). Like a fluxgate, it is driven by a kHz-range AC signal and therefore offers no greater bandwidth but with power consumption comparable to a full-scale fluxgate, not a compact one. The mirror-image differential induction-amplitude magnetometer (MIDIM; *Henkel*, 1999) has not yet reached the market, but appears to be a proprietary improvement on the fluxgate design. The device is not yet miniaturized to the chip level. SQUIDs have long been considered the ultimate magnetometer; with the advent of "high" temperature superconducting (HTS) SQUIDS, geophysical interest in these sensors has renewed (e.g., *Foley et al.*, 1999). As these devices are operated on Earth in a refrigerated dewar at the temperature of liquid nitrogen (77 K), the same performance can be achieved during daylight without a dewar only at distances well beyond Saturn. Massive passive cooling could be used at the expense of degraded performance. Liquid/vapor magnetometers (proton precession, alkali-vapor) measure the total field and not its vector components; furthermore, they are not well suited to order-of-magnitude miniaturization due to their high power use and the relatively large sensor volume required.

One technology that shows promise for measuring the full geophysical bandwidth in a single sensor, with breakthrough size, mass, and power, is *magnetoresistance*, specifically, spin-

dependent tunneling (SDT). The first goal of this project was to fabricate a general, prototype, solid-state magnetometer using newly developed magnetoresistive thin films.

Low-frequency electric-field measurements on electrically resistive planetary surfaces pose unique problems. High-frequency electric fields (those that radiate in the medium; see Section 6.3.1) are measured with resonant antennae, such as the classic half-wavelength dipole. The high-frequency regime is also called "capacitatively coupled." Also note that in propagation there is equal energy in the electric and magnetic field and is usually simply more convenient to measure the electric-field component. In the earth, low-frequency electric fields (those that diffuse; again see Section 6.3.1) are commonly measured on the ground by inserting two metal stakes or electrolyte "pots" into the ground; the component of the electric field along the direction of the two measurement points is the voltage difference divided by the separation. The low-frequency regime is also called "galvanically coupled." In space, low-frequency electric fields in plasmas are measured with a double Langmuir probe: two long booms of a resistive material have conductive ends. This is also a galvanically coupled measurement. In electrically resistive ground such as Antarctica, efficient galvanic contact cannot be made and systems must adapt between galvanically and capacitatively coupled measurements (*Wannamaker et al.*, 19xx). Development of a prototype electrometer for application on resistive planetary surfaces, particularly Mars, was the second goal of this project.

New magnetometers and electrometers may have many uses in space science, but our principal application is for electromagnetic sounding to detect subsurface, liquid water on Mars. This has been identified as a key exploration goal, crosscutting themes for geology, climate, life, and resources (*MEPAG, 2001*). Although orbital radars are presently planned to attempt to detect subsurface water on Mars, there are many potential pitfalls with these high-frequency methods, principally potential strong losses due to absorption, scattering and multiple reflection, and contrasts in dielectric constant that are small compared with those in electrical conductivity. Low-frequency sounding techniques designed to measure electrical conductivity are well-established in geophysical exploration for groundwater on Earth (see *McNeill*, 1990, for a review) and this legacy can be applied to Mars. The third goal of this project was to develop the broad theoretical framework necessary to design experiments for low-frequency electromagnetic sounding for groundwater on Mars. Essentially the entire field of inductive EM on Mars required some initial investigation, including the predicted response of the planet, the applicability different sensors, the likelihood of natural sources, and the resources (size, mass, power) required for natural- vs. artificial-source soundings. As these methods are relatively new to solid-earth planetary science, there is some tutorial review as well. The first objective of this section is to determine the key frequency ranges for detecting subsurface water on Mars as functions of depth, thickness, and salinity. Both natural- and artificial-source methods are considered, with recommendations on optimum methods, sensors, and platforms.

References

Acuña, M.H., and 12 others (1999). Global distribution of crustal magnetism discovered by Mars Global Surveyor MAG/ER experiment, *Science, 284*, 790-793.

Baibach, M.N., et al. 1988. Giant magneto-resistance of (001)Fe/(001)Cr superlattices. *Phys. Rev. Lett., 61*, 2472-2475.

Becker, A., Design formulas for electromagnetic sensing coils (1967). *Geoexploration, 5*, 81-88.

Brown, J. 1994. GMR materials: theory and applications. *Sensors, nr. 9*, 42-48.

Carr, T.D., M.D. Desch, and J.K. Alexander (1983). Phenomelology of magnetospheric radio emissions, in *Physics of the Jovian Magnetosphere* (ed. A.J. Dessler), Cambridge, pp 226-316.

Eterno, J.S., R.O. Zermuehlen, H.F. Zimbelman (1999). Attitude Determination and Control, in *Space Mission Analysis and Design* (eds. W.J. Larson and J.R. Wertz), Microcosm/Kluwer, pp. 340-366.

Foley, C.P., and 21 others (1999). Field trials using HTS SQUID magnetometers for ground-based and airborne geophysical applications, *IEEE Trans. Appl. Supercond., 9*, 3786.

Henkel (1999) "Mini magnetometer measures flux strength and direction," *Sensors, Aug. 99*, 6-7.

Khurana, K.K., and 6 others (1998). Induced magnetic fields as evidence for subsurface oceans in Europa and Callisto, *Nature, 395*, 777-780.

Moodera, J.S., L. Kinder, T. Wong, and R. Meservey (1995). Large magnetoresistance at room temperature in ferromagnetic thin film tunnel junctions, *Phys. Rev. Lett., 74*, 3273-3276.

Moodera, J.S., J. Nassar, and G. Mathon (1999). Spin tunneling in ferromagnetic junctions, *Ann. Rev. Mater. Sci., 29*, 381-432.

Russell, C.T., and R.J. Walker (1995). The magnetospheres of the outer planets, in *Introduction to Space Physics* (eds. M.G. Kivelson and C.T. Russell), Cambridge, pp. 503-520.

4. SPIN-DEPENDENT TUNNELLING (SDT) MAGNETOMETER

This work described in this section was carried out by Nonvolatile Electronics, Inc. (NVE) of Eden Prairie, MN, by Dr. Mark Tondra, Dr. Dan Reed, and Mr. Erik Lange under a subcontract to this grant. The PI prepared the comparison of SDTs to other magnetic-field sensors (Figure 4.9).

4.1 Overview of SDT Magnetic Sensors

Magnetoresistance is the change in the electrical resistance of materials as a function of an externally applied magnetic field. There are many forms of magnetoresistance, but the most useful ones are observed in ferromagnetic thin films, usually alloys of Ni Fe, and Co. These effects are useful because magnetoresistive thin films can be manufacturable in an integrated circuit process. They can be deposited on semiconductor wafers (with or without integrated circuits) and patterned into many forms of devices using standard photolithography and etching techniques. Resulting magnetoresistive products, then, benefit from the same commercial forces that have made integrated circuits so valuable and successful. They are extremely small, very low cost, and are easily combined with many electronic functions.

The easy combination with electronics is the key to what makes magnetoresistive thin films so important. The same underlying technology can be applied to many different applications. Examples are: generic linear magnetic field sensors; special function magnetic field sensors; read heads for computer disk drives, magnetic tapes, credit cards, currency, etc.; current sensing, digital data transmission isolation, and digital data storage. There are many details that must be addressed in order to have a successful device in any of these categories. The size of the magnetotransducer will vary, as will the circuit complexity, packaging, power requirements, cost, etc. But the basic magnetoresistive effect is common to all of them.

4.1.1 Physics Background

4.1.1.1. AMR The understanding of the physics of magnetoresistance in ferromagnetic materials goes back as far as 1857 when the Anisotropic Magnetoresistance (AMR) effect was first discovered in macroscopic ferromagnetic wires [1]. The AMR effect is observed as a relationship between the resistance of the material and the angle between the magnetization vector and the electrical current. The resistance is lowest when the current and magnetization are perpendicular and maximum when they are parallel/antiparallel. This effect is observable in bulk materials and in thin films. The magnitiude of the effect can be as large as 8% at room temperature. However, the AMR effect in the most commonly used materials is between 2% and 4%. The main tradeoffs involved are the desire to have low saturation fields, low hysteresis, low magnetostriction, and high linearity; while still maintaining high magnetoresistance. The most popular material for this compromise is the $Ni_{65}Fe_{15}Co_{20}$ (atomic percentage).

The physical origins of the AMR effect are "spin-orbit" interactions, and to the imbalance of spin-up and spin-down conduction (Fermi energy) electrons. The spin orbit interactions lead to non-equal scattering of spin up and spin down electrons. The net spin imbalance at the Fermi surface creates an unbalance of the scattering result. These two effects together result in a resistivity that varies with the orientation of magnetization with respect to electrical current. Detailed explanations of observed resistivity variations have been largely worked out by Smit [2] and others.

4.1.1.2. GMR The development of thin film deposition technology led to AMR sensors being the dominant technology for the read heads in hard disk drives. This dominance remained until the mid 1990's when Giant Magnetoresistive (GMR) devices took over. The GMR effect is fundamentally a thin film phenomenon. It is empirically observed to be a change in resistance as a function of the angle between the magnetizations of adjacent thin ferromagnetic thin films. Consider the simplest case of two thin NiFeCo ferromagnetic films separated by a thin Cu "spacer" layer (this structure is referred to as a "sandwich"). These films must not be in direct contact with each other or else their magnetizations will be directly coupled, and will not be able to rotate with respect to each other. However, they may not be separated by too much distance, or the electrons flowing in the sandwich will not be able to pass from one ferromagnetic layer to the other without loosing their "spin information". Typical dimensions for such a GMR sandwich are NiFeCo 5 / Cu 3.5 / NiFeCo 5 (thicknesses in nm). The thicknesses must be small compared to the effective scattering lengths of conduction electrons. The GMR effect can be observed with current flowing either in the plane of the thin films or perpendicular to it. Practically speaking, however, devices are made using the Current In the Plane (CIP) configuration because the Current Perpendicular to the Plane (CPP) configuration has a very low resistance unless the lateral dimensions can be made extremely small (~10 nm).

From a developmental standpoint, the discovery of GMR was not possible before vacuum deposition technology advanced to the point where layer thicknesses and roughnesses could be controlled to sub-nanometer dimensions. The usually cited discoverers of GMR were pushing on this technology in their search for magnetoresistive effects [3] and exchange coupling in magnetic multilayers [4].

Since these discoveries in the late 1980's, GMR has rapidly evolved to surpass AMR as the dominant magnetoresistive effect used in hard drive read heads in the mid 1990's. The basic read head structure is called a "spin valve." It is a sandwich as described above with one of the two magnetic layers "pinned" by an antiferromagnetic layer such as FeMn, or CrPtMn. A simple example of a spin valve structure is NiFeCo 5 / Cu 3.5 / CoFe 5 / CrPtMn 30.

The thin layer structure is critical because the physical effect that is being exploited is that the spin up and spin down electrons in the sandwich have different mean free paths that depend on the orientation of the magnetizations. These mean free paths are on the order of 10 nm.

The magnetic operation of a spin valve is such that the resistance is maximized when the magnetic layers are antiparallel and minimized when they are parallel. The total magnitude of the spin valve GMR effect is 5% to 25% depending upon layer thickness, quality, and configuration.

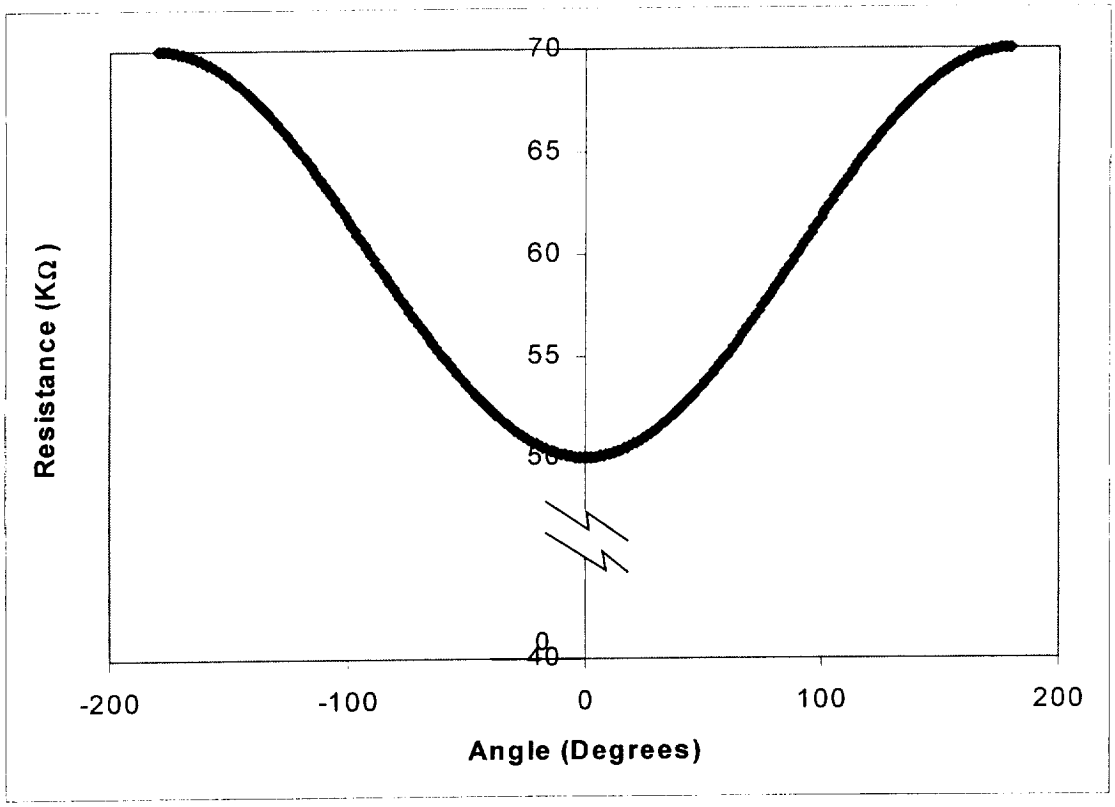

Figure 4.1. The resistance of a spin valve as a function of the angle between magnetizations of top and bottom magnetic layers. The high resistance values shown are more likely to be observed in a tunnel junction. The typical sheet resistance of a spin valve is about 25 ohms / square, so this data would be representative of a GMR spin valve with 2000. I.e. its length to width ratio is 2000.

4.1.1.3. SDT Spin Dependent Tunneling (SDT) devices are again related to the relative orientations of two adjacent ferromagnetic films. However, the tunneling effect takes place when electrons pass across a nominally insulating barrier separating the two magnetic layers. Thus it is strictly a CPP effect. The first useful SDT devices were demonstrated in 1995 [5,6], and the first one using lithographical fabrication techniques in 1996 [7]. The tunnel barrier must be extremely thin in order to have a measurable tunneling current. A typical SDT structure is NiFeCo 12.5 / Al_2O_3 1.5 / CoFe 50 / CrPtMn 30. Here, the Al_2O_3 tunnel barrier has replaced the Cu as the separating film in the spin valve. Magnetically, the operation of a pinned SDT device is identical to that of a GMR spin valve. The magnetoresistance, however, is larger. Total resistance changes on the order of 45% are common.

Tunnel junction devices are more difficult to fabricate than GMR devices. Two main challenges are the creation of the very thin tunnel barrier with no pinholes, and the subsequent formation of usable structures out of the initial blank tunnel sandwich layers.

At NVE, the SDT devices are made in a Perkin Elmer 2400 with a baseline pressure in the 10^{-8} torr. The layers are deposited using RF diode sputtering in an Ar plasma using an Ar pressure of 10's of mTorr. The Al_2O_3 barrier is formed by first depositing a 1.2nm layer of Al, and subsequently oxidizing it by introducing some oxygen into the chamber while a plasma is still present over the sample wafer. As it oxidizes, the Al film expands about 30% to its final thickness of about 1.5nm. One or more annealing steps are required to optimize the SDT devices' resistive and magnetic properties.

Patterning of the junctions takes place in two steps. The first step is to etch away portions of the top electrode material while leaving the entire bottom electrode intact. The second step is to etch away undesired bottom electrode material. Both etches are performed using an ion mill for material removal, and a photolithographically defined etch mask. The finished result is a stack where the edges of top electrodes are entirely within the edges of the bottom electrode. The bottom electrode can support one or two tunnel junctions depending upon the intended finished structure.

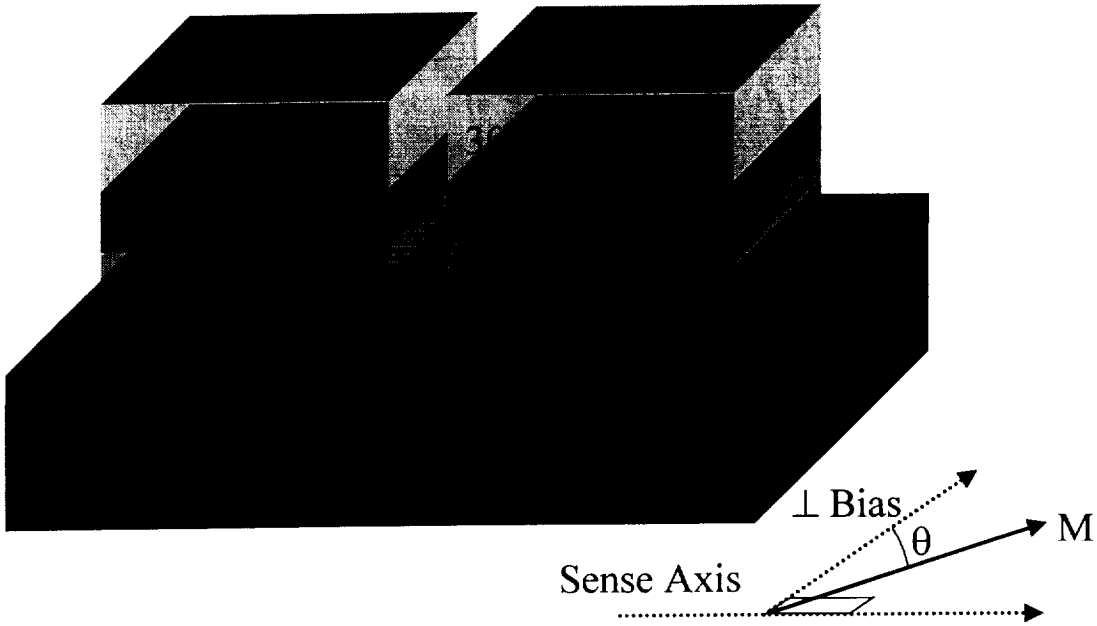

Figure 4.2: SDT material stack and magnetic biasing mode.

The two junction SDT structure allows a tighter packing of junctions in a given area, and makes fabrication slightly easier as all connections to junctions are to the top electrodes.

4.1.2 A Useful Sensor

In order for the junctions to be useful as magnetic field sensors, more is required. Such details are addressed here in the context of the SDT sensors. However, similar technology is also applied to GMR and AMR sensors.

4.1.2.1. Bridge Typically, a resistance bridge is desirable rather than a single resistor or string of resistors. A bridge allows for null readings, helps compensate for temperature effects, and makes amplifier design much easier. A typical bridge starts with four identical resistors on each of the four bridge legs. For the resistance bridge to do its job, however, features must be added to make some legs behave differently than others. If this is not done, all the legs' resistances will increase and decrease at the same rate, and no net output will be observed. The tool NVE uses most commonly to achieve a non-zero bridge output are flux concentrators.

4.1.2.2. Field biasing The SDT device response must be linearized. That is, the "square loop" output of an unbiased device must be turned into a linear, non-hysteretic output. The square loop

shape occurs when the free layer magnetization of the SDT junction flips back and forth to be parallel and antiparallel to the pinned layer. This output becomes much smoother when a perpendicular bias field is applied so that the soft layer magnetization rotates rather than flips. The magnitude of the perpendicular bias field is just over the anisotropy field of the soft layer. This is about 18 Oe in NiFeCo, and less than 5 Oe in regular permalloy ($Ni_{80}Fe_{20}$). In the finished devices, the perpendicular field is generated by an on-chip planar coil. A second coil is also provided as a sensitive axis bias. The difference in biased and unbiased SDT response is seen in Figures 4.3 and 4.4.

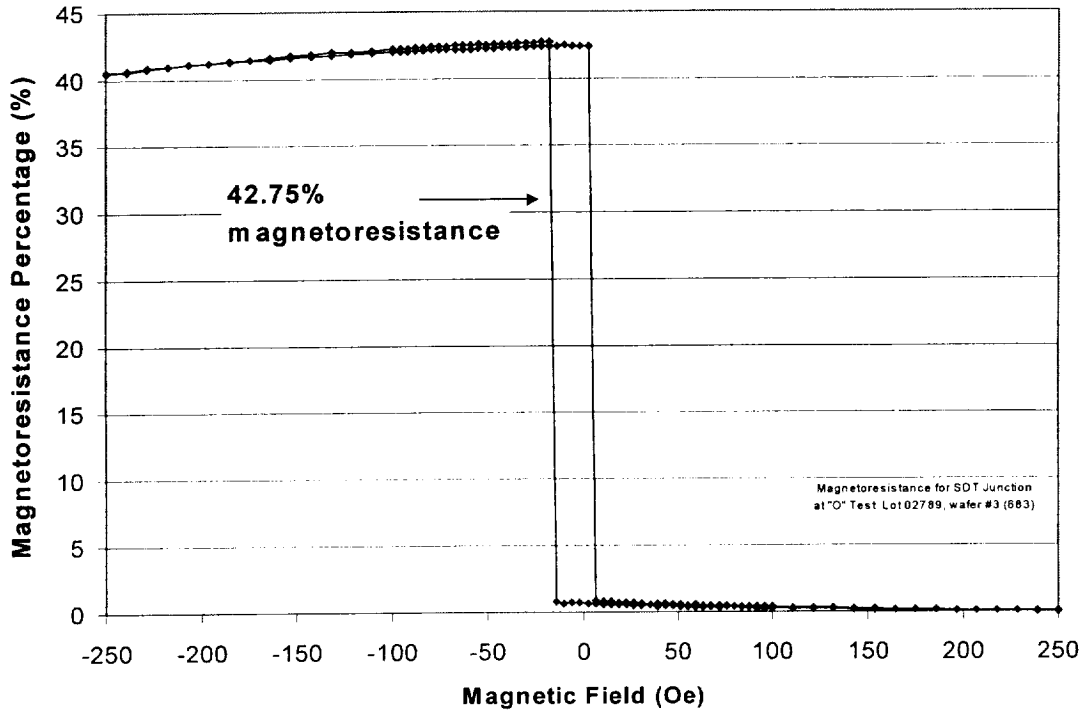

Figure 4.3. Unbiased SDT response. The change in resistance occurs when the magnetization of the free layer flips 180 degrees.

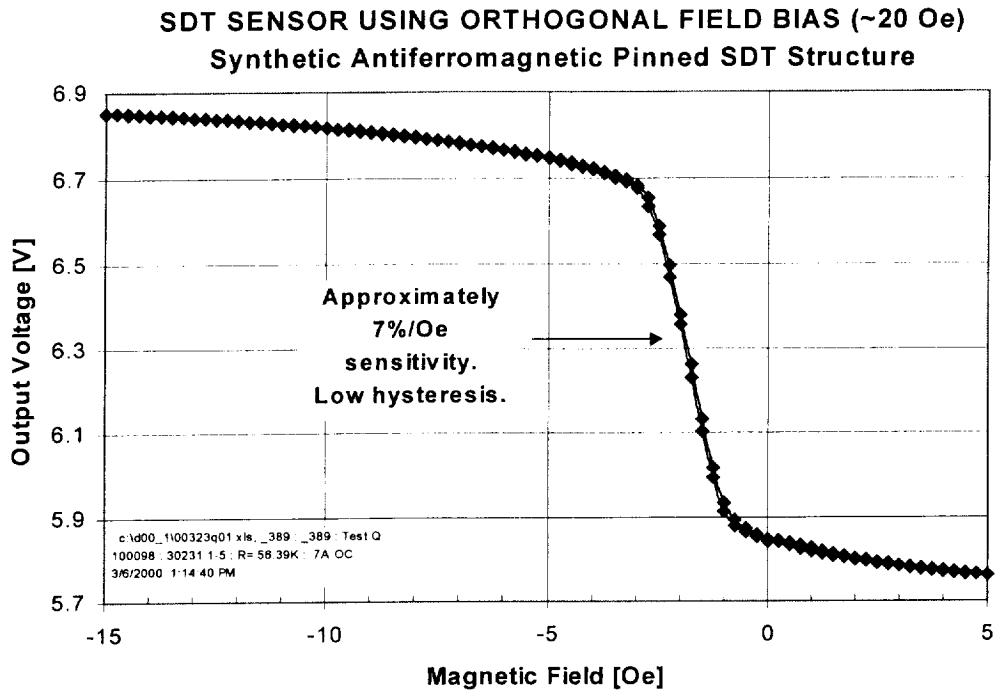

Figure 4.4. When the SDT device has a proper magnetic bias, the magnetization of the free layer rotates smoothly.

4.1.2.3. Flux concentrators These are usually 15 μm thick plated NiFe. Two flux concentrators on a sensor chip are arranged so that they are separated by a long narrow "gap". The sensitive axis of the sensor is parallel to the short dimension of the gap. Two opposite resistor legs (gap legs) are placed in the gap, while the other two are placed underneath the flux concentrators (shield legs). The field in the gap is "amplified" by the flux concentrators such that the gap field is [flux concentrator length] / [gap] x [external field]. The field under the flux concentrators reduced by a similar fraction. The net result is that the gap legs see a much greater field than the shield legs, and a net bridge offset is realized. The flux concentrators also have the effect of attenuating off-axis fields, so that the sensor becomes nearly a vector sensor (outputting the magnitude of the sense-axis field).

4.1.2.4. Sensor Output Once all of the pieces are together, the sensor output can be observed. Typical sensor output is shown in Figure 4.5.

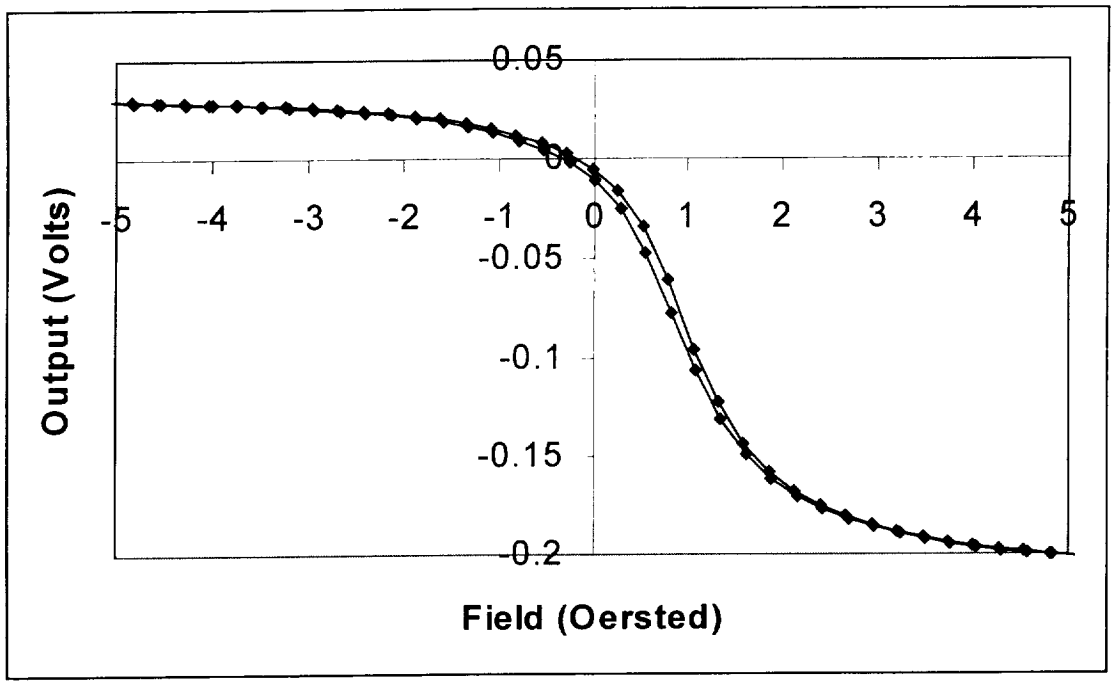

Figure 4.5. Actual SDT sensor output vs. magnetic field. This bridge is being supplied with 2 Volts, so the output range of 200 mV represents about 10% of the total supply voltage. The most sensitive part of the output is shifted about 1 Oe due to coupling between the pinned and free layers. The shift in voltage (vertical) is due to imperfectly matched SDT resistor legs.

4.2 Results

At the beginning of the project, there was no SDT magnetometer. Rather, there were SDT devices on wafers or in packages whose magnetoresistive properties could be measured. They were not yet put into functional resistance bridges with flux concentrators, biasing coils, and the like. Their performance as magnetometers, had the functional aspects been available would have been about 1 $\mu T/\sqrt{Hz}$ at 1 Hz (1000 $pT\sqrt{Hz}$). Electronics for magnetometers was simply some preamplifiers with no A to D converters, chopping, biasing, etc.

The incremental progress in SDT manufacture and performance are described in the Quarterly Progress Reports for this project. Top-level achievements during the course of this project include:

- Development and characterization of magnetometer electronics for 1 axis and 3 axis magnetometers with interface to a personal computer (Figure 4.6)
- Reduction of Resistance Area Product (RAP) of the SDT material
- Reduction of effective 1/f noise by several orders of magnitude
- Development of SDT sensor operating mode, including flux concentrators, magnetic field biasing, and bridge structures.
- Development of noise characterization capability
- Development of automated SDT sensor evaluation and test capability
- Investigation of voltage, current and field chopping techniques for reducing low frequency noise
- Full fabrication and testing of several thousand SDT sensors
- Temperature and radiation characterization

- Many peer reviewed publications (see Appendix A)

The SDT magnetometers developed during the course of this project have been shown to operate efficiently at temperatures as low as 4.2 K and withstand a total radiation dose of 1 MRad (SDT transducer only, not electronics). The best demonstrated effective noise floor is less than 300 pT/√Hz at 1 Hz, and less than 10 pT/√Hz above 1000 Hz.

SDT Performance Specifications (June, 2001)

Noise floor at 1 Hz	289 pT/√Hz	Best result
Noise floor (hi freq.)	7 pT/√Hz	Best result
Magnetoresistance	42.75%	Best result
Dynamic range	+/- 200 μT (2 Gauss)	Typical
Hysteresis	0.08 Oe on full sweep	Typical
Linearity	feedback required	
Bridge power	1 mW (10kΩ @ 2.5V)	Typical
Orthogonal Bias power	200 mW (500Ω @ 10V)	Typical
Die size	1775 μm X 2210 μm	
Package	SOIC-8 (5mm x 6mm)	
Cost	(low volume)	$6
Cost	(high volume)	$1
Reproducibility (June 2001)	over 10,000 made	not production qualified

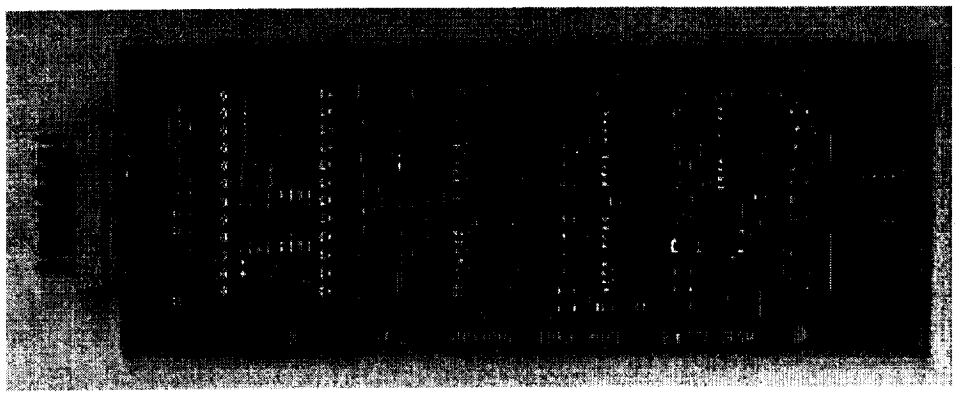

Figure 4.6 Packaged SDT magnetometer, approximately actual size. SDT sensor is small chip at right; other chips are support electronics.

4.2.1 Noise Floor

The progress over time of the SDT performance, and the best noise data are shown below.

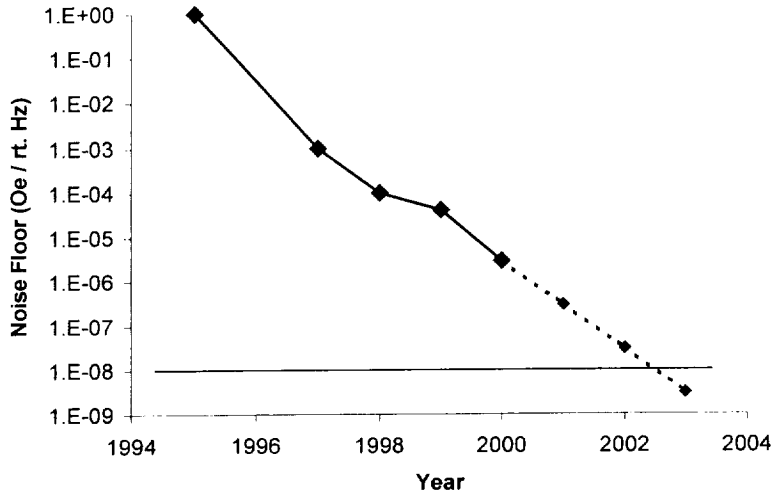

Figure 4.7. SDT transducer effective noise floor at 1 Hz vs. time. Improvement of about two orders of magnitude was achieved during the course of this project; the last batch of sensors produced for this project was in the year 2000 and had 1-Hz noise floors of ~$3x10^{-6}$ Oe/√Hz (0.3 nT/√Hz). Dotted line assumes an improvement of about 10x per year. The limit of this progress, while not known for sure, is likely to be ~10^{-8} Oe/√Hz (1 pT/√Hz; horizontal line).

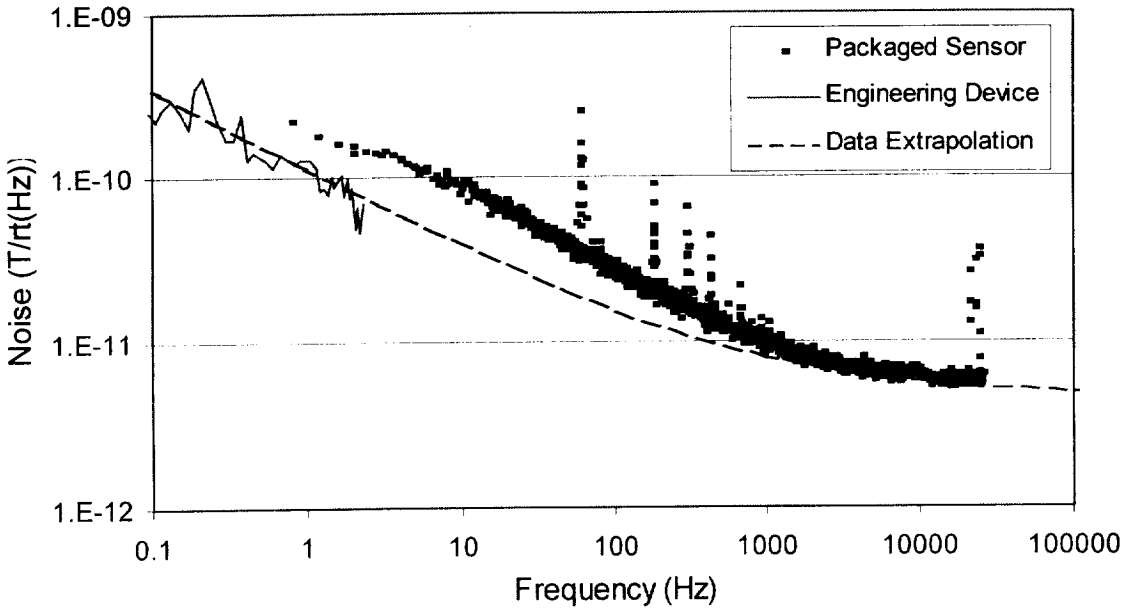

Figure 4.8. The best noise results from packaged parts and on-wafer parts. Note 1-Hz noise floor at ~0.1 nT√Hz and high-frequency noise floor of several pT/√Hz.

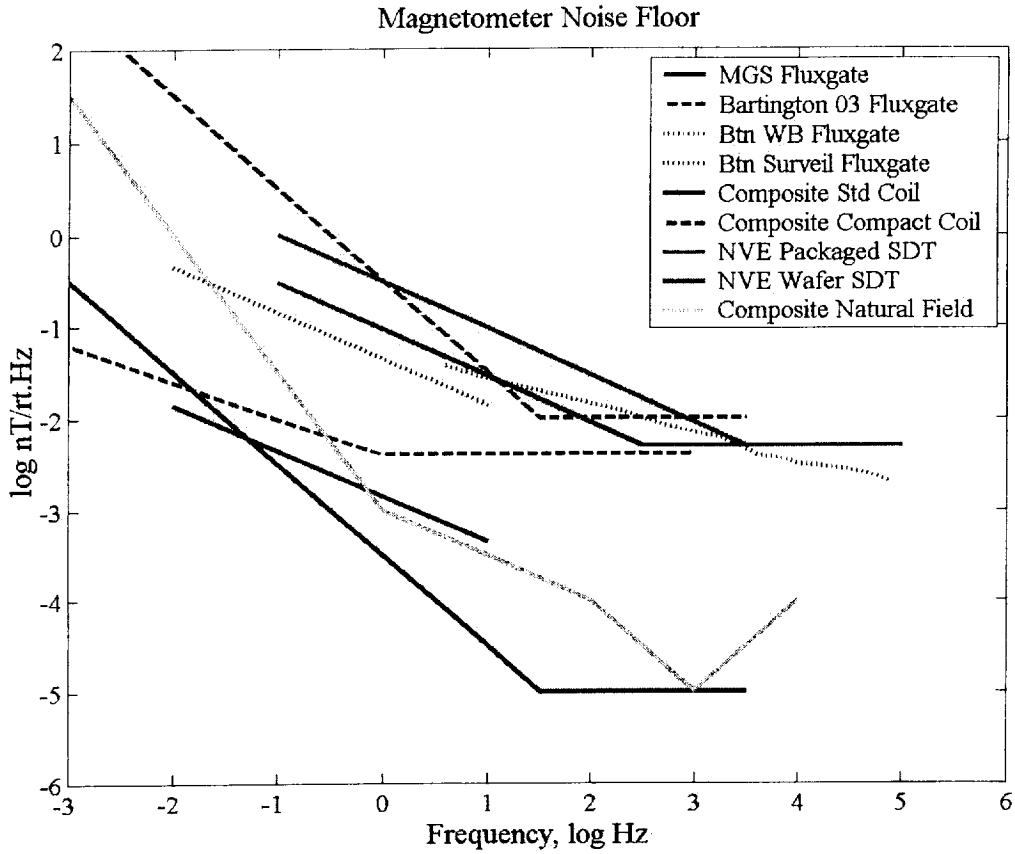

Figure 4.9. Comparison of noise floors of SDT sensors developed during the course of this project to other magnetometers. Above 1 Hz, SDTs perform comparably to a new generation of fluxgate magnetometers but SDTs are an order of magnitude smaller (10s vs 100s of grams). Below 1 Hz, fluxgate performance is still about two orders of magnitude better than SDTs.

4.2.2. Thermal

The goal of this portion of the study was to determine how well the SDT sensor functions over a broad temperature range from –70°C to +175°C. Two sensors were tested and both operated well over this temperature range with little qualitative change. The sensitivity of the two sensors changed by 15% and 25% over the temperature range measured and measurement of a known 0.5Oe field showed variations with temperature of 0.13Oe on one sensor and 0.27Oe on the other sensor. At 175°C, the sensors showed a reduction in the pinning strength of the IrMn layer, and a loss of pinning is expected to cause the sensor to fail at a temperature of approximately 225°C to 250°C. There was no indication that the sensor would fail to operate at low temperature.

To measure the sensor operation, two packaged SDT sensors were selected and a ThermoStream airflow system provided stable temperature control. With the device at a fixed temperature, an external field was ramped up and down between –7.5Oe to +7.5Oe. This field range was sufficient to fully saturate the soft magnetic layer of the sensor in each direction. Two sensors were selected to have a widely varying bridge resistance to identify possible differences in the temperature response. The sensors have resistances of 6.7kΩ and 137kΩ for devices identified

as SDT1 and SDT2, respectively. The difference in bridge resistance is primarily due to different numbers of junctions and junction sizes in the different sensor designs. Both sensors were made from the same wafer, so there should be little variation in junction material properties such as the resistance area product (RAP). The bridge was biased with a constant current of 1mA for SDT1 and 0.1mA for SDT2, which gives voltages of 6.7V and 13.7V respectively. In actual operation a constant voltage of approximately 10V is applied to the bridge. During the measurement, a 10V supply was connected to the orthogonal bias coil of the sensor as is typically done in operation of the sensor.

Changes with temperature were characterized first as the total voltage signal as a function of applied field, as the sensitivity near zero field (slope of voltage versus V/Oe field, or V/V/Oe), and as the drift for an applied 0.5 Oe field (a typical value for Earth's static field and a therefore worst case for time-variable fields). The last alone is displayed here. To estimate this drift, we picked out the sensor reading for an applied field of 0.5 Oe at different temperatures. The sensor voltage reading is calibrated to 0.5 Oe using the initial room temperature sensor voltage versus field slope and offset. Using this same calibration, the sensor field reading at 0.5Oe applied field is plotted for the different temperatures. To account for the sensor hysteresis, the field reading is always taken when the field is decreasing. Figure 4.10 shows the drift in field reading with temperature. This drift represents a worst-case situation for the sensor because at each temperature, the field is swept over a wide field range, forcing the soft magnetic layer to saturate in both the forward and reverse directions between each point plotted in Figure 4.10. Therefore, the data includes not only the drift, but also the reproducibility of the sensor after a field sweep. The two sensors show some deviation with temperature, though it is interesting to note that the dependence is in opposite directions. Sensor SDT 1 shows a lower field reading at low and high temperatures, while SDT2 shows a larger field reading at low and high temperatures. When there is no offset in the bridge, the temperature dependence of the four legs of the bridge are equivilent and the sensor shows no net change with temperature. However, any imbalance in the sensor will be exaggerated as the material resistance changes with temperature. The large negative field reading has nearly zero bridge offset signal, and only a minimal change with temperature, while the large positive field reading has a much larger bridge offset signal and changes substantially with temperature. Conversely, sensor SDT 2 (Fig. 5) has a larger signal at negative fields and is closer to 0 signal at large positive fields. Therefore, SDT 1 tends to become more negative at higher temperatures while SDT 2 tends to become more positive. This suggests that an ideal sensor that has zero bridge offset at zero field would show no drift in the zero-field reading as temperature is changed.

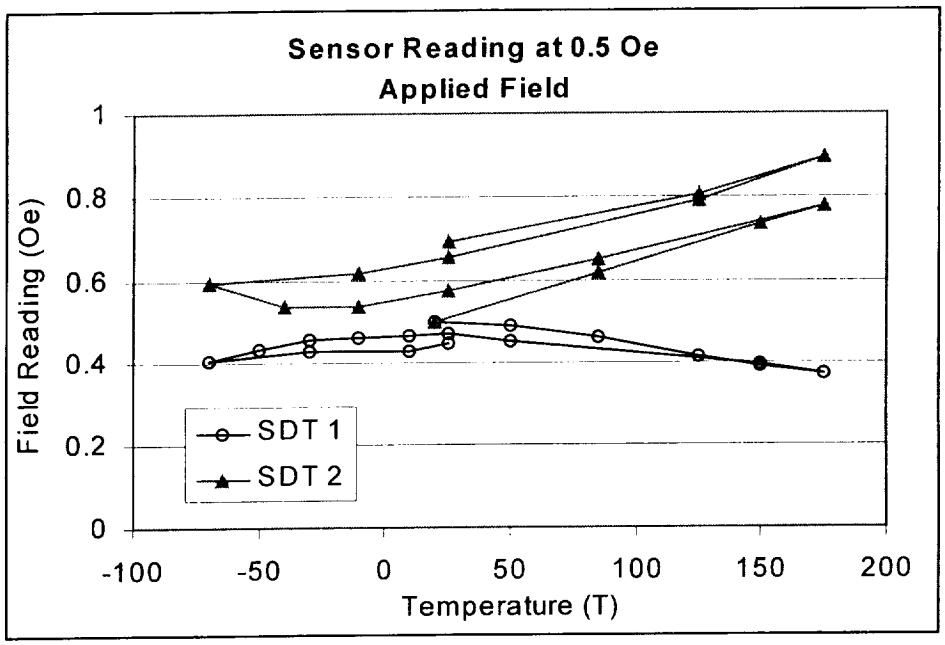

Figure 4.10. Measured signal versus temperature for an applied field of 0.5 Oe. The sensor is calibrated to read 0.5 Oe at 0.5 Oe applied field for the first room temperature sweep. Using the same calibration, the sensor reading at 0.5 Oe applied field is measured for subsequent sweeps at different temperatures.

Although the SDT sensor shows quite good response over the -70°C to +175°C temperature range tested, there are several ways that the performance might be improved. The primary limitation observed in operating at higher temperatures is the breakdown in the IrMn pinning strength. By selecting alternative pinning layers such as PtMn or NiMn, the pinning can be stable up to 350°C to 400°C. The sensor operation would then be limited by the thermal stability of the junction. Another possible problem in operating these sensors is slow degradation while operating at high temperatures. For these measurements, the sensor was only subjected to high temperature for approximately 5 minutes. We have not yet investigated the effects of long term exposure to high temperatures. In addition to the high temperature sensor failure, there is a 0.13Oe to 0.27Oe change in field readings over temperature due to changes in sensor sensitivity and changing voltage offsets. Most of the low temperature variation in sensitivity can be improved by using a constant current source for the orthogonal bias coil. The changes in zero-field offset voltage could be reduced by more accurately balancing the bridge to provide zero signal at zero field.

4.2.3 Radiation

The natural radiation environment in space is composed of trapped and solar protons, trapped electrons, and heavy ions from both galactic cosmic rays and solar events. These particles impart three types of failure mechanisms to typical electronics devices: (1) Total ionizing dose, which primarily affects oxides (2) Displacement damage, which is a degradation of the crystalline lattice structure (3) Single particle effects, including transients, upsets, latchup, and burnout. Cobalt60 testing is designed for addressing the total ionizing dose degradation of devices and essentially provides no information on any displacement damage effects since the displacement damage cross-section is many orders of magnitude less than the ionization cross-section. Proton testing of electronic parts provides both ionizing dose degradation as well as

displacement damage effects, so is a more effective, although typically more costly, testing technique. Proton testing provides the best simulation fidelity to the actual space environment. Although we can make broad generalizations about what types of devices are most affected by which degradation mechanism (minority carrier devices are more strongly affected by displacement damage, CMOS majority carrier devices are more sensitive to ionizing effects), we do not really know all the possible failure mechanisms any new technology device, especially sensitive sensors, might exhibit when irradiated. For this project, we were able to piggyback on another project and set up a limited number of exposures (0.5, 1, 2, 5 10, and 25 Krad) of SDTs to energetic protons.

Proton testing on the sensors at the Crocker Nuclear Laboratory at the University of California, Davis was planned during the 30-31 May time period as an add-on to another Ball experiment. At approximately 4:30 am on 31 May, about 8 hours into the radiation testing program, the cyclotron lost vacuum in the injector assembly while the primary experiment was taking place. The lost of vacuum was traced to a leak in a water cooling line inside a sizeable vacuum chamber. The estimated time to rebuild of the injector assembly was one week, so the testing was aborted. No additional proton testing could be scheduled within the scope of this project.

Cobalt exposure, in spite of its limited space-environment fidelity, was easier to arrange as a fallback. Five SDT sensors received a total of 1 MegaRad from a Co_{60} source. This total dose was achieved through repeated doses having sub-totals of 10k, 30k, 100k, 300k, and 1 Meg. Sensor performance was evaluated after each dose. No statistically meaningful change in sensor slope, offset, noise, or hysteresis was observed at any point. One of the 5 sensors had a small shift in total resistance, the cause of which is unknown.

4.3 Future Work

In our estimation, some work is required in three general areas: transducer performance, electronics "hardening", and temperature calibration.

Transducer performance improvements are required in noise and power. The noise is primarily caused by non-intrinsic 1/f noise, presumably due to non-ideal tunnel barrier properties. The power is mostly consumed by the 200 mW perpendicular biasing coil and not the <1 mW bridge.

Electronics hardening simply means that the present magnetometer electronics is not usable over the full space range of temperature and radiation. Consequently, a full system characterization is not possible. A space-worthy instrument would require an electronics redesign in order to address this issue. Though the cost of such a redesign would be relatively large, there is little technical risk, as such components exist.

To date, the temperature measurements have focused on demonstrating the feasibility of wide range operation. A space worthy instrument would have to go through a calibration of the full system (SDT transducer + electronics) to be of use.

4.4 References

[1] W. Thomson, "On the electro-dynamic qualities of metals; Effects of magnetization on the electric conductivity of nickel and iron," Proc. Roy. Soc., vol. 8, pp. 546-550, (1857).

[2] J. Smit, "Magnetoresistance of ferromagnetic metals and alloys at low temperatures," Physica 16, pp. 612-617, (1951).

[3] M.N. Baibich, J.M. Broto, A. Fert, F. Nguyen Van Dau, F. Petroff, P. Etienne, G. Creuzet, A. Freiderich, and J. Chazelax: Giant magnetoresistance of (001)Fe/(001)Cr magnetic superlattices, PRL 61 (1988), pp. 2472-2475.

[4] P. Grunberg, R. Schreiber, Y. Pang, M.B. Brodsky, and H. Sowers: Layered magnetic structures: Evidence for antiferromagnetic coupling of Fe layers across Cr interlayers, PRL 57 (1986), pp. 2442-2445.

[5] J.S. Moodera, L. R. Kinder, T.M. Wong, and R. Meservey, PRL 74, 16, p. 3273, (1995).

[6] T. Miyazaki and N. Tezuka, JMMM 139, L231 (1995).

[7] R.S. Beech, J. Anderson, J. Daughton, B.A. Everitt, and D. Wang, IEEE Trans. Magn. 32, p. 4713 (1996).

Publications

The following is a list of publications that were primarily or partially supported by this NASA project. In some cases, SDT devices that were fabricated under this NASA project were supplied to other groups for some kind of specialized characterization. In other cases, the SDT sensors were being developed for non-space applications.

"Interface Composition in magnetic tunnel junctions," R. Schad, K. Mayan, D. Allen, Jeff McCord, Dehua Yang, M. Tondra, and D. Wang, (INTERMAG 2001, in press, IEEE Trans. Magn.)

"Fabrication and properties of spin dependent tunneling junctions with CoFeHfO as Free layers," Dexin Wang, Zhenghong Qian, James Daughton, Cathy Nordman, Mark Tondra, Daniel Reed, and Dave Brownell, (INTERMAG 2001, in press, IEEE Trans. Magn.)

"Comparison of pinhole and defect density in Magnetic Tunnel Junctions," D. Allen, R. Schad, G. Zangari, I. Zana, M. Tondra, D. Wang, and D. Reed," (INTERMAG 2001, in press, IEEE Trans. Magn.)

"Micromagnetic Design of Spin-Dependent Tunnel Junctions for Optimized Sensor Performance," Mark Tondra, James M. Daughton, Catherine Nordman, Dexin Wang and John Taylor, J. Appl. Phys., Vol. 87, pp. 4679-4681, May, 2000.

"Pinhole Imaging in Magnetic Tunnel Junctions," R. Schad, D. Allen, G. Zangari, I. Zana, D. Yang, M. Tondra, and D. Wang, J. Appl. Phys., Vol. 87, pp. 5188-5190, May, 2000.

"High Temperature Pinning Properties of IrMn vs. FeMn in Spin Valves," Mark Tondra and Dexin Wang, JVST A, 17 (4), Jul/Aug, (1999), pp. 2220-2222.

5. HIGH-IMPEDANCE ELECRIC-FIELD SENSOR

This work described in this section was carried out by Geometrics, Inc., of San Jose, CA, by Dr. Jeff Johnston and Mr. Ken Smith under a subcontract to this grant.

The goal of obtaining a magnetotelluric (MT) sounding on Mars using natural field sources requires the measurement of the temporal variation of the electric and magnetic fields at its surface. If useful electric and magnetic field measurements can be acquired they will be converted into estimates of the surface impedance **Z** where in the most general form

$$E = Z \cdot H$$

Here, both E and H represent the complex electric and magnetic field vectors describing the horizontal field components in the frequency domain and $\boldsymbol{Z}$ is a complex tensor function of frequency. The components of $\boldsymbol{Z}$ are used to calculate an apparent resistivity as a function of frequency that is in turn used to calculate the variation of resistivity with increasing depth. If such an electrical resistivity profile can be obtained it should indicate the depth to a zone of partially melted permafrost if such a zone exists. It is expected that the temporal variations useful for study of this hydrologic regime will range from tens of kilohertz to less than 0.1 Hz.

The complex value E necessary for these calculations is defined relative to the instantaneous measured value E by

$$\mathcal{E} = \sqrt{2}\,\mathrm{Re}(Ee^{i\omega t})$$

Because a basic objective is the estimation of a transfer function, $\boldsymbol{Z}$, and not the estimation of power spectral densities, the impedance relationship does not depend on the statistics of the signals E and H: the response E is causally related to the input H. Never the less, accurate measurement of the E and H fields at the ground surface is still necessary for an accurate estimate of the surface impedance. This summary report describes design considerations, construction of a prototype antenna and amplifier, and performance tests of a circuit intended for accurate measurement of broadband electric fields on Mars.

5.1 Design Considerations

The ideal antenna for MT soundings on Mars would be lightweight and compact for efficient transport from Earth and permit mobility when deployed on Mars. Figure 5.1 shows the basic features of such an antenna. This antenna would be carried about by a small vehicle, receive various voltages signals on its elements, amplify them, and pass them along to a signal processor at its output. Electric field values would be calculated from these voltage measurements and used, along with local magnetic field measurements, to calculate the surface impedance beneath the antenna.

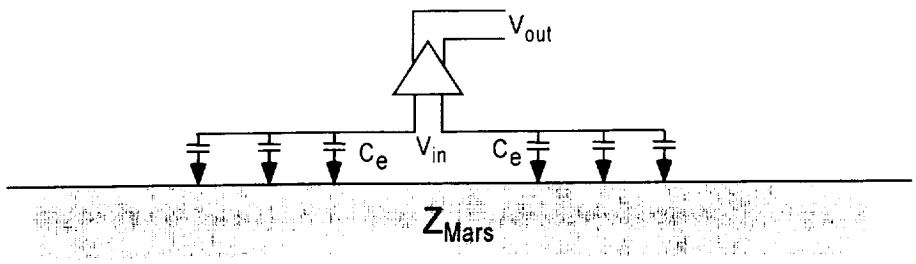

Figure 5.1

The measured voltage (and calculated electric field) will vary with frequency and will be dependent on the surface and subsurface resistivity structure, the geometry of the antenna and its position relative to both the vehicle and Mars. In the simple case where the antenna is parallel to the Martian surface, the surface resistivity is uniform, and the size of the vehicle is small compared to the antenna, the conversion of the measured antenna voltage to surface electric fields is straightforward. In this case, the voltage measurement is sensitive to differential charge accumulations on the ground surface. If the time variation of these charge distributions is due to magnetic induction, we can also expect that the calculated impedance is in fact a measurement of the surface impedance.

The useful portion of any electric field measurement is band limited. For the configuration shown in Figure 5.1, the limiting factors at low frequency are the perfection of the amplifier and C_e; capacitive coupling of the antenna with the surface. This low frequency cutoff (F) is given by:

$$F = 1/(2\pi R_{in} C_e)$$

where R_{in} is the input impedance of the amplifier. So, for this simple antenna-amplifier combination, the easiest way to lower the low frequency cutoff is by increasing C_e; the coupling of the antenna with the ground. If C_e were infinite we would have galvanic coupling and could make DC measurements. On the other hand, making the antenna smaller or elevating it above the planets' surface will reduce C_e and thereby reduce the low frequency signal contribution from the ground. Also, placing the antenna above the structure of the vehicle will effectively place another layer between this sensors and the ground. Unless the antenna is shaped like a long balance beam overhanging the vehicle, deployment above the vehicle produces an impedance measurement that now includes the vehicle. If the vehicle is more conductive than the ground, it will be the dominant electrical structure in the measurement.

Unfortunately, surface resistivity at the measurement site may not be uniform and this will lead to variations in the electrical current input along its length. It also may be difficult to lay even a flexible antenna parallel to the ground surface so that capacitive coupling is uniformly distributed. These circumstances make it impossible to calculate the voltage gradient. One way to mitigate these circumstances is to increase the separation between the antenna cable and the ground. An increased separation will, however, reduce C_e and thereby increase the cutoff frequency. This means that the signal is high-pass filtered and so the net result of elevating the cable is to reduce the depth of exploration. These practical concerns argue against the use of capacitive-coupled cable antennas in electromagnetic sounding and lead to considering a configuration less ideal than depicted in Figure 5.1.

Conventional earth-bound MT systems measure electric fields by making electrical contact with the ground through non-polarizing chemical electrodes or simple metal stakes. Figure 5.2 depicts the electric field measurement scheme of such a system. Here, low frequency measurement with a low resistance contact (r) permits a conventional galvanic MT system to measure the electric field with negligible signal contribution due to capacitive coupling (c) between the cable and the ground. This is because the impedance of the capacitive term ($1/\omega c$) is much greater than that of resistive element (r) for small ω. With voltage input only at the electrodes, the calculation of the voltage gradient can be made with confidence.

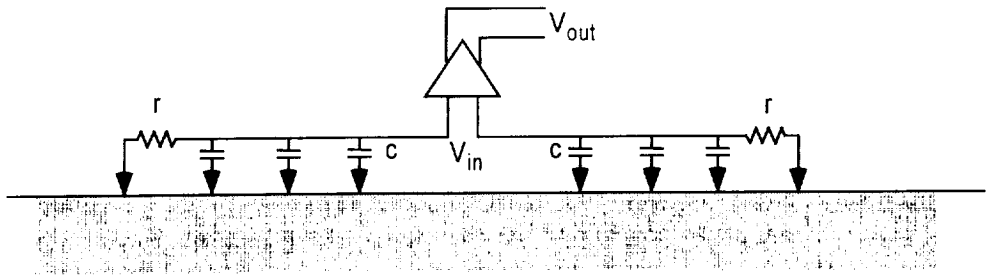

Figure 5.2

A different situation is shown in figure 3 where, either because of high contact resistance (**R**) or an attempt to make high frequency measurements, capacitive coupling between the cable and the ground becomes important. This situation degrades the electric field measurement for a conventional galvanic MT system because there is a significant but unknown signal contribution due to capacitive coupling (c) between the cable and the ground. In this case, the capacitive impedance ($1/\omega c$) becomes small enough relative to **R**, that a significant of portion of V_{in} is due to capacitive coupling with the earth. This means that the calculation of the voltage gradient is uncertain due to uncertainty in the effective dipole length. The net result is distortion of the measured electrical spectrum because of the frequency dependence of the capacitive coupling term.

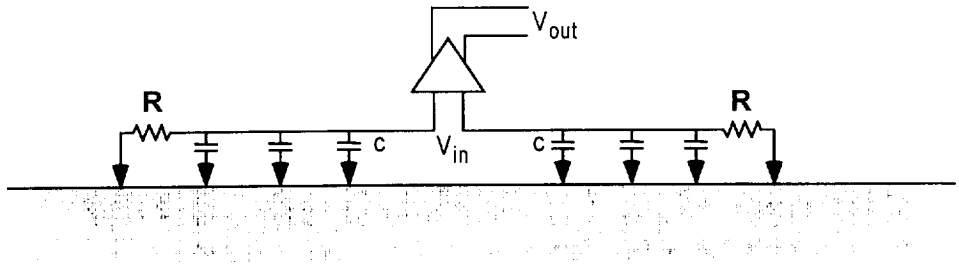

Figure 5.3

Including 'buffered' electrodes in the dipole circuit as shown in Figure 5.4 can reduce the signal contribution due to capacitive coupling thought the antenna cable (c). This buffering circuit is know as a 'voltage follower' and consists of a unity gain amplifier at the electrode that has very high input impedance and low output impedance compared to the capacitive contact the dipole makes with the earth. This allows signal currents arising from capacitive input along the cable to flow to the buffer amplifier's output instead of to the differential amplifier's input. Buffered

electrodes are used on at least two existing MT systems: they are used as the high frequency electric field sensors on Geometrics' EH4 CSAMT system and also on the University of Utah's EGI MT system. Buffered electrodes are necessary in the EH4 system for signals above about 1 kHz and are used with the EGI system when it is deployed on glacial ice.

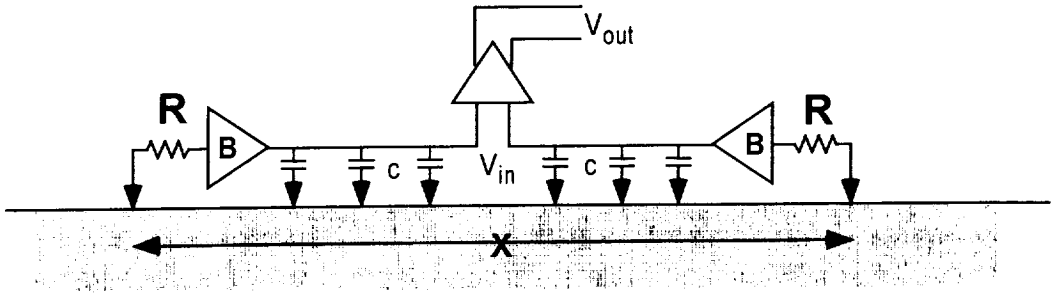

Figure 5.4

If galvanic contact with conductive ground is extremely poor or logistically impossible, local capacitive coupling to the ground is an alternative that may provide low distortion electrical contact as shown in Figure 5.5. The inclusion of a capacitive electrode in combination with the finite input resistance of the buffer circuit again creates a high-pass filter Here, signal distortion will be low (less than 0.5%) only if the input impedance of the buffer circuit is at least 10 times greater than the impedance of the capacitive contact C_e. This leads to trade offs between the size of the electrode, the performance of the buffer amplifier, and the lower cutoff frequency of the system. If, for example, a capacitive contact comprised of a 10 cm diameter disk was positioned 1cm from the ground surface, the contact impedance (Z_{Ce}) would be 22.9 G-ohm at 1 hertz. This requires that an effective buffer input impedance of about 230 G-ohm is needed if the system is to achieve low distortion electrical contact for a 1 hertz signal through this small plate lying near the ground.

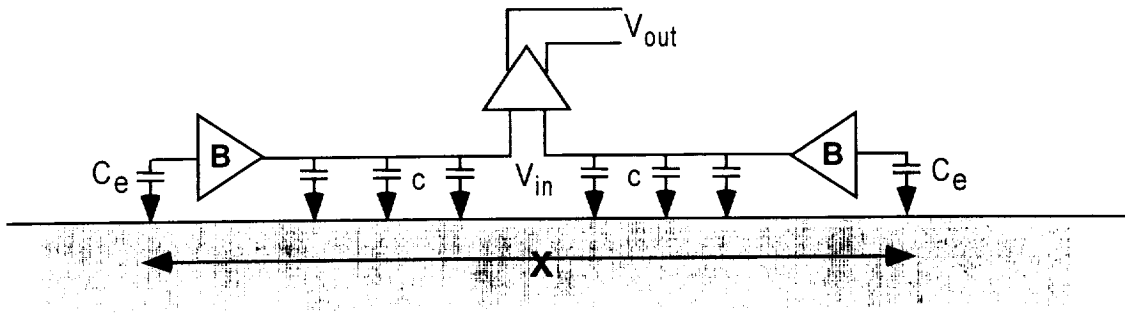

Figure 5.5

Experiences with the EGI MT system in Antarctica have shown that electric field measurement at low frequency in a dry environment is difficult when contact resistance is high. The difficulty arises from the noise effects caused by the discharge of wind-generated static electricity near the electrodes. If signal strength is low, or weather conditions are poor it will be difficult to obtain useful signal without reducing this stray voltage. As shown in Figure 5.6, this can be done by surrounding the electrode with a conductive shield connected to the low impedance output of the buffer amplifier via a small resistance; small relative to the output impedance of the buffer

amplifier. There are two problems caused by the inclusion of this shield however: 1) the small output impedance of the buffer amplifier is in series with the shields' capacitance to ground and this will attenuate higher frequency signals; and 2) the capacitance from shield to amplifier input is a feedback path around the buffer amplifier which changes the effective impedance of the amplifier and may lead to instability of its output. The later of these two problems is the most nettlesome because amplifier instability defeats the low frequency enhancement that is the intended purpose of the static shield. Stability problems are increased by the need to power the buffer amplifier through the sensor cable: stray voltage on the shield is capacitively coupled onto the power supply and, because it is not completely removed, will reappear to some extent on the amplifiers' output.

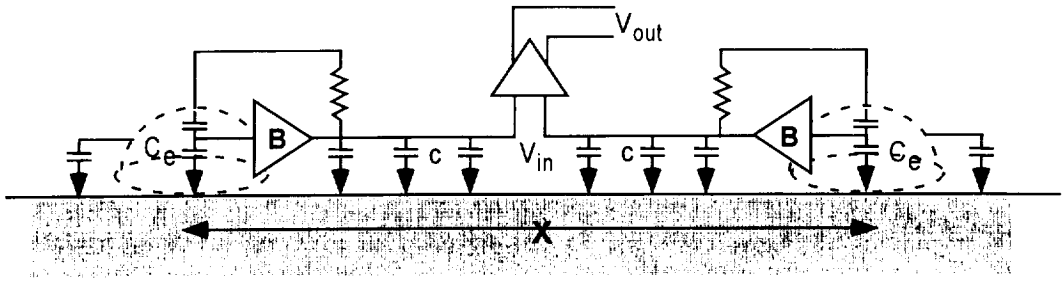

Figure 5.6

A solution to the stability problem is do drive the shield through a 'better' resistor which takes the form of another amplifier. This amplifier is shown in Figure 5.7 as S1. It is also shown providing power to the buffer amplifier and in so doing its output is driving all the capacitance connected to the buffer amplifier except the input C_e. If S1 has a gain of 0.99, all of the capacitance connected to the buffer amplifier except C_e will appear to be 100 times smaller than they are because the potential across them is reduced by a factor of 100. In addition, because the buffer amplifier has the same signal on its power supply as is on its output and on a portion of its input, the common mode rejection ration of the buffer amplifier will also be improved by a factor of 100. The ultimate benefit of this feedback scheme is the effective increase in the input impedance of the system. Because of the internal linkage between the power supply of an amplifier and its input impedance, the power supply feedback shown here will increase system input impedance by a factor of 100.

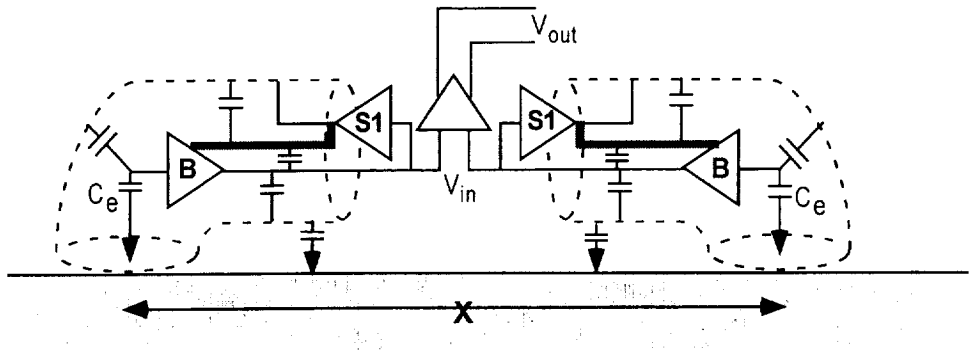

Figure 5.7

Driving the sizeable capacitance created by a length of sensor cable may degrade the performance the S1 amplifier To avoid degraded performance, the shielding circuit is reconfigured so that three separate amplifiers are used to drive two shields as shown in Figure 8. The circuit shown in Figure 5.8 is just one side of the device that feeds the differential amplifier. This scheme requires that any given amplifier section only needs a gain of about 0.9 under load to provide an overall gain performance of 0.99.

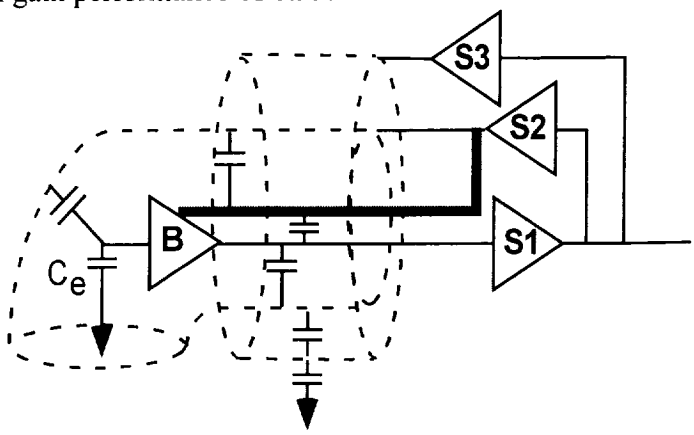

Figure 5.8

5.2 Prototype

The circuit shown in Figure 5.8 was constructed as a field prototype. This field prototype has been debugged and performance tested in a laboratory environment. It consists of a buffer circuit, an interconnect cable, and the shield driver/power supply circuit. These components are shown in sequence from left to right in photo 1. When assembled with the short lab cable, the device is about 1.5 m long. The shield driver circuit should accommodate an interconnect cable length about 10 m long. A cross section of this cable is shown in Figure 5.9. The two coaxial shields in the cable correspond to the nested shields (dashed) shown in Figure 5.8 and the various core conductors carry the power to and signal from the buffer circuit.

Figure 5.9.

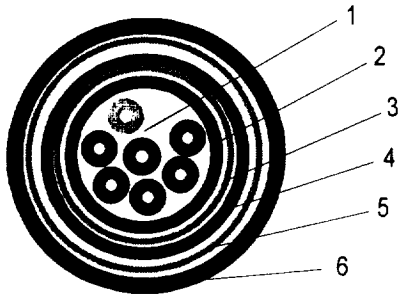

1) 8 #26 AWG multi-strand tinned copper with cross linked polyethylene insulation; color coded black, brown, red, orange, yellow, green, blue, and violet.
2) 1/16" thick polyurethane jacket.
3) Foil shield to provide 100% coverage incorporating a bare #22 multi-strand tinned copper leader.
4) 1/16" thick polyurethane jacket.
5) Foil shield to provide 100% coverage incorporating a bare #22 multi-strand tinned copper leader.
6) 1/16" thick polyurethane jacket.

Figure 5.10

Laboratory tests of the prototype device consist of placing the assembly in a Faraday cage so that the buffer amplifier is in the center of the cage. The cage provides a relatively quiet, static free environment. This is a favorable environment for making fine adjustment to certain component values in order to improve stability and performance. The cage can also be driven with a signal generator while the buffer's output is measured and this result will provide the frequency response of the device. As shown in the functional diagram in Figure 5.11, this was done by connecting a function generator between the amplifier ground and the Faraday cage. Here, the capacitor C_e is a capacitor comprised of the electrode, a 10cm long wire protruding from the buffer amplifier enclosure and the Faraday cage. The dashed circle in figure 10 surrounds the entire device represented as a perfect unity gain amplifier in parallel with some effective input impedance Z_{in}.

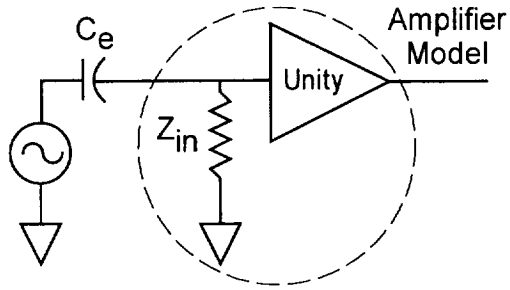

Figure 5.11

Figure 5.12 shows the measured frequency response of the device. Examination of the upper plot in this figure reveals that the pass band of the device extends from approximately 0.6 Hz to 20 kHz. If the values of C_e and Z_{in} were both known independently, the low frequency limit

could be calculated using the formula for the half power point of an RC filter: $F = 1/(2\pi R_{in}C_e)$. The pass bands' upper limit is controlled by the small output impedance of the buffer amplifier that is in series with the shields' capacitance to ground.

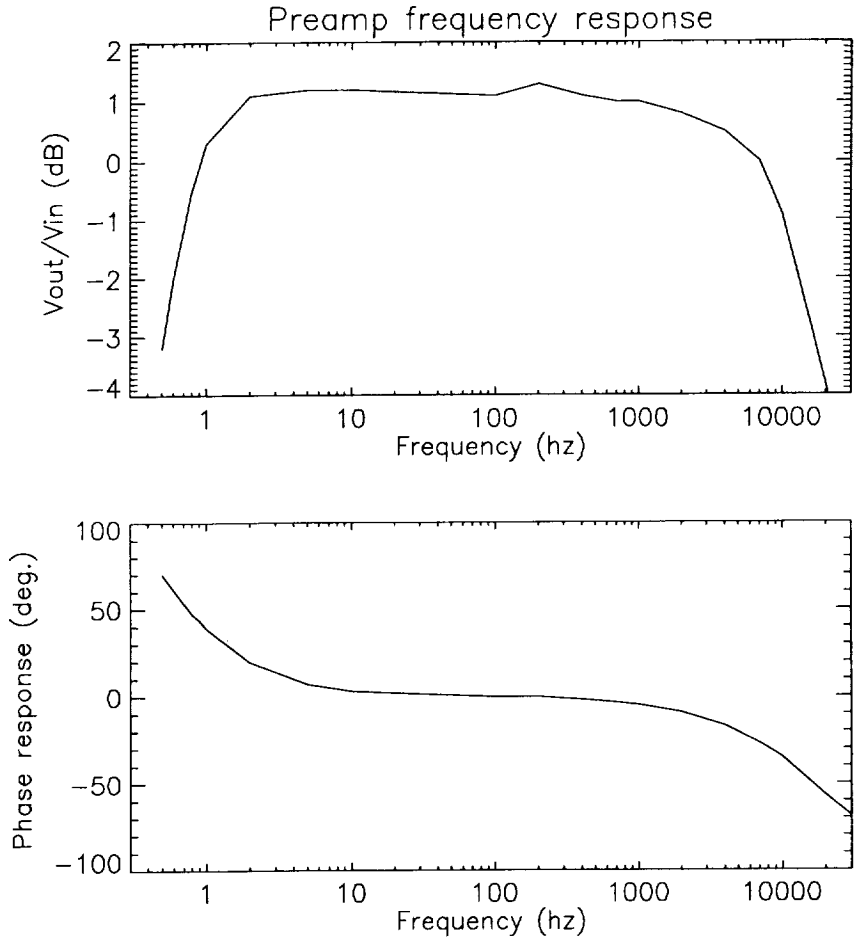

Figure 5.12

These measurements of the amplifier's frequency response allow us to calculate the effective input impedance of the amplifier. The value of C_e is conservatively calculated to be 1.0061e-12 farad based on a surface area for the equivalent spherical diameter of the 10cm electrode (7mm diameter) inside a 2.6m diameter spherical cage. The half-power point of the amplifier at approximately 0.6 hz, and this yields a calculated value of 265G ohms for the minimum input impedance Z_{in}. Because the nominal input impedance of the buffer section is 1.5G ohm this means that the feedback in the prototype circuit has a gain performance of 0.995 +/- .001.

Measurements of the environmental signal strength plus preamplifier are shown in Figure 5.13 as preamplifier output amplitude versus frequency. These measurements were made with the buffer portion of the circuit located in the center of the Faraday cage. The spectra were calculated from the average of 5records each containing 2500 samples and were smoothed via convolution with a 5 point Hanning window. Both the first and third power-line harmonics are clearly visible and stand about 40 dB above the 100-microvolt background. This background signal is a

combination of circuit noise and environmental signals that penetrate the cage. The increase in signal level with period is most likely due to insufficient antialiasing of the preamplifier output. relative to our lab's noise environment. Considering the cultural noise signal strength in the lab and the high input impedance of the preamplifier, the 70 - 80 micro-volt/m background value is for electric field strength is considered reasonable. These values are about 500 to 1000 times higher than typical natural fields that would be measured through galvanic contact on 10 ohm-m ground.

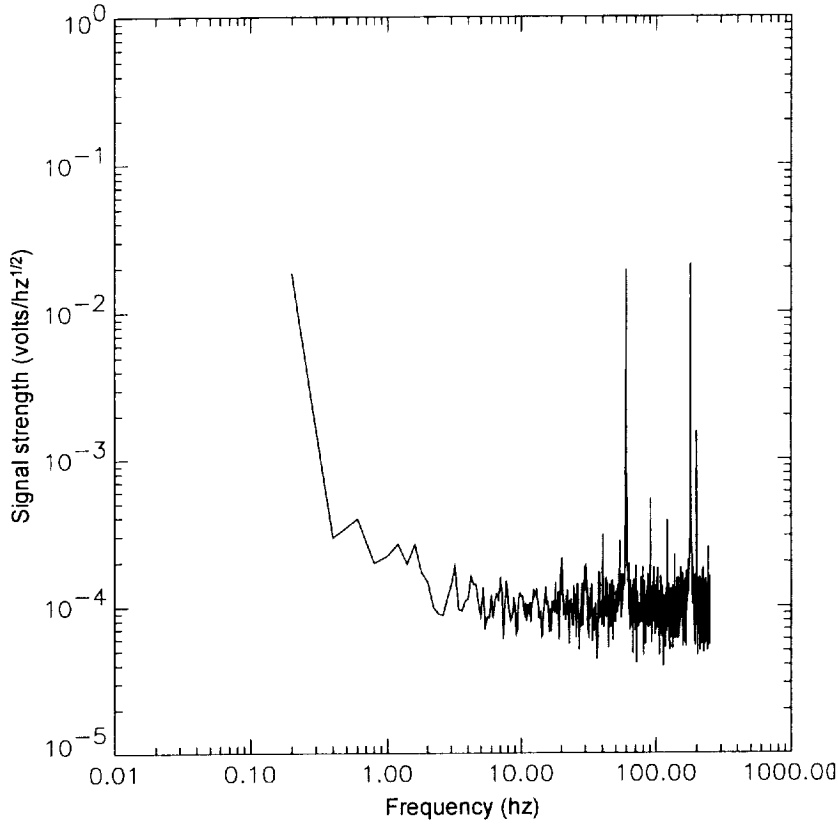

Figure 5.13

6. Low-Frequency Electromagnetic Sounding for Groundwater on Mars

This section describes the predicted responses of groundwater on Mars to EM induction, the likelihood of various natural EM sources, the resources (size, mass, power) required for natural- and artificial-source soundings, the applicability of different sensors, and several mission scenarios for ground and airborne platforms. For compactness, this section is appended in the form of the galley proofs for the in-press article in *Journal of Geophysical Research, Planets.*

Low-frequency electromagnetic exploration for groundwater on Mars

Robert E. Grimm

Blackhawk Geoservices, Inc., Golden, Colorado, USA

Laboratory for Atmospheric and Space Physics, University of Colorado, Boulder, Colorado, USA

Received 11 April 2001; revised 17 September 2001; accepted 21 September 2001; published XX Month 2002.

[1] Water with even a small amount of dissolved solids has an electrical conductivity orders of magnitude higher than dry rock and is therefore a near-ideal exploration target on Mars for low-frequency, diffusive electromagnetic methods. Models of the temperature- and frequency-dependent electrical properties of rock-ice-water mixtures are used to predict the electromagnetic response of the Martian subsurface. Detection of ice is difficult unless it is massively segregated. In contrast, liquid water profoundly affects soundings, and even a small amount of adsorbed water in the cryosphere can be detected. Subcryospheric water is readily distinguishable at frequencies as low as 100 Hz for fresh water to 10 mHz for brines. These responses can be measured using either natural or artificial sources. ULF signals from solar wind and diurnal-heating perturbations of the ionosphere are likely, and disturbances of regional crustal magnetic fields may also be observable. Spherics, or ELF-VLF signals from lightning discharge, would provide optimal soundings; however, lightning may be the least likely of the possible natural sources. Among the active techniques, only the time-domain electromagnetic (TDEM) method can accommodate a closely spaced transmitter and receiver and sound to depths of hundreds of meters or more. A ground- or aircraft-based TDEM system of several kilograms can detect water to a depth of several hundred meters, and a system of tens of kilograms featuring a large, fixed, rover- or ballistically deployed loop can detect water to several kilometers depth. *INDEX TERMS:* 0694 Electromagnetics: Instrumentation and techniques, 0925 Exploration Geophysics: Magnetic and electrical methods, 6225 Planetology: Solar System Objects: Mars, 5494 Planetology: Solid Surface Planets: Instruments and techniques; *KEYWORDS:* Mars, water, electromagnetic, magnetotelluric, TDEM

1. Introduction

[2] Detection of subsurface, liquid water on Mars is a key exploration goal, crosscutting themes for geology, climate, life, and resources [*Mars Exploration Program/Payload Analysis Group (MEPAG)*, 2001]. Signs of relatively shallow subsurface water (at depths of perhaps a few hundred meters) in recent geological history [*Malin and Edgett*, 2000] potentially put that water within the range of robotic drilling [*Blacic et al.*, 2000]. Geophysical exploration for groundwater is well established on Earth, and this legacy can be applied to Mars. The most widely regarded methods are seismic and electromagnetic (EM). Seismology is the single most successful geophysical method in history because of its strengths in imaging and in resolving deep earth structure. While it is possible to distinguish water-saturated rock from dry rock (a fundamental task of seismic exploration for natural gas [e.g., *Grimm et al.*, 1999]), large resources usually must be mobilized to achieve these results, and the changes in material properties can be subtle. In contrast, the difference in electrical conductivity between wet and dry rock can span orders of magnitude, and soundings can be made from a single station.

[3] A fundamental division in EM behavior is between high- and low-frequency methods. The mathematical distinction between these end-members is outlined in more detail below, but essentially, high frequencies are propagative or wave-like, whereas low frequencies are inductive or diffusive. Ground-penetrating radar is the most familiar example of the former and is the most commonly considered approach to planetary subsurface EM exploration. The Apollo 17 Lunar Sounder Experiment (ALSE) [*Phillips et al.*, 1974] pioneered orbital subsurface exploration, and orbital radars are planned for Mars and Europa. Advantages of radar include signal controllability and high resolution. Disadvantages include potential strong losses due to absorption, scattering, and multiple reflections, contrasts in permittivity that are still small compared to those in conductivity, and sidelobe ambiguities for shallow reflections.

[4] On Earth, low-frequency EM methods have dominated exploration for groundwater at depths of hundreds of meters (see *McNeill* [1990] for a review). Both active (using a transmitter) and passive (using natural sources) have seen wide application. Advantages of low-frequency methods compared to radar include greater sensitivity to the geoelectric section and simpler operation and interpretation. Disadvantages include greater mass and power for the active methods and poorer resolution overall.

[5] This paper takes a broad approach to the detection of groundwater on Mars using low-frequency EM methods. It is lengthy for two reasons. First, essentially the entire field of inductive EM on Mars requires reconnaissance, including the predicted response of the planet, the applicability of different sensors, the likelihood of natural sources, and the resources (size, mass, power) required for natural- versus artificial-source soundings. Second, these methods are relatively new to solid earth planetary science, particularly as surface or airborne measurements: to date, low-frequency EM has been used only for global sounding in conjunction with an external magnetic field, for the Moon [e.g., *Schubert and Schwartz*, 1969] and the satellites of Jupiter [*Khurana et al.*, 1998]. Therefore this paper also has some tutorial review, with specific application to Mars.

0148-0227/02/2001JE001504$09.00

[6] The first goal is to determine the key frequency ranges for detecting subsurface water on Mars as functions of depth, thickness, and salinity. The core calculations toward this end (the response of a layered medium to vertical plane waves) are the same kind as those that preceded ALSE [*Ward et al.*, 1968], except here the emphasis is on the low frequencies and both the constitutive relations and variety of layered models are developed in greater detail. Both natural- and artificial-source methods are considered. Natural-source measurements are preferred when mass, size, and power strongly constrain the instrument. Deep targets, in particular, may also require excessive power at long wavelengths such that only natural-source methods could succeed. As these techniques rely totally on the presence of natural EM energy, constraints on such sources are discussed. Artificial-source methods are preferred for shallow targets owing to controllability of the signal and consequent higher signal-to-noise ratio. The depth of detection of groundwater under the preferred artificial-source method is developed in some detail because of the strong resource trade-offs. Both measurement techniques and some advances in sensor technology are reviewed, with recommendations on optimum methods, sensors, and platforms.

[7] In this paper the term "water" is used to denote all forms of H_2O, and "groundwater" and "subsurface water" are used specifically to distinguish liquid. In addition, both electrical conductivity and resistivity are used; these quantities are of course reciprocal.

2. Distribution of Water

[8] Abundant geological evidence, including the outflow channels, valley networks, and features indicative of ground ice, points to significant quantities of water on Mars in the past (see *Carr* [1996] for a review). Estimates of the global inventory of water span several orders of magnitude, with the geology-based figures mostly in the range 100–1000 m column-equivalent [*Carr*, 1996]. At a porosity of 10%, water would then fill the upper crust to a depth of 1–10 km.

[9] Water that has at some time been part of a hydrologic cycle on Mars (even if only a single or partial cycle) is likely held principally as ice in the cryosphere, the effectively permanently frozen portion of the upper crust. If the water inventory does not exceed the storage capacity of the cryosphere, then the cryosphere will be incompletely saturated. Liquid water may exist owing to heterogeneity in thermal properties within the cryosphere (thus locally obviating its definition) and also as adsorbed, unfrozen water. The latter is generally restricted in terrestrial permafrosts to a few percent by volume within 10–20 K of the melting point, but these values are unknown for Mars. Groundwater will exist below the cryosphere if the global inventory of water exceeds the storage capacity of the cryosphere.

[10] *Clifford* [1993] developed detailed models of the distribution of water and ice in the upper crust. He determined the depth to the base of the cryosphere by considering the mean temperature at different latitudes and likely ranges for the heat flux, thermal conductivity, and influence of salts on melting-point temperature. Using a contemporary heat flux of 30 mW/m^2 [*Schubert et al.*, 1992] and a thermal conductivity of 2.0 W/(m K), appropriated to ice-cemented rock or soil, Clifford determined that the depth to the base of the cryosphere varies from 2.3 to 6.5 km as a function of latitude.

[11] The discovery of "gullies" [*Malin and Edgett*, 2000] poses strong challenges to the notion that the cryosphere is everywhere kilometers thick. These features, whose individual morphologies indicate both erosion and deposition under the action of surface water, appear to discharge on steep slopes at depths of a few hundred meters below overlying plateaus. They are almost entirely crater-free and therefore relatively recent. It is unlikely that transient aquifers can appear at such depths solely owing to melting of ice under climatic variations [*Mellon and Phillips*, 2001]. However, higher geothermal gradients could restrict the cryosphere to just a few hundred meters instead of kilometers [*Mellon and Phillips*, 2001]. In the absence of local hydrothermal convection, this hypothesis relies critically on the presence of an extremely low thermal conductivity regolith (0.045 W/(m K)): while this extrapolation from surficial thermal-inertia measurements is not unreasonable, there are no independent geological indicators of such a thick, low-density blanket.

[12] A key implication of this hypothesis is that shallow groundwater can be geologically long-lived. *Mellon and Phillips* [2001] speculate that water is released episodically on high slopes owing to the failure of bounding ice dams under climatic freeze-thaw variations. In contrast, other competing hypotheses, such as pumping due to secular growth of the cryosphere or contraction of the lithosphere, imply that shallow groundwater is transient. The discrete points of outflow of the gullies suggest individual aquifers, but the subcryosphere could alternatively be more or less completely saturated, even as both aquifers and aquitards are on Earth. In both cases it is unknown whether the processes that lead to shallow aquifers are widespread and discharge is expressed only in a few regions or whether the cryosphere is thin only locally and, say, *Clifford*'s [1993] model holds globally. A geophysical search for subsurface water at depths up to several hundred meters would provide critical tests of these hypotheses. The gullies are also profoundly significant in that they may point to water that may lie within the depth of first- or second-generation drilling demonstrations on Mars [*Blacic et al.*, 2000], not in the second or third as previously thought for a thick cryosphere.

[13] The distribution of groundwater below the cryosphere is unknown. *Clifford* [1993] assumed that all such water would drain downward and computed water-table depths by further assuming that the upper crust of Mars has a megaregolith structure whose properties can be approximated by scaling from the Moon. In Clifford's model the surface porosity is taken to be 20 or 50% and decreases exponentially with a scale height of 2.82 km. Porosities below 10-km depth (computed to be <0.6–1.4%) are neglected, as it is assumed that the megaregolith closes all porosity owing to self-compaction at 1 kbar. Depending on the global water inventory, the thickness of the cryosphere, and the elevation, subcryospheric groundwater could be in contact with the cryosphere or lie at a depth of up to several kilometers deeper. Although both the self-compaction and exponential-porosity criteria can be called into question, changes in either are not likely to change the subcryospheric storage capacity by more than a factor of 2 or 3. Related to questions of groundwater movement is the assumption that water will drain downward and form a subcryospheric water table. This is clearly an extreme case, as capillary and hygroscopic forces limit the amount of water that can drain: the specific retention of terrestrial unconsolidated sediments is 5–50% [e.g., *Davis and DeWeist*, 1966] and could be larger under the lower gravity of Mars. There is no reason to expect subcryospheric water to drain downward, particularly if the base of the cryosphere is deep as in Clifford's model and therefore the rock porosity is small. A more likely alternative, then, is that the subcryosphere should be considered analogous to a partially saturated vadose zone.

[14] In reality, the distribution of ground ice and water is of course likely to be both vertically and horizontally heterogeneous. Some more detailed comments are made below on resolution, but in general, horizontal changes will be easier to map than complex vertical stratigraphy. The models presented in this paper are therefore idealized but nonetheless are intended to capture the fundamental trends that would be observed in practice.

3. Apparent Resistivity of a Layered Half-Space

3.1. Diffusion Versus Propagation

[15] Electromagnetic fields and waves are described by Maxwell's equations and the constitutive relations involving electrical

conductivity σ, magnetic permeability μ, and electrical permittivity ε (for numerical convenience, the permittivity can be expressed as the product of the relative dielectric constant ε_r and the permittivity of free space ε_0: $\varepsilon = \varepsilon_r \varepsilon_0$). These relations can be combined as functions of frequency f to form the Helmholtz equations [e.g., *Ward and Hohmann*, 1988]

$$\nabla^2 \begin{pmatrix} E \\ H \end{pmatrix} = i\omega\mu(\sigma + i\omega\varepsilon) \begin{pmatrix} E \\ H \end{pmatrix} = -k^2 \begin{pmatrix} E \\ H \end{pmatrix}, \quad (1)$$

where E and H are the electric and magnetic field strengths, respectively, $\omega = 2\pi f$ is the angular frequency, $k = \sqrt{\omega^2\mu\varepsilon - i\omega\mu\sigma}$ is the wave number, and $i = \sqrt{-1}$. Two end-member behaviors are evident. At high frequency, $k^2 \approx \omega^2\mu\varepsilon$, and the Helmholtz equation reduces to the wave equation: energy transport is by propagation of the electromagnetic field and is dominated by the permittivity and permeability. Attenuation per wavelength is small. At low frequency, $k^2 \approx -i\omega\mu\sigma$; the Helmholtz equation reduces to the diffusion equation and is controlled by the conductivity and permeability. Attenuation is strong, with the field strength decreasing by $\exp(2\pi) \approx 500$ in one wavelength. The attenuation can also be expressed as a skin depth $\delta = \sqrt{2/\sigma\mu\omega} \approx 500/\sqrt{\sigma f}$ in MKS units. The importance of diffusion relative to propagation, or loss to storage, is quantified by the loss tangent $\sigma/\omega\varepsilon$. The complementary cotangent measures the phase angle between the electric field and the flux direction. The diffusive regime is also called "quasi-static" because fields in free space are evaluated at distant points without regard to propagation delay, which is small compared to timescales within conductive media.

[16] The definition of "high" versus "low" frequency in the loss tangent obviously depends on both permittivity and conductivity, but the large natural variations in the latter imply that it is usually used to define the inductive-to-propagative transition. For a typical terrestrial near-surface conductivity of 3×10^{-3} S/m and dielectric constant of 7, $\sigma/\omega\varepsilon = 1$ at $f = 10$ MHz. Frequencies in the ground much less than this value (say 1 MHz and below) are diffusive, whereas frequencies in the ground much greater (of order 100 MHz and above) are propagative. In practice, the conductivity and dielectric constant are frequency dependent, but this order-of-magnitude estimate illustrates why terrestrial ground-penetrating radars operate in the VHF band but inductive measurements are made in the ULF to MF bands. For Mars the lower ground conductivity will shift the transition from diffusion to propagation to lower frequencies.

3.2. Plane-Wave Response

[17] The EM response of a layered medium to vertically incident plane waves at arbitrary frequency is computed by a recursive procedure [*Wait*, 1970]. The intrinsic impedance η_j of the jth layer is defined as

$$\eta_j = \left(\frac{i\mu\omega}{\sigma_j + i\omega\varepsilon_j} \right)^{1/2}, \quad (2)$$

where σ_j and ε_j are the conductivity and permittivity, respectively, of the layer. The wave or apparent impedance Z_j of the layer is

$$Z_j = \eta_j \frac{Z_{j+1} + \eta_j \tanh(ik_j h_j)}{\eta_j + Z_{j+1} \tanh(ik_j h_j)}, \quad (3)$$

where h_j is the layer thickness and $j = 1$ is the layer nearest the surface. The recursion is begun at the lowermost layer with the intrinsic impedance of the underlying half-space substituted for the apparent impedance of a layer below at $j + 1$. The apparent resistivity ρ_a is calculated from the apparent impedance of the top layer:

$$\rho_a = |Z_1|^2/\omega\mu. \quad (4)$$

The procedure is repeated at each frequency of interest. A plot of f (or period) versus ρ_a is the fundamental tool for one-dimensional (1-D) magnetotelluric interpretation and will be the focus of this paper. The phase of the impedance is often inverted jointly with the apparent resistivity; such considerations relevant to the inverse problem are neglected here, as well as many auxilliary quantities that are useful for 2-D and 3-D interpretation and for assessing noise.

[18] The assumption of vertical incidence is commonly made in terrestrial magnetotellurics because it both simplifies the computations for energy partitioning at subsurface interfaces and eliminates the need for knowledge of the source-field geometry. It is an excellent approximation within the subsurface because EM energy is strongly refracted downward at the planetary surface owing to the great contrast in material properties. The general, impedance-based version of Snell's law [e.g., *McNeill and Labson*, 1991] can be used to show that even for grazing incidence (89°) and an anhydrous Mars, wave normals are within 15° of vertical at 10 kHz and within 0.001° at 1 Hz. Further consideration to source structure is given below.

3.3. Heterogeneity and Resolution

[19] Although formal solution of the inverse problem for conductivity structure from EM data is beyond the scope of this study, some comments on expected resolution of aquifers on Mars are appropriate. The resolution of all diffusive methods is logarithmic with distance, whereas that of wave methods varies linearly. Therefore the resolution of low-frequency EM soundings can be expected to be poorer than radar, assuming the latter performs optimally. The resolution of diffusive EM methods varies with the size, shape, depth, and magnitude of subsurface resistivity contrasts as well as with the field components measured. In general, lateral resolution is comparable to a skin depth or $1/2\pi$ wavelength in the medium. For example, lateral contacts are detectable when closer than about one skin depth, which is different on either side of the contact [*Vozoff*, 1991]. A corollary is that one-dimensional modeling is valid more than about a skin depth away from such contacts, or when the lateral variations in conductivity structure are slow with respect to the skin depth. When the sensor is not in contact with the target, as will occur for airborne platforms or for high-resistivity overburden, additional allowance must be made for geometrical spreading [e.g., *Wait*, 1955, 1956]. As a rule of thumb, the lateral resolution in these cases is comparable to the vertical separation between the measurement and the target. For Mars, aquifers at depths of several kilometers may be expected to be defined laterally to a resolution of order 1 km, whereas horizontal discrimination of aquifers at depths of a few hundred meters will be of order 100 m.

[20] Vertical resolution is assessed by the ability to detect an embedded resistive or conductive layer within a half-space. This approach leads to simple formulae but, of course, may not apply to regions of complex layering or strong lateral heterogeneity. In relatively simple environments with good signal levels, 10% changes in apparent resistivity can be reliably distinguished [*Zonge and Hughes*, 1991]. Using this criterion, numerical experiments for a resistive layer embedded in a half-space [*Zonge and Hughes*, 1991] have shown that the layer can be resolved when its thickness exceeds 20% of its depth. EM is generally insensitive to the exact magnitude of a resistor as eddy currents are not efficiently induced there; furthermore, signal levels may be high enough for reliable characterization of a resistor only when the electric field is measured (e.g., magnetotelluric (MT) methods; see below).

[21] EM methods are, of course, more sensitive to conductors, and so detection of a conductive layer scales with the background-normalized conductivity of the target σ': a conductive layer can be resolved when its thickness exceeds $0.2/\sigma'$ times the depth to the target for $\sigma' > 2$ [*Zonge and Hughes*, 1991]. The thickness of a conductor is harder to determine because of equivalence, wherein different structures have nearly identical EM responses. For conductors that are either very thick or very thin with respect to a skin depth, the EM response is controlled solely by the conductance $S = \sigma h$, where h is the conductor thickness [*Kaufman*, 1994]. Therefore aquifers of different thickness, porosity, and salinity can all give the same EM response. Where the skin depth is comparable to the conductor thickness, this ambiguity can be partly resolved. The trade-off between porosity and salinity remains, but because likely porosities lie within an order of magnitude, the salinity can be constrained to a similar level of confidence.

[22] Aquifers on Mars are likely to have conductivities many orders of magnitude greater than their surroundings (see below), so detectable thicknesses may be quite small, even if the criteria are made more stringent. The issue is therefore not likely to be detection, but separation of equivalence factors above. A deep subcryospheric vadose zone may appear as a resistor, and therefore its thickness must exceed several hundred meters under the nominal model to be detected under good conditions. If poorer signal-to-noise levels require a 50% change in resistivity, the thickness of a detectable resistor is equal to its depth [*Zonge and Hughes*, 1991], and therefore a deep subcryospheric vadose zone would have to be several kilometers thick to be detected.

[23] Lateral variations in conductivity pose additional difficulties for terrestrial EM measurements apart from geometrical complexity, but these are not likely to strongly influence soundings on Mars. Measurements of apparent resistivity that include the electric field are subject to broadband displacements or "static shift" because of the high sensitivity of the electric field to near-surface conductivity heterogeneity [e.g., *Vozoff*, 1991]. These are commonly variations in the weathering layer on Earth; without moisture, even heavy clay concentrations will not be conductive on Mars. Another terrestrial issue is current channeling [*McNeill*, 1990; *Vozoff*, 1991]: the equations developed above assume that subsurface currents are purely inductive, but in fact galvanic currents flow too. Conductive structures will gather or channel current, which can also introduce broadband errors. Again, the low conductivity of rocks in the absence of liquid water will not permit much galvanic flow between aquifers and their surroundings, and so this too may be ignored at present.

4. Material Properties

[24] The crust of Mars is electromagnetically modeled as a three-component mixture of anhydrous rock, pure water ice, and liquid water containing dissolved solids. Each hydrostratigraphic zone is assigned different constraints on each component. Three steps are outlined below toward this end. First, the temperature- and frequency-dependent electical conductivity and dielectric permittivity of the components are given. Second, mixing models used to combine their properties are described. Third, the specific application of to each zone is outlined.

4.1. Electrical Properties of Rock, Ice, and Water

[25] The total electrical conductivity of rock can be expressed as the sum of frequency-independent and frequency-dependent components [*Keller*, 1982]:

$$\sigma_R = \sigma_{Rdc} + \sigma_{Rac}. \tag{5}$$

The frequency-independent portion is a function of temperature through a sum of Ahrennius relations,

$$\sigma_{Rdc} = A_1 \exp(-Q_1/kT) + A_2 \exp(-Q_2/kT), \tag{6}$$

where A_1 and A_2 are constants, Q_1 and Q_2 are activation energies, k is Boltzmann's constant, and T is absolute temperature. For basalt, $A_1 = 0.7$ S/m, $A_2 = 10^7$ S/m, $Q_1 = 0.57$ eV, $Q_2 = 2$ eV, and for peridotite, $A_1 = 4$ S/m, $A_2 = 10^7$ S/m, $Q_1 = 0.81$ eV, $Q_2 = 2.3$ eV [*Keller*, 1988]. The frequency-dependent component contains two terms that are functions of temperature

$$\sigma_{Rac} = A_3 \omega^{n_{ac}}. \tag{7}$$

The temperature dependence of the two parameters,

$$\begin{aligned} A_3 &= -2.55 \times 10^3/T - 3.31 \quad T < 300 \\ A_3 &= -970/T - 7.6 \qquad\quad T > 300, \end{aligned} \tag{8}$$

and

$$n_{ac} = -5.06 \times 10^4/T^2 + 4.84 \times 10^2/T - 0.286 \tag{9}$$

were derived from figures of *Keller* [1982] for basalt and are assumed to apply to peridotite also.

[26] The loss tangent for dry rocks is observed to be approximately independent of frequency over several decades at low frequency ($\sim 10^{-3}$ to 10^3 Hz [*Keller*, 1982]). The temperature- and frequency-dependent permittivity can be calculated from the conductivity and loss tangent. In practice, n_{ac} is less than unity and decreases with increasing temperature, so the frequency-dependence of the permittivity of dry rock is weak enough to be ignored for the purposes of this study. Therefore the dielectric constant is held at 7, appropriate to rocks and minerals with density 2.5–3 g/cm^3 [*Keller*, 1988].

[27] The resonant loss or complex dielectric relaxation of liquid water occurs at frequencies >1 GHz, and so the conductivity and permittivity of groundwater can here be considered to be independent of frequency. Any dependence of permittivity on dissolved solids is neglected, leaving the relative dielectric constant solely a weak function of temperature (derived from *Keller* [1988]):

$$\varepsilon_{rW} = 87 - 0.32(T - 273). \tag{10}$$

The permittivity is then $\varepsilon_W = \varepsilon_0 \varepsilon_{rW}$.

[28] The conductivity of groundwater is a strong function of the concentration of dissolved solids. Analytic expressions for the conductivity of groundwater with dissolved NaCl were derived from figures of *Keller* [1988]:

$$\begin{aligned} \log \sigma_W &= \log C - 1 + (T - 273)/150 \quad (\log C < 2.25) \\ \log \sigma_W &= \text{const} \qquad\qquad\qquad\quad (\log C > 2.25), \end{aligned} \tag{11}$$

where C is the concentration of dissolved solids in g/L. The conductivity is limited as the solution approaches saturation ($\sim$360 g/L for NaCl at 20°C). Conductivities due to other salts at 20°C are within a factor of 3 of NaCl [*Keller*, 1988], so the latter is taken to be representative of all dissolved solids. No separate provision is made for steam or supercritical water, but the results are insensitive to these distinctions because skin depths at the frequencies of interest do not penetrate deeply enough when groundwater is present.

[29] In contrast to liquid groundwater, relaxation losses in ice occur at tens of kilohertz and below. Ice behaves electrically as an

overdamped linear (Debye) oscillator with the relative dielectric constant given by

$$\varepsilon_{rI} = \varepsilon_{rI}^{\infty} + \frac{\varepsilon_{rI}^{0} - \varepsilon_{rI}^{\infty}}{1 + \omega^2 \tau_I^2}, \tag{12}$$

and the conductivity is

$$\sigma_I = \varepsilon_0 \tau_I \omega^2 \frac{\varepsilon_{rI}^{0} - \varepsilon_{rI}^{\infty}}{1 + \omega^2 \tau_I^2}, \tag{13}$$

where $\varepsilon_{rI}^{0} \cong 75$ and $\varepsilon_{rI}^{\infty} \cong 3$ are the zero- and infinite-frequency asymptotes, τ_I is the relaxation time constant, and the permittivity is again $\varepsilon_I = \varepsilon_0 \varepsilon_{rI}$. The relaxation time constant follows an Ahrennius relation [*Chyba et al.*, 1998]:

$$\tau = A_4 \exp(Q_4/kT), \tag{14}$$

with $A_4 = 5.3 \times 10^{-16}$ s and $Q_4 = 0.57$ eV.

4.2. Multicomponent Mixing

[30] The conductivity of water-bearing rock has been well described for more than half a century by Archie's law:

$$\sigma_{WR} = \phi \gamma \sigma_W \varphi^m, \tag{15}$$

where σ_{WR} is the composite rock-water conductivity, ϕ is the porosity, and γ and m are constants. Typical values for γ and m are 0.6–1.4 and 1–2, respectively [e.g., *Keller*, 1988]. Archie's law neglects the rock conductivity σ_R, and therefore there is no lower limit to conductivity with decreasing porosity or groundwater conductivity. A variety of two-component mixing models can be used to include the finite rock conductivity; here the Modified Brick-Layer Model (MBLM) of *Partzsch et al.* [2000] is adopted:

$$\sigma_{WR} = \frac{1}{\frac{1-\alpha}{\sigma_W} + \frac{\alpha}{\sigma_W(1-\alpha^2)+\sigma_R\alpha^2}}, \tag{16}$$

where $\alpha^3 = 1 - \phi$ (note the minor misprint in the *Partzsch et al.* [2000] version). The MBLM assumes that the fluid phase is distributed as films on the surfaces of cubic solids. It is an excellent approximation to Archie's law with the parameters of the latter set to $\gamma = 1$ and $m = 1.1$–1.2. Furthermore, the MBLM closely approximates the Hashin-Shtrikman upper bound (HS+) for conductivity [*Hashin and Shtrikman*, 1962; *Mavko et al.*, 1998]; this latter model assumes no specific geometry of the constituents except that one component (here, the fluid) is interconnected. The commonly used Maxwell-Wagner and Waff models for spherical inclusions are also equivalent to HS+ [*Partzsch et al.*, 2000; *Mavko et al.*, 1998] and hence the MBLM. Finally, the conductivity computed by these models is within a factor of 2 of that calculated from a simple parallel-plate model, which gives a stringent upper bound on conductivity. The coincidence of the empirical Archie's law with theoretical models attests to the strong interconnectivity of fluid pore spaces and the insensitivity of gross conductivity to specific pore geometry.

[31] For partial saturation ψ of the pore space, Archie's law is $\sigma_{WR} = \gamma \sigma_W \phi^m \psi^2$. The MBLM can be equivalently corrected by multiplying ϕ by ψ^2. For cases in which a rock-ice-water mixture is considered, water is still assumed to be the interconnected phase, and so the conductivity of the rock-ice portion is computed first using the parallel-plate model and then the conductivity of the composite solid and the liquid is subsequently determined by the MBLM. The same saturation-corrected MBLM can be independently applied to the permittivity [*Berryman*, 1995; *Mavko et al.*, 1998].

4.3. Clays

[32] The model described above assumes that the rock component is dry basalt. Departures from this simple end-member, including other primary rock types as well as alteration products, could potentially influence EM sounding for groundwater. Andesite is also abundant at the surface of Mars [*Soderblom*, 1992; *Bandfield et al.*, 2000], but its electrical properties [*Keller*, 1988] are insufficiently different to require distinction of primary rock composition. Evidence for crystalline clay minerals on Mars is still equivocal, although weathered material may be present amorphously as palagonite [e.g., *Soderblom*, 1992; *Bandfield et al.*, 2000]. Clay minerals are often considered to be electrically conductive, but it is in fact ion exchange with pore water that dominates the conductivity: very dry clay is a relatively poor conductor. As ion exchange increases with specific surface area, which in turn is maximized for sheet-silicate structures, clay minerals are assumed to provide upper bounds to the electrical properties of all potential weathering products on Mars.

[33] Explicit modifications to Archie's law used in oil and gas exploration account for the presence of conductive clay or shale, often as a function of cation exchange capacity. A simpler approach is taken here. *Keller*'s [1988] review showed that the minimum conductivity of pore water could be related to the amount of clay present; this in turn can be expressed in terms of the equivalent concentration of dissolved solids. Even with very little clay present, the minimum conductivity was ~0.003 S/m, which corresponds to an equivalent NaCl concentration of ~0.025 g/L. The pore-water conductivities for moderate and heavy clay abundances were found to be 0.1 and 10 S/m, respectively, or 0.7 and 7 g/L equivalent NaCl, respectively. The equivalent pore-water salinities for very little, medium, and heavy clay will be rounded to 0.03, 1, and 10 g/L. The dielectric constants of dry clays (4–8 [*Keller*, 1988]) are also insufficiently distinct from rock to warrant special consideration, and changes due to moisture are neglected.

[34] Clay cation exchange also introduces dielectric relaxation losses [*Olhoeft*, 1985]. The changes in conductivity as a function of frequency (dispersion) are usually less than a factor of 2; while these subtle effects may be useful in identifying clay-cation exchange on Mars, they are small compared to the overall signatures of groundwater and will be ignored here.

4.4. Adsorbed Water

[35] Water becomes loosely attached to mineral surfaces owing to the difference in molecular structure between the mineral and the bulk pore water. This adsorbed water can have the properties of a liquid [*Anderson and Tice*, 1973]; that is, ions and solutes as well as the water molecules themselves are mobile over thicknesses up to several monolayers of water or greater. Because of this mobility, a small amount of adsorbed water can greatly increase the electrical conductivity of dry rock. *Olhoeft* [1976] reported an "order-of-magnitude" increase in the DC conductivity (probably actually measured between 1 mHz and 1 Hz) of dry basalt at 25°C when 0.01 wt % of water was added and claimed that 0.002 wt % was detectable. At 10 Hz, *Olhoeft* [1976] stated that "more than a physisorbed monolayer" was required for detection. A simple electrical model for the DC behavior of adsorbed water assumes that Archie's law or the MBLM can be directly applied to the volume of adsorbed water, adjusted for relative saturation, and perhaps subject to a cutoff when less than about a monolayer is present. This model is developed and tested below.

[36] The quantity of adsorbed water has been studied extensively in terrestrial permafrosts. NMR spectra have indicated decreasing but significant water mobility down to −40°C [*Ander-*

Table 1. Test of MBLM Applied to Unfrozen Water in Permafrost

	$W_u(-1°C)$ / $W_u(-10°C)$	$V_u(-1°C)$ / $V_u(-10°C)$[a]	Predicted σ $\sigma(-1°C)/\sigma(-10°C)$	Observed $\sigma(-1°C)/\sigma(-10°C)$
Clay	6	5–6	5–7	3–10
Gravel	10	9–10	11–13	~10
Basalt	150[b]	140–150	240	~100

[a] Assuming $\rho_s = 1-3$ g/cm^3.
[b] Computed from equation (17) using $A_s = 0.25$ m^2/g.

son and Tice, 1973]. A composite relation for the approximate weight fraction of unfrozen water W_u is

$$W_u = 0.01 \exp\left[0.2618 + 0.5519 \ln A_s - 1.449 A_s^{-0.264} \ln(273-T)\right], \quad (17)$$

where T is the absolute temperature and A_s is the specific surface area in m^2/g [*Anderson and Tice*, 1972]. The volume fraction of unfrozen water is then

$$V_u = [1/W_u - 1)/\rho_s + 1]^{-1}, \quad (18)$$

where ρ_s is the soil or rock grain density. Table 1 compares the changes in weight fraction of unfrozen water to the change in conductivity over the range $-1°C$ to $-10°C$, from data compiled by *Scott et al.* [1990]. The predicted change in conductivity is computed from the change in volume of unfrozen water using the MBLM with zero host conductivity, which is equivalent to Archie's law with $n = 1.1$. The relative saturation is assumed to be unity. The agreement is excellent for clay and gravel but is off by a factor of ~2 for solid basalt. This is still reasonable given that the unfrozen water weight for this case was not given and was instead computed from (17).

[37] The MBLM at very low water content was compared to *Olhoeft* [1976] by assuming that the basalt contained very little clay (pore-water conductivity 0.03 S/m) and had a porosity of 3–10%. The relative saturation of water then varies from 1 to 0.3%, respectively. The predicted change in conductivity for basalt at 25°C is a factor of 45 at $\varphi = 3\%$ and a factor of 14 at $\varphi = 10\%$. This is in sufficiently good agreement with Olhoeft's reported "order-of-magnitude" change that the MBLM can be confidently expected to predict conductivity even at very low water content and saturation to within an order of magnitude.

[38] The weight fraction of adsorbed water can be related to the number of H_2O monolayers N_M as

$$N_M = 10^{-20} W_u (d_w)^2 / A_s m_w, \quad (19)$$

where d_w is the diameter (~2.8 A) and m_w is the mass (3×10^{-23} g) of the H_2O molecule.Equations (17) and (19) can be combined to calculate the number of adsorbed monolayers present in frozen soil as a function of specific surface area and temperature or, alternatively, the minimum temperature such that one monolayer is present. For $A_s = 40-100$ m^2/g, appropriate to silty permafrosts [*Anderson and Tice*, 1973], the single-monolayer minimum temperature has a broad minimum at $-27°C$. This is a reasonable fit to the minimum mobility temperature of $-40°C$ given by *Anderson and Tice* [1973], especially considering that (20) is a composite fit and does not include extreme behaviors. Note that one monolayer of water is fully 1.5 wt % at $A_s = 40$, so the relatively large quantities of water adsorbed at high specific surface area are nonetheless spread thinly. Adsorbed water for basalt powder ($A_s = 6$ m^2/g) is predicted to thin below a single monolayer at $-18°C$. The same relations may be inverted to give A_s from W_u, T, and N_M, so that the specific surface area for *Olhoeft*'s [1976] basalt sample is 0.25 m^2/g, which is predicted to be unable to maintain one monolayer below $-7°C$. The specific surface area of Martian soil was estimated from the Viking Lander gas-exchange experiment to be ~17 m^2/g [*Ballou et al.*, 1978] but at greater depths could be <1 m^2/g, values appropriate to solid rock. Therefore interstitial unfrozen water could fall below a monolayer, and the interconnected conductivity paths that promote ionic conductivity would be lost, at temperatures as high as several degrees below freezing.

[39] Water is also adsorbed from the vapor phase (see *Kieffer and Zent* [1992] for a review). However, this component is not likely to be an important electrical conductor on Mars. In the upper cryosphere, water vapor is generated by sublimation from ice. Only about one monolayer of adsorbed water can exist here, because additional H_2O is more stable as ice [*Anderson et al.*, 1967]. As one monolayer is a strong lower bound for substantial ionic mobility, it is very doubtful that vapor-adsorbed water at subzero temperatures could provide significant electrical conductivity.

[40] Water vapor can also be generated by evaporation below the cryosphere. In this region, larger quantities of capillary water (i.e., held by surface tension) will dominate over adsorbed water. Therefore the effect of distributed groundwater in a subcryospheric vadose zone could be parameterized solely through the capillary specific retention; here the continuum will be restricted to fully unsaturated or fully saturated.

[41] Brine concentrations of various salts can lower the freezing point by up to 50 K [*Brass*, 1980; *Mellon and Phillips*, 2001]. This will move the bottom of the cryosphere at most from 6.2-km to 2.9-km depth at the nominal heat flux and thermal conductivity [see also *Clifford*, 1993] or from 140 m to 65 m in the insulating-regolith model. As the depth to groundwater is the most critical factor affecting the EM sounding response and it is illustrated through the background thermal properties, no specific provision is made at present for freezing-point depression due to salinity. Another major obstacle to including this effect is that the variation of unfrozen water with salt type and concentration is unknown.

[42] The final model for the electrical conductivity of adsorbed water computes the unfrozen volume fraction in the ice-rich cryosphere using $A_s = 6$ m^2/g, a value characteristic of basalt powder but logarithmically intermediate between solid rock and soils at the Viking site. The saturation is taken to be unity, and the electrical conductivity is set to zero below $-20°C$, the predicted single-monolayer minimum temperature for basalt powder. At 10 Hz, logarithmically intermediate to the frequencies of interest here, more than a single monolayer was required to measure any change in electrical properties at room temperature [*Olhoeft*, 1976]; thus this model ensures that the conductivity is being overestimated.

[43] A variety of other effects, mostly relaxation losses due to different kinds of energy barriers, have been observed or inferred in terrestrial permafrosts [*Olhoeft*, 1977]. The only low-frequency inorganic mechanism not accounted for here was an interfacial relaxation loss in the range 10–300 Hz. As ionic conduction still appeared to dominate in this frequency band, such losses are ignored.

4.5. Iron Oxides

[44] The presence of large amounts of iron in the crust of Mars introduces several potential complications owing to the higher

conductivity and permeability and possible dispersive effects, particularly for the latter in permeability. Iron, expressed as Fe_2O_3, comprises ~18 wt % of soils at both the Viking and Pathfinder sites [*Clark et al.*, 1982; *Rieder et al.*, 1997]. *McSween et al.* [1999] calculated that a nominal sulfur-free rock at the Pathfinder site would contain 12 wt % FeO. The corresponding normative abundance of iron-oxide minerals was computed to be <2 wt %. Assuming a soil density of 1.5 g/cm^3, a rock density of 2.7 g/cm^3, and an average iron-oxide mineral density of 5 g/cm^3, the volumes of iron-oxide minerals in the soil and rock are 5% and 1%, respectively (an alternative calculation for the rock, based on weighting the mineral norms by their relative number of oxygens, gives a similar result). *Madsen et al.* [1999] determined that maghemite (γ-Fe_2O_3) is the most likely magnetic mineral in Martian dust. They estimated maghemite at 6 w t% (implicitly assuming that the dust has the same Fe_2O_3 abundance as the soil). This, in turn, would translate to a minimum volume of ~2%, again assuming that the maximum density of the dust is that of the soil. The abundance and nature of iron oxides over the full range of depths of interest here (kilometers or more) are unknown.

[45] It is straightforward to show that the near-DC induced-magnetic contribution of μ for even relatively abundant maghemite is negligible. The relative permeability $\mu/\mu_0 = 1 + k_m$, where k_m is the dimensionless magnetic susceptibility. Taking $k_m = 3.7$ (from a mineral density of 5.1 g/cm^3 and a dimensional susceptibility of 7.2×10^{-4} m^3/kg [*Madsen et al.*, 1999]), the maximum increase in μ for even 10% maghemite by volume is then just 37%.

[46] The conductivity is more variable and difficult to evaluate but has greater consequences. Here all of the iron minerals, not just the magnetic carrier, can contribute. Measured magnetite conductivities range from 2×10^{-4} to 2×10^4 S/m, and those of hematite range from 1×10^{-7} to 300 S/m [*Telford et al.*, 1990]; the geometric mean of these extrema is 0.1 S/m. Terrestrial iron ores are observed to have conductivities ranging from 10^{-6} to 10 S/m [*Telford et al.*, 1990]; the geometric mean of all the tabulated values is ~10^{-3} S/m. The MBLM or equivalent Hashin-Shtrikman bounds can be used to estimate the conductivity of a silicate host containing conductive iron oxides. As these minerals are likely to be dispersed when present in primary igneous textures or when in unconsolidated materials such as dust and soil, it is appropriate to consider the conductive minerals as inclusions. Where the host conductivity is much smaller than the inclusions, the inclusions effectively have infinite conductivity and the MBLM predicts a hundredfold increase in the bulk conductivity over the conductivity of the host for 3 vol % inclusions. Given the many orders of magnitude contrast between groundwater and anhydrous rock, this increase in conductivity has no effect on the calculated sounding curves that include groundwater.

[47] If iron minerals become concentrated through hydrothermal, fluvial, lacustrine, or aeolian processes (effectively forming an ore deposit), then the conductivity could be much higher. The hematite deposits of Sinus Meridiani [*Christiansen et al.*, 2000] demonstrate that such processes do occur on Mars. The MBLM predicts that the same 3% concentration of conductive minerals, if electrically interconnected, would have a bulk conductivity ~1/60th that of the conductive phase, say ~10^{-5}–10^{-3} S/m. As these figures are comparable to the lower range of conductivities expected for aquifers (say, 3% porositity in the presence of only light clay), and higher iron-oxide concentrations could also be matched to greater porosity and/or salinity, it is likely that iron-ore deposits on Mars could be confused with subsurface water when compared solely on the basis of conductivity. Indeed, many kinds of metallic ores are conductive (the explosion in EM exploration following WW II was in response to the search for strategic metals, particularly in resistive terrains such as Canada), and so EM exploration on Mars would also be sensitive to such deposits. As with terrestrial exploration, independent geological and geophysical information, particularly the ability to map the three-dimensional shape of the conductor, will be important in discriminating between different hypotheses for the nature of the conductor.

[48] Iron-oxide minerals can have frequency-dependent permeability or dispersion that leads to magnetic relaxation losses. This phenomenon, also known as magnetic viscosity or superparamagnetism, has been observed in magnetite, hematite, and maghemite (see *Spies and Frischknecht* [1991] for a review). Because the characteristic relaxation time (compare to equation (13) above) increases exponentially with magnetic-domain volume, a broad range of frequencies can be affected by superparamagnetism. Lunar soils and low-grade breccias with large single magnetic domains have relaxation times of order 100 s [*Dunlop*, 1973] (resonance frequency ~10^{-2} Hz), whereas fine-grained Australian laterites relax in milliseconds [*Spies and Frischknecht*, 1991] (resonance frequency ~10^3 Hz). The very fine dust of Mars is anticipated to have relaxation times in the range of a fraction of a microsecond, corresponding to strong losses at frequencies of tens of MHz or greater [*Olhoeft*, 1998]. While potentially important for ground-penetrating radar, this lies well outside the frequency range of interest here. However, magnetic relaxation losses for polycrystalline magnetite, perhaps representative of Martian soil, peak around several hundred hertz [*Olhoeft and Strangway*, 1974] and therefore could affect low-frequency exploration. In active sounding, magnetic viscosity can be effectively eliminated by separating the source and receiver [*Buselli*, 1982], as the effect is strongest when the applied field magnetizes material in the immediate vicinity of the transmitter loop. In passive sounding, the effect would be recognized by its characteristic frequency-dependent amplitude (apparent resistivity) and phase behavior [*Olhoeft and Strangway*, 1974].

4.6. Other Materials

[49] In addition to groundwater, other fluids and ices have been proposed to exist on Mars. A crustal carbonate abundance of just 2% sequesters the equivalent of 1 bar of atmospheric pressure per kilometer of regolith [*Fanale et al.*, 1992]. Pure liquid CO_2 is a poor solvent compared to H_2O, and therefore ionic conduction, which dominates low-frequency electrical conductivity, is negligible. CO_2 dissolved in water can form a weak acid, enhancing solubility, but as the present goal is detection of groundwater, this is a moot point. *Olhoeft* [1998] proposed that clathrate hydrates (solid ice-like phases formed between gas and water molecules at low temperature and high pressure) can be detected electromagnetically. As the electrostatic molecular cage enclosing the gas is unlikely to promote ionic transport, the conductivity of these phases is expected to be unimportant, although relaxation-loss mechanisms may be detectable in the kHz-MHz range [*Olhoeft*, 1998]. As a whole, however, low-frequency EM methods are relatively insensitive to CO_2; if the cryosphere of Mars is dominated by CO_2 and not H_2O [*Hoffman*, 2000], there will be little anomalous electrical conductivity.

[50] Earth-based radar has detected a region of low reflectivity and high absorption to the west of Tharsis, dubbed "Stealth," which has been interpreted as volcanic ashfall deposits [*Muhleman et al.*, 1991]. Modeled loss tangents indicate an electrical conductivity of ~10^{-2} S/m at radar frequencies. Such conductivity is very high compared to expected values for Mars and is more typical of Earth, so some network for conduction, whether as water, moist clays, or iron minerals, must be present. Buried "stealth" layers would then pose similar obstacles to deep sounding as would ore deposits.

5. Plane-Wave Responses

[51] On the basis of the expected distribution of subsurface water and ice on Mars and the EM properties of these materials, a

Table 2. Models Tested

Model	Figure	Description	Cryospheric Unfrozen Water	Subcryospheric Aquifer	Subcryospheric Structure[a]	Dissolved Solids, g/L	Insulating Regolith, m
1	3, 4, 13, 15	anhydrous	–	–	–	–	–
2	4–6, 15	ice[b]	–	–	–	–	–
3a	5	deep aquifer, fresh water	–	✓	–	0.03	–
3b	5	"	✓	–	–	0.03	–
3c	5, 8, 15	"	✓	✓	–	0.03	–
4a	6	deep aquifer, brine	–	✓	–	360	–
4b	6, 7	"	✓	–	–	360	–
4c	2, 6–10	"	✓	✓	–	360	–
4d–4g	7	"	✓	✓	✓	360	–
5a, 5b	8	deep aquifer	✓	✓	–	1,10	–
6b	11	shallow aquifer, brine	✓	–	–	360	200
6c	9–11, 14, 15	"	✓	✓	–	360	200
6d, 6e	9, 10	"	✓	✓	–	360	50,100
6f, 6g	11	"	✓	✓	✓	360	200

[a] Vadose zone or aquifer with imposed bottom boundary.
[b] Models 2a and 2b use 50% uniform porosity; all others use 20% exponential porosity structure (see text). All models have ice-saturated cryospheres except model 1 (no ice) and model 2a (500-m mear-surface dessicated zone).

variety of models can be constructed to test the plane-wave EM response. To facilitate description, each model is given an alpha-numeric designation (Table 2) and the models are illustrated schematically in Figure 1.

[52] The background compositional structure consists of a 50-km-thick basalt crust [*Zuber et al.*, 1999] overlying a peridotite mantle (model 1). A fundamental distinction in the models is whether the cryosphere is thick (several kilometers; models 2–6) or thin (hundreds of meters; model 7). For thick-cryosphere models the thermal structure consists of a linear geothermal gradient to the base of the lithosphere at 1600 K, below which temperatures are considered to be constant. Modeling of the entire lithosphere is

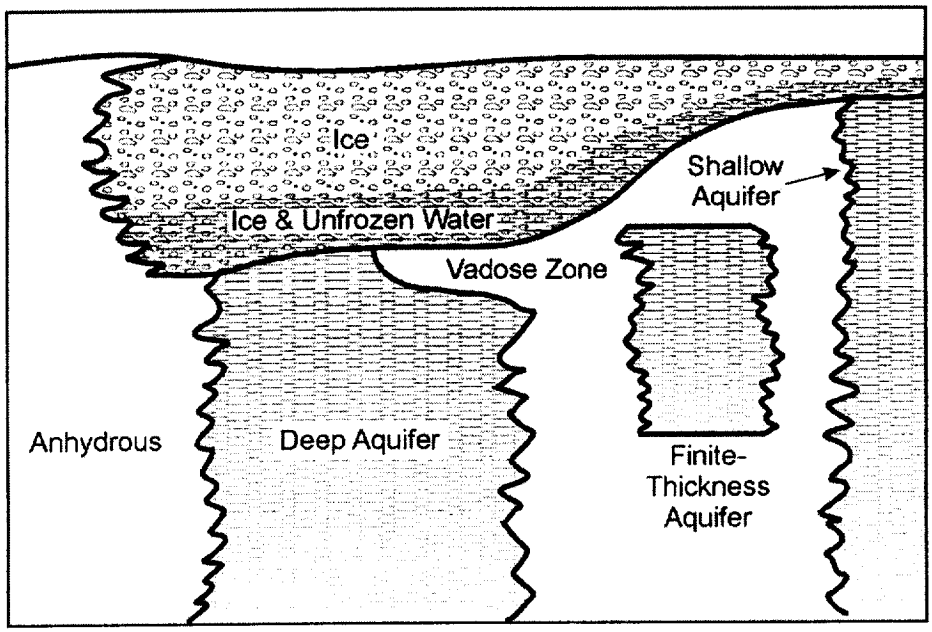

Figure 1. Cartoon of possible distributions of Martian subsurface water and ice considered in this paper. Cryosphere can contain ice and, at greater depths, unfrozen, adsorbed water in contact with formation. Thick cryosphere and deep aquifers (several kilometers) correspond to nominal geotherm; thin cryosphere and shallow aquifers (hundreds of meters) may be found under higher geotherms or other, perhaps unusual, conditions. Crustal-scale aquifers are nominally considered to gradually terminate with depth owing to decreasing porosity; alternatively, discrete aquifers may be bounded by underlying aquitards. Also, drainage of water may lead to formation of subcryospheric vadose zone.

necessary for the anhydrous models owing to the very large skin depths of low frequencies in resistive rock. Radioactive heating in the crust is neglected. The geotherm is determined assuming a thermal gradient of 30 W/m^2 [*Schubert et al.*, 1992] and a thermal conductivity of 2.0 W/(m K) (values of 1.5–3 W/(m K) are initially compared). For thin-cryosphere models the thickness of regolith with thermal conductivity of 0.045 W/(m K) is specified, and so the geotherm consists of two linear segments. Layering and other sources of dielectric scattering within the dry crust (potentially critical to radar response) can be ignored here, as the principal contributor to low-frequency sounding is the electrical conductivity.

[53] Away from the polar regions, ice in the cryosphere has likely been sublimated to depths up to a few hundred meters [*Clifford and Hillel*, 1983; *Fanale et al.*, 1986]. Allowance is made in one model for complete desiccation to a representative depth of 200 m, but in other models ice is assumed to extend to the surface.

[54] A mean annual surface temperature of 180 K is adopted, representative of 60° latitude. This value was chosen for the middle- to high-latitude regions where gullies have been observed [*Malin and Edgett*, 2000] as potential indicators of shallow groundwater under the thin-cryosphere models. The results for deep groundwater are less sensitive to the surface temperature and may be considered to be globally representative.

[55] With two exceptions noted below, the porosity for all models is 20% at the surface and decreases with depth with a scale height of 2.82 km [*Clifford*, 1993]. Where no explicit lower bound is specified, the decrease of porosity with depth effectively limits aquifer thickness. Alternative models are presented for explicit limits to aquifer thickness and for a finite unsaturated vadose zone separating the cryosphere and a subcryospheric aquifer.

[56] The frequency- and depth-dependent electrical permittivity and conductivity structures for a representative model (4c) are shown in Figures 2a and 2b, respectively. Note that the contrast in permittivity with depth is gradual and modest but the change in conductivity due to the presence of water is comparatively large and sharp.

[57] Reference models for a completely anhydrous Mars (Figure 3) show two distinct branches. At frequencies less than ~1 kHz, the apparent resistivity increases with frequency, which is the diffusive signature of greater conductivity at depth. Here the increase in electrical conductivity with temperature, which, in turn, increases with depth, causes longer wavelengths to sense a lower overall resistivity. The leading effect of increasing thermal gradient is to decrease the apparent resistivity at all frequencies within the diffusion regime.

[58] In the limit where the contrast between the resistor and conductor is large and the latter is treated as a half-space, the apparent resistivity is simply ρ

$$\rho_a = \mu\omega h^2 \tag{20}$$

and is known as an "h line" because it forms a straight line on a log-log plot and depends only on the thickness h of the overlying resistor [*Jiracek et al.*, 1995]. The existence of the conductor can be established by as few as two frequencies and its depth determined at any frequency from the apparent resistivity. The detailed forms of the subkilohertz responses in Figure 3 are not straight lines owing to the continuous variation of conductivity with depth. Furthermore, the change in material properties at the crust-mantle boundary produces an inflection, although this becomes less distinct at higher geotherms, where the differences in the electrical conductivity of basalt and peridotite are smaller. The apparent depth to the conductor (solving equation (20) for h) over the frequencies sensitive to the crust varies continuously but has a minimum value at 100 Hz of 25–50 km, depending on thermal gradient. At the lowest frequencies, which strongly penetrate the constant-conductivity asthenosphere, the apparent depth to the conductor increases as the reciprocal square root of frequency and therefore no longer has any meaning.

[59] The diffusive response in Figure 3 is idealized for a totally anhydrous, homogeneous crust and mantle. In practice, the depth of exploration may be limited by deep structure. On Earth both graphite and water have been considered as the source of prominent midcrustal conductors [see *Jiracek et al.*, 1995]. The effect of arbitrarily terminating vertical variations in conductivity at 30 km is also illustrated in Figure 3 for the nominal 15 K/km geotherm. The apparent resistivity departs from the previous curve below ~10 Hz and rapidly reaches an asymptotic value equal to the resistivity at the cutoff depth.

[60] At frequencies >1 kHz the response is propagative, and the signature is dominated by multiple reflections within a waveguide defined by the planetary surface and the effective depth to subsurface conductors. Peaks in apparent resistivity correspond to matched impedances and maximum leakage from the waveguide, whereas apparent-resistivity minima correspond to maximally mismatched impedance and maximum internal reflection. As the impedance mismatch at the plantary surface forms a vibration node, apparent-resistivity highs are analogous to open-tube resonances containing $n/4$ (n = 1, 3, 5,...) wavelengths in the vertical direction, and apparent-resistivity lows resemble closed-tube resonances with $n/2$ (n = 1, 2, 3,...) wavelengths. Because of the continuous variation in conductivity with depth, the modes are not regularly spaced, but subsurface properties could nonetheless be determined from their dispersion. The $1/f$ overall falloff in apparent resistivity is characteristic of a parallel RC circuit above its corner frequency.

[61] Subsurface ice is relatively difficult to detect electromagnetically unless it is massively segregated (Figure 4). Models 2a and 2b consider a sheet of ice to a depth of 1 km. Because of the impedance contrast at this interface, the high-frequency internal-reflection structure is altered at frequencies >10 kHz. This impedance boundary is almost entirely due to the contrast in dielectric constant at these frequencies; in essence, detection operates similarly to a radar.

[62] Where there is no distinct bottom to ice, the response >10 kHz has only minor differences with the anhydrous reference. However, if there is a substantial volume of warm ice (within ~20 K of melting), the relaxation loss can be identified at ~5–9 kHz (model 2d, Figure 4). The relaxation exists under Mars temperature conditions down to 0.01 Hz (Figure 2) but is very broad and weak at cold temperatures. The identified signal is therefore from the bottom kilometer of the cryosphere, and the center frequency ~8 kHz is due to the interaction between skin depth and peak ice conductivity as a function of temperature and frequency. The effect is nonetheless modest, just a factor of ~2 over background for even 50% uniform porosity. When the 20%-exponential porosity structure is used, these signatures vanish (model 2c; not shown).

[63] In contrast to ice, groundwater profoundly changes the shape of the sounding curves across a broad frequency range. Groundwater containing 30 mg/L dissolved solids (appropriate to equilibrium with basalt containing very little clay) would be considered very fresh yet still has sufficient ionic conduction to be strikingly detectable (model 3, Figure 5). A subcryospheric aquifer produces a distinct h line between ~300 Hz and a few kHz with a minimum apparent depth to a conductor of 7.4 km at 1 kHz. The formal bottom of the cryosphere is 6.2 km in this model. The simple h line analysis will always overestimate the depth to the conductor when conductivity decreases continuously

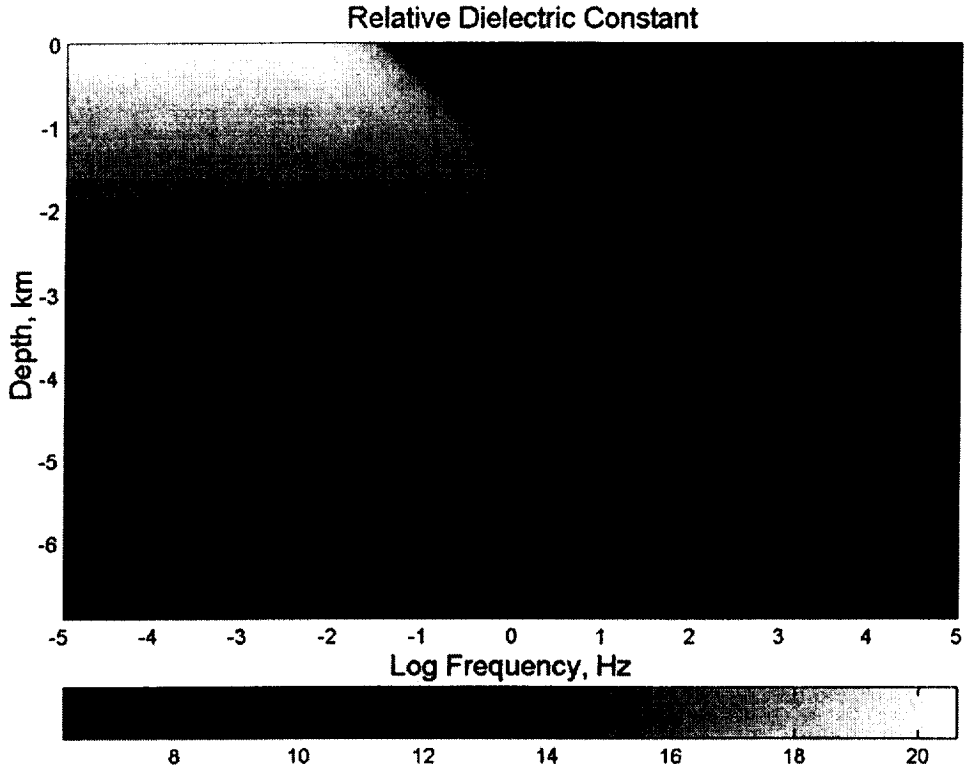
Relative Dielectric Constant
Depth, km
0
-1
-2
-3
-4
-5
-6
-5 -4 -3 -2 -1 0 1 2 3 4 5
Log Frequency, Hz
8 10 12 14 16 18 20

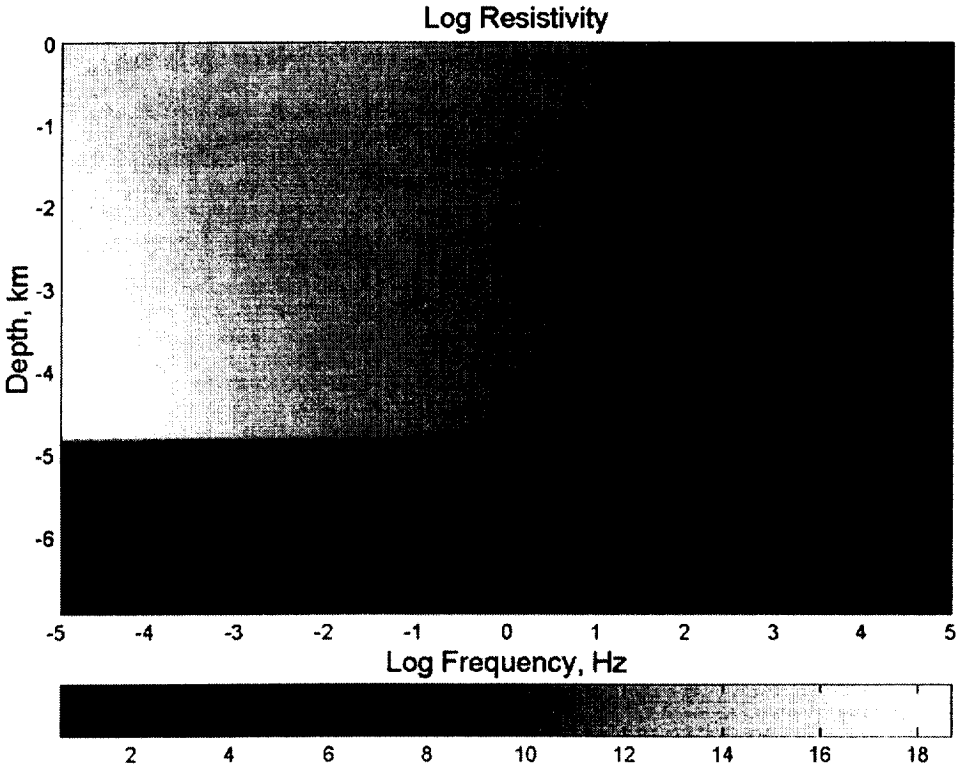
Log Resistivity
Depth, km
0
-1
-2
-3
-4
-5
-6
-5 -4 -3 -2 -1 0 1 2 3 4 5
Log Frequency, Hz
2 4 6 8 10 12 14 16 18

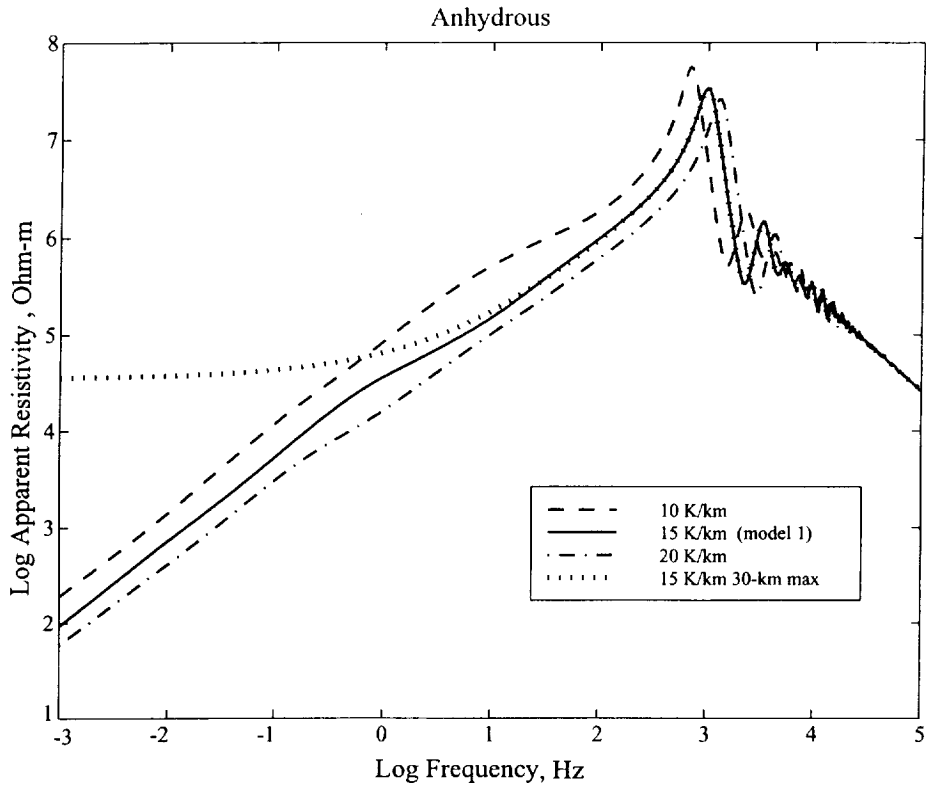

Figure 3. Apparent resistivity for vertically incident plane waves as a function of frequency and geothermal gradient, for anhydrous crust. In general, the effective depth of penetration in the diffusive regime increases to the left; decreasing apparent resistivity with decreasing frequency is therefore due to the decrease in true resistivity with increasing depth (temperature). Dotted curve disallows further decrease in resistivity below 30-km depth. Increase in resistivity of uppermost mantle causes inflection at 1 – 10 Hz. Higher-frequency trend of apparent resistivity inversely proportional to frequency is a signature of transition from diffusion to propagation; oscillations are reflection modes between planetary surface and high-conductivity lower crust.

with depth, but a formal inversion could likely determine the depth to the base of the cryosphere to within a few hundred meters (say, 10%) at this depth.

[64] Below ~300 Hz the trend of the h line is reversed, and eventually the curve asymptotes into the background trend for anhydrous crust: there is effectively no sensitivity to water below 10 Hz as the skin depth is now much greater than the aquifer depth or effective thickness. The intermediate portion of the curve showing increasing apparent resistivity with decreasing frequency also contains some information about water. In the limit where the structure can be considered to be a conductor overlying a resistive half-space, the apparent resistivity is

$$\rho_a = 1/\mu\omega S^2 \tag{21}$$

and is known as an "S line" because it depends only on the total conductance $S = \sigma h$ of the conductive overburden [*Jiracek et al.*, 1995]. Again, a formal inversion that accounts for the continuous change of conductivity with depth will produce better results than (21), but it will still be limited by electrical equivalence of the aquifer: the thickness of the aquifer cannot be measured independently of the conductivity.

[65] The high-frequency, propagative response is also strongly affected by an aquifer (Figure 5). The transition from diffusion to propagation shifts to a higher frequency and, because impedance contrasts are increased owing to the groundwater's high conductivity, the number and amplitude of internal-reflection modes are increased.

[66] Unfrozen water within the cryosphere has little effect on the curves when a subcryospheric aquifer is also present (Figure 5), because the greatest contribution from the unfrozen water is near the warm base of the cryosphere anyway. When the subcryospheric aquifer is not present, the propagative response to groundwater changes only modestly, as the unfrozen water can still support wave reflections in the cryosphere. However, the diffusive signa-

Figure 2. (top) Relative dielectric permittivity (dielectric constant) and (bottom) electrical conductivity for deep, briny aquifer (model 4c). Porosity decreases exponentially with depth and is everywhere saturated with ice or water; geothermal gradient is 15 K/km. The base of the cryosphere is formally at 6.2 km, but unfrozen water causes strong conductivity in the bottom kilometer of the cryosphere (note that dielectric contrast is modest). Relaxation loss in ice causes frequency- and temperature- (depth-)dependent transition between 0.01 Hz and 10 kHz. See color version of this figure at back of this issue.

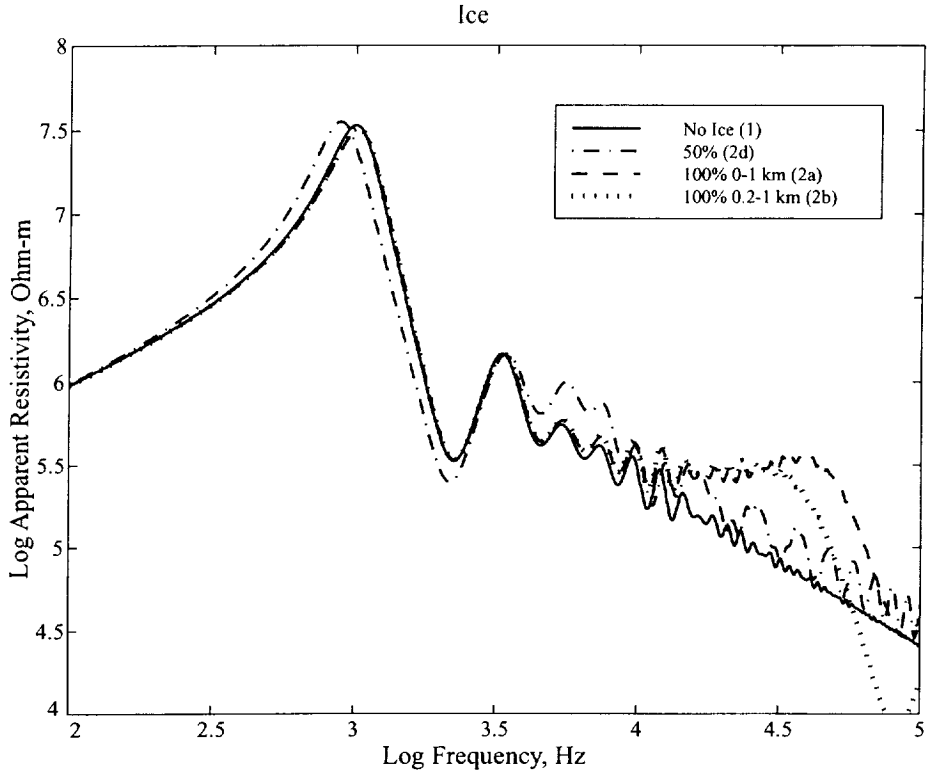

Figure 4. Apparent resistivity for ice-saturated cryosphere at 15 K/km. At 50% uniform porosity, deep, warm ice is distinguishable by increase in apparent resistivity due to relaxation loss in 5–9 kHz range. Shallow ice or depth to ice is indeterminate. Massively segregated ice and depth to ice are resolvable at >10 kHz owing to dielectric contrast, akin to radar. Ice in pore volume that decreases exponentially with depth is indistinguishable from anhydrous crust (model 2c).

ture is compressed to frequencies >100 Hz, with the critical h line section almost eliminated. The latter does still yield a minimum depth to a conductor of 6.4 km at 2.2 kHz.

[67] At an extreme groundwater salinity of 360 g/L (NaCl saturation at 20°C), the general pattern of the response is the same but is expanded to a greater frequency range (model 4, Figure 6). The h line for a subcryospheric aquifer now spans the range ~30 mHz to a few kHz; even the h line for unfrozen cryospheric water alone extends down to ~1 Hz. Because the skin depth within the brine-bearing formation is small (~100 m), the h line response is quantitatively an excellent approximation to a resistor over a conductor, with a minimum depth to the conductor of 5.2 km at 350 Hz determined from the h line. This is ~1 km shallower than the formal base of the cryosphere because the unfrozen brine within the cryosphere is itself a strong conductor (see Figure 2b). These patterns in Figure 6 can also be described as shifting the pair of S lines in Figure 5 down by about four and a half decades in frequency. The amplitude of variations in the wave regime (not shown) further increases, because the range of impedance contrasts has again been increased.

[68] In both examples (Figures 5 and 6) the signatures of aquifers of finite thickness and different positions below the cryosphere must all lie in between the curve for unfrozen cryospheric water (zero-thickness subcryospheric aquifer) and the curve for unfrozen water in contact with an infinitely thick subcryospheric aquifer. These curves achieve their greatest separation as S lines, where the sounding sensitivity is transitioning from the conductor to the basement. Therefore all useful discrimination information will be contained within the decade and a half of frequency that the two S lines span. Figure 7 illustrates the effect of variations of the thickness of a dry subcryospheric vadose zone and subcyrospheric aquifer for the high-salinity model of Figure 6. An unbounded aquifer that is separated from the cryosphere by a dry vadose zone is indicated by departures from the curve for a subcryospheric aquifer in contact with a cryosphere containing unfrozen water. A 1-km-thick vadose zone produces a maximum change in apparent resistivity of 50%. Placing a bottom boundary on a subcryospheric aquifer in contact with the cryosphere appears as departures from the curve for unfrozen water in the cryosphere. Relatively small thicknesses (~100 m) are significant because of the high conductivity of the brine; lesser salinity will proportionally increase the thickness required to produce the same curve. Again, this is equivalence: aquifers with different conductivity-thickness products can yield the same S line. Equivalence is minimized where the apparent skin depth (computed from the apparent resistivity, in contrast to the true skin depth within the conductor) is comparable to the conductor thickness [*Kaufman*, 1994], but this fortuitous combination may not exist; in this example the skin depths in the most sensitive frequency band are still several times the effective conductor thickness.

[69] The effect of salinity on models containing both unfrozen water in the cryosphere and a thick subcryospheric aquifer is shown in Figure 8. Groundwater in equilibrium with various clay abundances has concentrations of dissolved solids well below that of a brine, which results in a logarithmic displacement of the S line to higher frequencies. A bandwidth of six orders of mangitude, from ~1 mHz to ~1 kHz, is required to guarantee that the S line

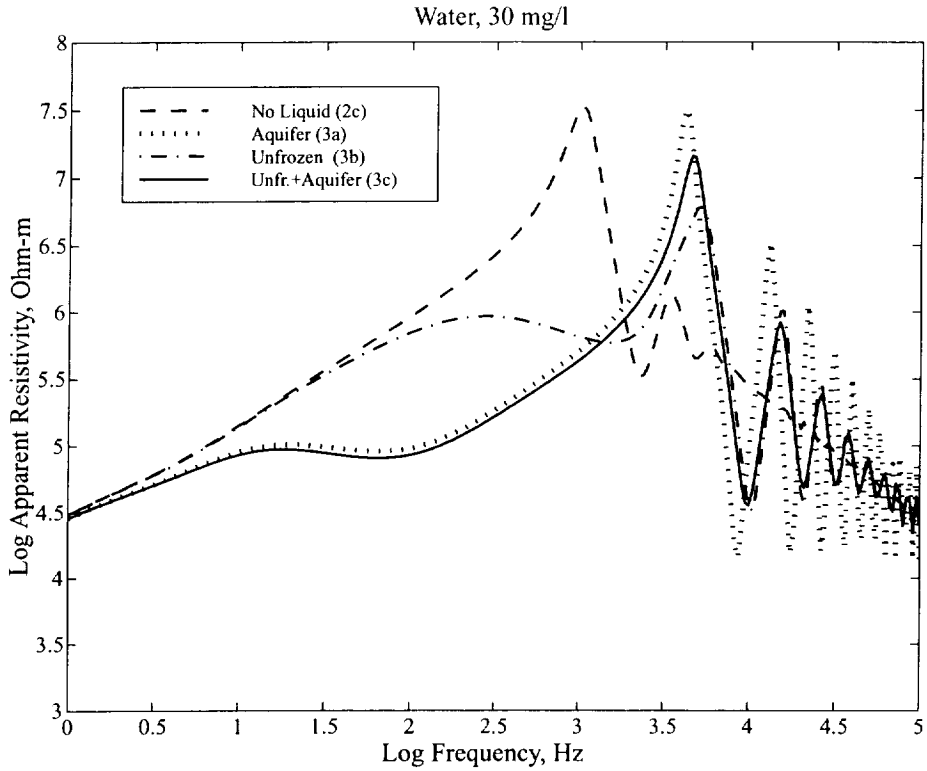

Figure 5. Apparent resistivity for models variably containing ice only (model 2c), ice and a subcryospheric aquifer (model 3a), ice and unfrozen water within the cryosphere (model 3b), and ice, unfrozen water within the cryosphere, and a subcryospheric aquifer (model 3c). Salinity is everywhere 30 mg/L, representative of fresh water. Water is detectable at all frequencies >10 Hz. For the last model the segment with positive slope from 100 to 1000 Hz ("*h* line") approximately gives the depth to groundwater, and the segment with negative slope from 30 to 50 Hz ("*S* line") approximately gives the total conductance, or conductivity-thickness product. In the wave regime the quarter-wavelength (maximum apparent resistivity) and half-wavelength (minimum apparent resistivity) modes for the surface-to-groundwater waveguide occur at 6 kHz and 10 kHz, respectively, and can also be used to determine the depth to water.

responses can be captured, and with them some attempt at estimating aquifer thickness. If a narrower bandwidth is necessary, the optimum frequency for detection of groundwater and determination of its depth (i.e., capturing a portion of the *h* line) is ~100 Hz to 1 kHz.

[70] The EM responses of models containing an insulating regolith were tested at a groundwater salinity of 360 g/L. For zero regolith thickness the nominal 15 K/km geotherm exists everywhere, but at the assumed regolith thermal conductivity the geotherm in the regolith is 667 K/km. Therefore 0°C is attained at depths as shallow as 140 m for a 200-m-thick insulating regolith. With most of the subsurface now containing water, the diffusion-to-wave transition is displaced to much higher frequencies, as high as several hundred kHz for a 200-km-thick regolith (Figure 9). The modal frequencies (reflections) shift in accordance with a shallower water table for the hotter temperatures associated with thicker regoliths. The low-frequency *h* lines have lower apparent resistivity and hence shallower depth to conductors. The *S* line transitions to basement (Figure 10) are progressively displaced to lower frequencies with thicker regoliths.

[71] The effect of finite thickness of an aquifer under an insulating regolith is similar to that for the deep aquifers, except the sensitive frequency band between the *S* lines for unfrozen water in the cryosphere and an unbounded aquifer in contact with such water now covers six decades of frequency instead of one and a half (Figure 11). Furthermore, there is much greater resolution of thin aquifers (~10 m) because the target is shallow and conductive. Again, these figures will decrease at lower salinity owing to equivalence.

6. Natural Electromagnetic Sources

[72] The natural electromagnetic spectrum of Earth is rich with signals that can be used for sounding. Some of these will exist at Mars, some will not, and Mars may have unique signals not observed on Earth. In this section, likely similarities and differences are reviewed.

[73] The low-frequency terrestrial spectrum can be divided into three major segments (Figure 12). At relatively high frequencies (>2 kHz) the Earth-ionosphere cavity acts as a waveguide that supports transverse-electric (TE) and transverse-magnetic (TM) plane waves. The principal source of natural energy here is lightning, and the waveguide permits regional-to-global propagation: thunderstorms in equatorial Africa, South America, and Indonesia can be detected worldwide. At lower frequencies (1 Hz–2 kHz), transverse-electromagnetic (TEM) plane waves and spherical (Schumann) resonances of the Earthionosphere cavity, also from lightning, are evident. All lightning energy is collectively called spherics, and the region >1 Hz is the spheric band. At the lowest frequencies (<1 Hz) the waveguide is ineffective, but energy can

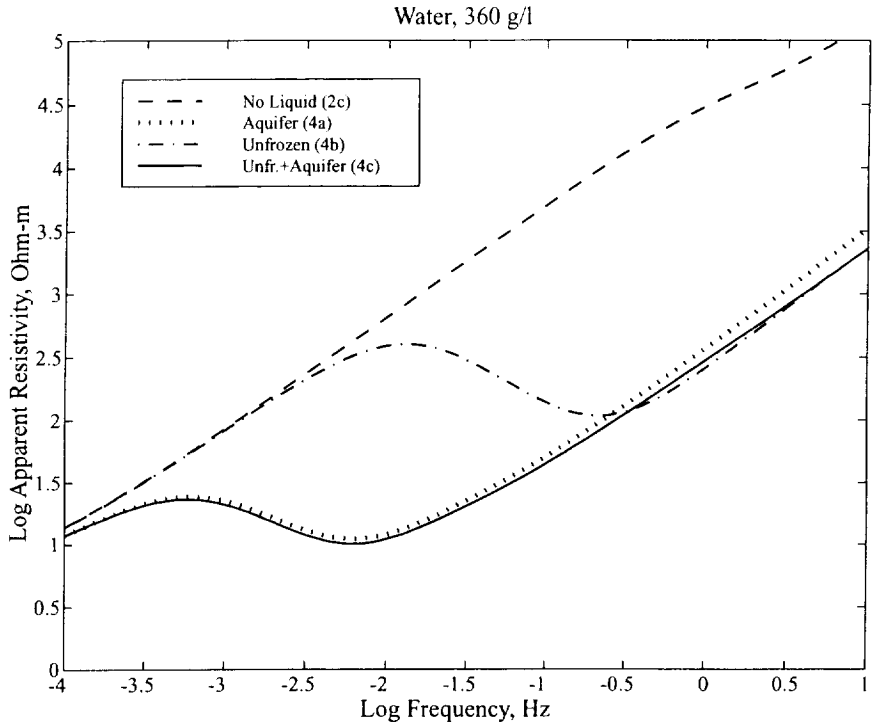

Figure 6. As Figure 5, but with groundwater salinity of 360 g/L, representative of saturated brine (models 4a–4c). Higher salinity shifts *S* lines (indicating transition from aquifer to basement) down about four and a half decades of frequency. Propagative transition is largely unchanged (not shown), so depth to water can be determined anywhere along *h* line from 1 Hz to 1 kHz.

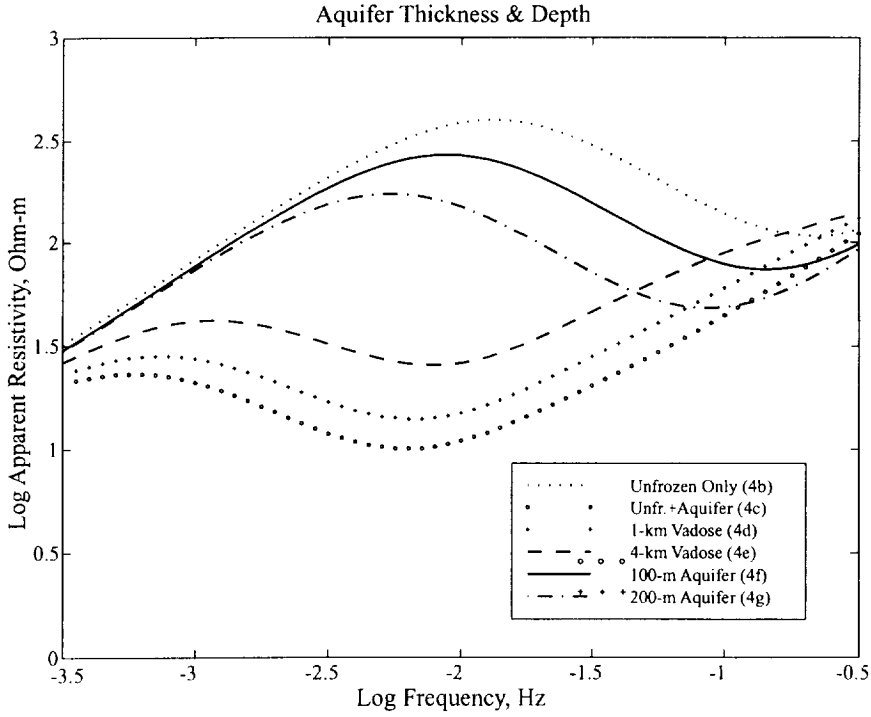

Figure 7. Resolution of subcryospheric vadose zone and imposed aquifer thickness for deep, briny aquifer (models 4d–4g) compared to unbounded subcryospheric aquifer (model 4c) and unfrozen cryospheric water only (model 4b). Poor conductivity in vadose zone requires relatively large thickness for discrimination. In contrast, high conductivity of aquifer makes response very sensitive to aquifer thickness, although interpretation is subject to equivalence in conductivity-thickness product.

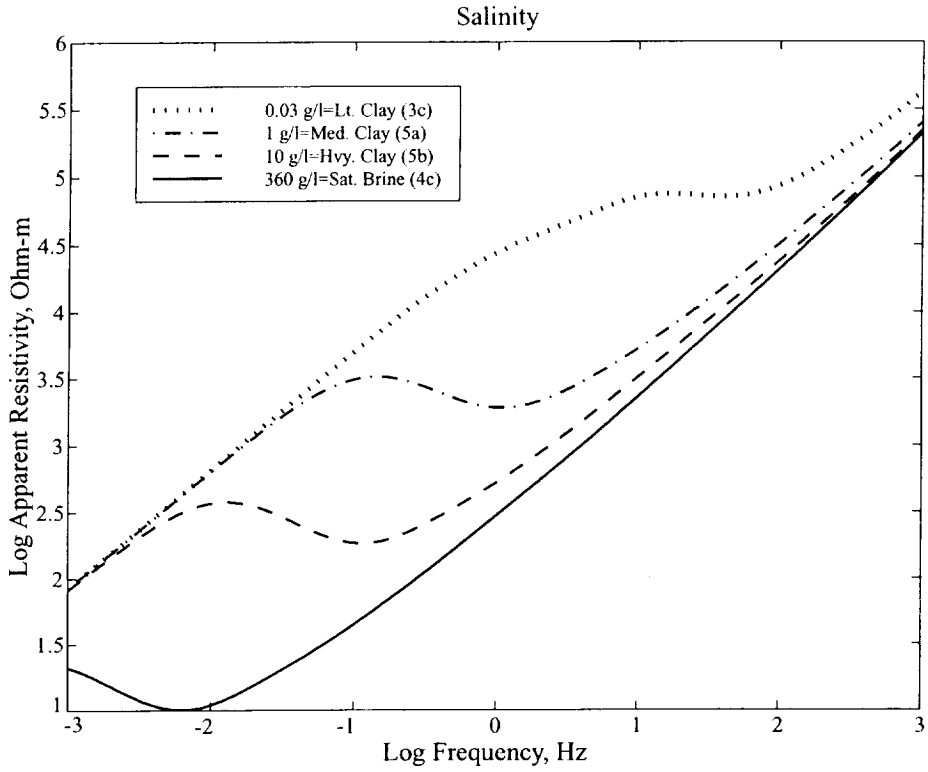

Figure 8. Response of deep aquifers including unfrozen cryospheric water over a range of groundwater salinity. Groundwater with even modest dissolved solids is detectable to subhertz frequencies (models 5a–5b).

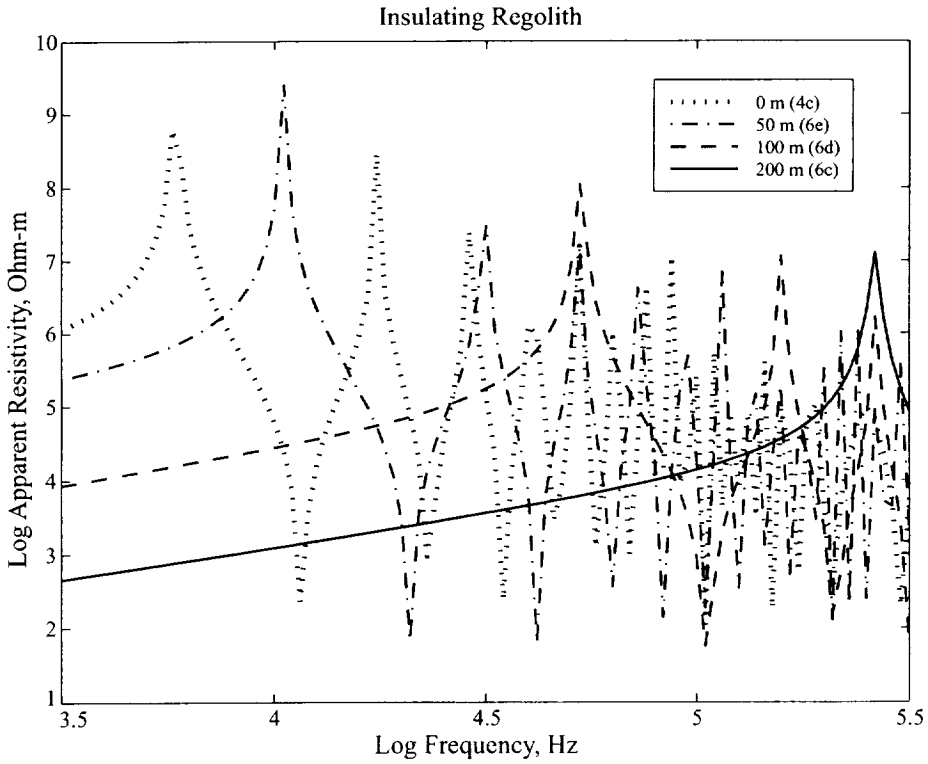

Figure 9. Effect of low thermal conductivity regolith on briny groundwater (models 6c–6e). Deep geotherm of 15 K/km sharply increases in regolith, raising ice-melting isotherm and thinning electrically resistive overburden. Propagative reflections are displaced to higher frequencies and replaced by the diffusive signature of a discrete conductor (apparent resistivity proportional to frequency).

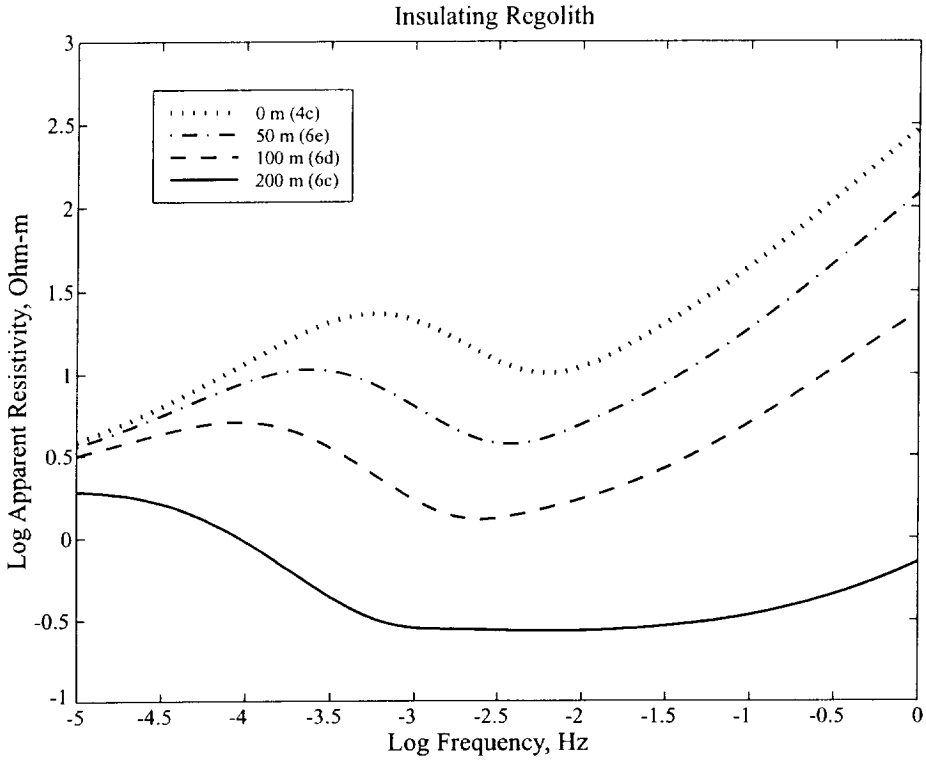

Figure 10. Extension of Figure 9 to low frequency. With increasing regolith thickness, overall resistivity is decreased and *S* line trend reversals are displaced to lower frequencies.

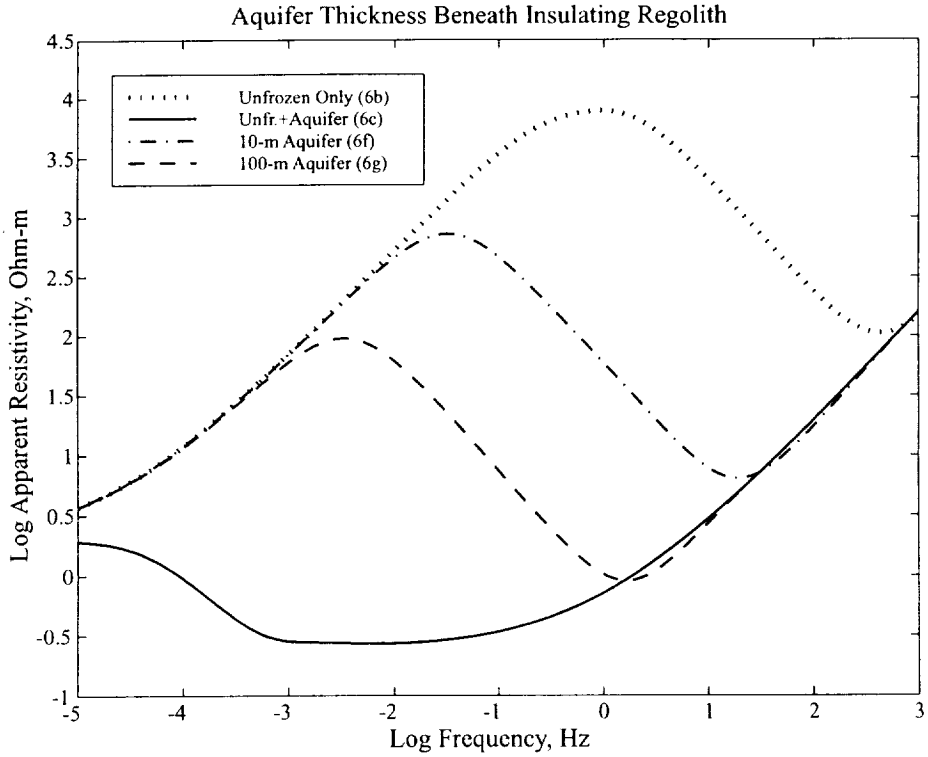

Figure 11. Resolution of aquifer thickness for shallow, briny aquifers under insulating regolith. (models 6f–g), compared to unbounded subcryospheric aquifer (model 6c) and unfrozen cryospheric water only (model 6b). Response shows very high sensitivity to aquifer thickness, again subject to conductivity-thickness equivalence.

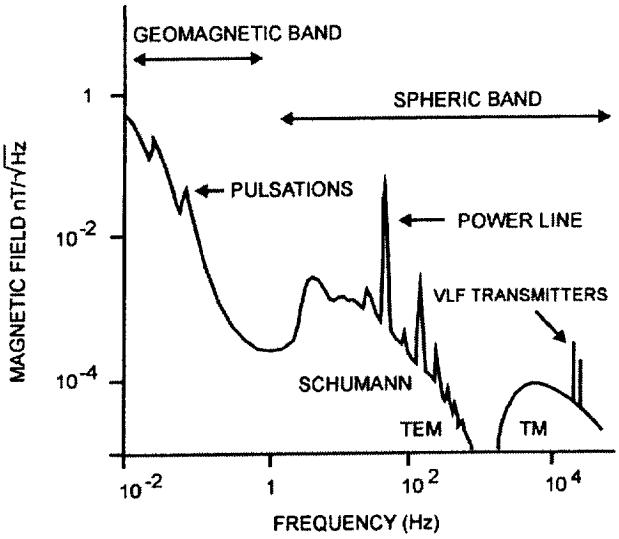

Figure 12. Stylized terrestrial low-frequency EM spectrum [after *Palacky and West*, 1991]. Natural signals in geomagnetic band are from the ionosphere and pulsations of the magnetosphere; useful signals actually extend to well below 1 mHz. Natural signals in the spheric band are from lightning and propagate as global spherical harmonics (Schumann resonances) or TEM/TM waves. The gap in energy at ~2 kHz is the mode cutoff for TM waves, whereas minimum at ~1 Hz is due to the mode cutoff for global resonances and is also the diffusion frequency shielding geomagnetic signals. For Mars, expect low-frequency energy from ionosphere and crustal magnetospheres, shift of diffusive cutoff to 50–100 Hz, weak Schumann resonances, waveguide cutoff at 1–2 kHz, and TEM/TM waves >100 Hz depending on presence of lightning and waveguide.

diffuse to the Earth's surface through the ionosphere. The principal sources of natural energy here are the highly periodic magnetohydrodynamic (MHD) pulsations of the magnetosphere, magnetospheric substorms, and the longer-period background variations due to diurnal heating of the ionosphere. These signals collectively define the geomagnetic band.

6.1. Spherics

[74] Lightning from distant thunderstorms was first exploited in EM exploration as the audiofrequency-magnetic (AFMAG) technique [*Ward*, 1959]. The audiomagnetotelluric method (AMT) added electric field measurements. VLF transmitters for military communications to submarines later became the choice for reliable signals (see *McNeill and Labson* [1991] for a review), and lightning was generally relegated to noise. *Farrell et al.* [1999] reviewed the possibility for electrical discharge from dust devils on Mars up to 10 km in diameter. Both laboratory experiments [*Eden and Vonnegut*, 1973] and the Sojourner rover [*Ferguson et al.*, 1999] have shown that significant static charge can accumulate on Mars, but to date there have been no reports of optical, thermal, or radio signatures of lightning. *Farrell et al.* [1999] estimated the radiated electric field from dust devils of various sizes by assuming (1) the DC electric field within the devil was at atmospheric breakdown values of 200–30,000 V/m, (2) the AC discharge was 10–50% of the DC discharge, and (3) the characteristic frequency of radiation is 3–4 kHz. Note that the upper limit to E field breakdown on Mars corresponds to the modal value for discharge in terrestrial thunderstorms [*Winn et al.*, 1974]. The E fields predicted by *Farrell et al.* [1999] at 200-km distance were 1 mV/m to 10 V/m. These are relatively large and easily measured fields. There are several reasons, however, why these field strengths may be overestimated. First, the effective electric size of the devil may be limited by the development of an oppositely charged sheath or corona, as pointed out by *Farrell et al.* [1999]. Charge may be equalized by high-frequency (~MHz) glow and not by filamentary discharge. *Farrell et al.* [1999] implied that the corona could limit charge accumulation to ~1% of the discharge limit, but by repeating their calculations, it is evident that this factor was not cumulatively applied to the 200- to 30,000-V/m range for breakdown fields. Thus a range of breakdown fields 2–30,000 V/m should be considered. Second, the entire devil is assumed to discharge at once. Although lower discharge volumes could be specified, *Farrell et al.* [1999] did not address the charge state of large dust storms, so either higher or lower volumes are possible. Third, the bandwidth of radiated energy was assumed to be just 1 Hz. This can be straightforwardly corrected by assuming that energy is distributed roughly over a bandwidth equal to the frequency of peak energy (~5–15 kHz [*Uman*, 1969; *Palacky and West*, 1991]). Fourth, the effectiveness of the low-conductivity Martian surface to act as a waveguide may have been overestimated. At distances of hundreds to thousands of kilometers from lightning (distances that may have to be accepted as the only sources available during measurements), estimates of the radiated electric field can vary from undetectable to easily measured. Robust quantitative assessment of time-varying electric fields on Mars simply must await in situ measurement.

[75] Some general properties of the waveguide and any putative spheric signals can be predicted, however. The waveguide thickness determines the lowest frequency that can be trapped as a TE or TM wave: $f_c = c/2h_i$, where c is the speed of in vacuum. With h_i = 70 km at VLF [*McNeill and Labson*, 1991], f_c = 2 kHz for Earth, in agreement with the observation of a narrow but pronounced energy deficiency in the terrestrial spectrum at this frequency (Figure 12). Below the cutoff frequency, energy is trapped as plane transverse electromagnetic (TEM) waves or as spherical-harmonic oscillations, the Schumann resonances. High-order TEM waves form a continuum, but the low-order TEM waves and Schumann resonances are discrete modes. The transition between plane and spherical geometry occurs at ~100 Hz, where the free-space wavelength is a significant fraction of the planetary radius.

[76] The 70-km effective height of the terrestrial ionosphere at VLF frequencies corresponds to the lowermost strong vertical gradient in charge density that defines the D region. Here electron densities increase from $\sim 10^2$ to $\sim 10^3$ cm^{-3} over the altitude interval ~60–90 km [e.g., *Russell*, 1995]. By 100-km altitude the electron density in the ionosphere of Mars is $\sim 10^3$ cm^{-3} [*Hanson et al.*, 1977]. Therefore the conductivity magnitude and gradient appear to be sufficient to reflect low-frequency EM waves, and the 70-km altitude for the top of the VLF waveguide will be retained as a first approximation.

[77] Although the top of a low-frequency waveguide can thus be roughly established for Mars, the low-conductivity upper Martian crust will be much less efficient as a waveguide than the near surface of the Earth. Using the models developed above, an anhydrous Martian lithosphere does not even attain conductivities characteristic of Earth's shield and permafrost regions ($\sim 10^{-4}$ S/m) until depths of 40–60 km at a geotherm of 15 K/km. *Cummer and Farrell* [1999] analyzed the propagation of spherics on Mars using a detailed model of the ionosphere and found that frequencies in the range 2–5 kHz were strongly attenuated. However, they noted that the uniform, relatively high ground conductivity of 10^{-7} S/m (see Figure 2) in their models formed the bottom of the waveguide by choice and that lower near-surface conductivities could cause this boundary to lie at greater depth.

[78] A completely anhydrous crust therefore would be characterized by high propagation loss, and the hydrous case would be characterized by low propagation loss. These hypotheses could also be tested simply by measuring the frequency of the waveguide cutoff from a single surface station: the frequency should be ~2 kHz if upper crustal conductors are present but would lie lower, perhaps closer to 1 kHz, if the crust of Mars is anhydrous and poorly mineralized. The last constraint recalls that interconnected iron minerals are another potential source of crustal conductivity that must be discriminated from water. The presence of ice does not affect the waveguide.

[79] The first several Schumann resonances for Earth are at 8, 15, 20, 26, and 32 Hz. As the resonance frequencies vary inversely with the radius of the ionosphere [e.g., *Rawer*, 1993], Schumann resonances on Mars might be expected to lie approximately at 15, 28, 37, 48, and 60 Hz. Calculations using a detailed model of the ionosphere [*Sukhorukov*, 1991] predict resonance frequencies on Mars of 13–14, 24–26, and 35–38 Hz. However, these frequencies lie below the expected diffusion frequency of the Martian ionosphere (see below), which may imply that the resonances are very lossy; indeed, *Sukhorukov* [1991] calculated quality factors of just 2–4.

6.2. Geomagnetics

[80] At the lowest frequencies the ionosphere cannot trap EM waves, and energy diffuses both outward and down to the Earth's surface. The minimum period that can diffuse through a medium of conductivity s and thickness h is given roughly by the diffusion time, $t_D \sim s\mu h^2$. For a daytime total conductance of the ionosphere of ~10 S [*Wolf*, 1995] over a thickness of ~100 km that contributes most of this conductance, $t_D \sim \mu Sh = 1$ s, corresponding to a frequency of ~1 Hz. A broad energy minimum occurs near 1 Hz in the terrestrial spectrum (Figure 12), consistent with the diffusive rather than wave nature of this division. The peak ion density for Mars is an order of magnitude smaller than Earth [*Luhmann*, 1992], and the corresponding thickness is perhaps a third of Earth's, so the diffusion time may be expected roughly to be two orders of magnitude smaller, i.e., a maximum diffusion frequency of 50–100 Hz.

[81] The frequency (2 mHz to 5 Hz) and intensity (red spectrum) of terrestrial MHD oscillations of the magnetosphere make them ideal for deep sounding. Without a global magnetosphere, no such signals will exist for Mars. However, the large fields of the crustal anomalies are known to exclude the ionosphere [*Acuña et al.*, 1999]; because these magnetic fields reach so high, they are also subject to time-varying ionospheric and solar wind perturbations and therefore might produce useful EM signals. These field lines do not satisfy the assumptions used to calculate the modal frequencies of terrestrial MHD standing waves [*Kivelson*, 1995], so no attempt will be made to predict their qualities at Mars, other than that they should be observable during the day, when the driving forces are greatest.

[82] Magnetic substorms and storms are another common source of ULF energy on Earth, particularly from the auroral and equatorial electrojects. Again, as these phenomena are intimately linked to the large terrestrial magnetosphere, they are not expected at Mars, unless the "mini-magnetospheres" have some relevant properties of the global magnetosphere.

[83] The lowest-frequency signals commonly used for terrestrial EM exploration are due to diurnal variations of the ionosphere, called S_q. Giant countercirculating currents in the low-latitude ionosphere produce signals with periods of a day and its higher harmonics of 12, 8, 6, and 4 hours (see *Campbell* [1997] for a review). The form of these currents is consistent with a dynamo interaction of the motion of ionospheric electric charge across the Earths magnetic field lines. Localized dynamo interactions of the ionosphere and remanant crustal magnetic fields could occur on Mars. In addition, there may be a component of the current that is directly driven by solar heating of the ionosphere, and on Mars the solar wind directly impacting the ionosphere will produce additional time-varying signals, probably with amplitudes of ~20–30 nT [*Luhmann et al.*, 1987]. The base frequency and harmonics of any such diurnal events are trivial to predict, but the identification of signals resulting from interaction with crustal magnetism will likely require in situ observation. The transition to lower plasma density at night will yield higher temporal harmonics owing to the associated spatial discontinuity. Indeed, if the transition is sufficiently sharp, the transition may approximate a step function, and broadband natural-source time-domain sounding may be possible.

[84] In summary, the most likely time-varying EM fields observable near the surface of Mars are those due to diurnal heating and solar wind perturbation of the ionosphere. Where directly driven by solar heating or the solar wind, these ultra-low-frequency (~10^{-5}–1 Hz) fields will be maximized during the day and at low latitudes. The daily variations of plasma density in the ionosphere and perturbation of the fields from crustal magnetic anomalies may also yield signals that are more regionally restricted. Energy from any lightning on Mars will be strongly trapped only at frequencies greater than 50–100 Hz, although weak Schumann resonances may be present at lower frequencies. Both plane TEM (100 Hz to 1 kHz) and TM (>1 kHz) waves can be waveguided to great distances, up to a hemisphere or more, depending on ionospheric continuity.

7. Natural-Source Measurements

[85] EM signals are measured by the magnetic field, the electric field, or both. Specific instruments for making these measurements are discussed later. In the propagative regime the electric and magnetic fields have equal energy; which is measured is a matter of convenience. At higher conductivity, opposing secondary fields are inductively generated, partly canceling the primary field, and the electric field is attenuated preferentially. The ratio of electric to magnetic fields is essentially a measurement of voltage drop divided by current, i.e., a resistance or, more formally, an impedance:

$$Z = \left|\frac{E_x}{H_y}\right|^2 = \left|\frac{E_y}{H_x}\right|^2. \tag{22}$$

This is the magnetotelluric (MT) method (see *Vozoff* [1991] for a review). Explicit horizontal components are shown in (22) because the electric and magnetic fields are measured orthogonally. The two cross measurements are equal only for a layered medium; indeed, differences are exploited in tensor analyses for laterally heterogeneous media.

[86] The fundamental MT assumption is that subsurface primary fields can be treated as vertically moving plane waves. Strong wave front curvature occurs when measurements are made near the source. Incident fields approximate plane waves at distances much greater than the skin depth away from a compact source; typically, a distance of 3 skin depths suffices in practice [e.g., *Zonge and Hughes*, 1991]. An upper bound to the skin depth for the models presented above will be given by the anhydrous crust at 15 K/km (model 1). The lower bound on skin depth for the models presented here is a briny (360 g/L) groundwater including unfrozen water in the cryosphere, an unbounded subcryospheric aquifer, and a 200-m insulating regolith (model 6c). For lightning with frequency peaks at 150 and 2500 Hz, a three-skin depth offset on Mars can be achieved for the anhydrous crust at a distance of 130 and 15 km, respectively. For the shallow-brine model the required offsets are close to 600 m for both cases. Therefore some care must be taken in interpreting the results from lightning sources if they are suspected to

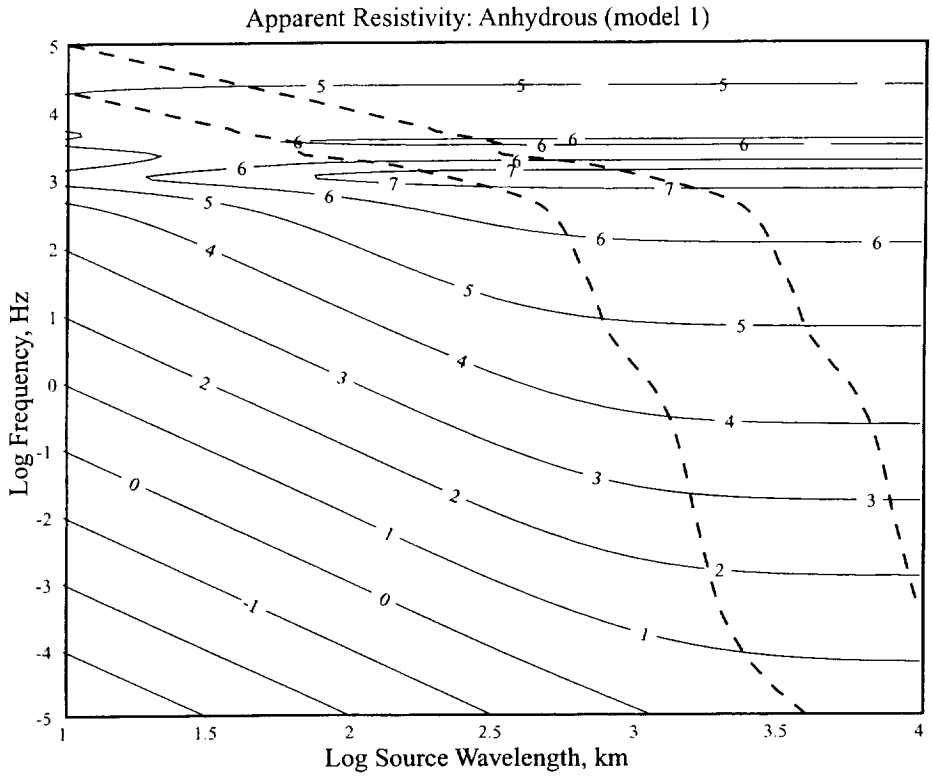

Figure 13. Effect of source-field structure on magnetotelluric (MT) and geomagnetic depth sounding (GDS) measurements for anhydrous model, following *Madden and Nelson* [1985]. Solid contours are log apparent resistivity. At sufficiently high frequency, measurements are independent of source wavelength and would plot as Figure 3. At low frequency the source wavelength dominates (parallel contours with slope −2), and there is no information on subsurface structure. Lower dashed line is low-frequency cutoff for MT; portion of the figure below has error >20% [*Madden and Nelson*, 1985]. Upper dashed line is high-frequency cutoff for GDS; portion of the figure above has vertical field <0.1 of horizontal. An anhydrous crust is relatively unfavorable for MT and relatively favorable for GDS in terms of the span of frequencies that may be applied when the source wavelength is unknown.

lie within ~100 km, but clearly the plane-wave assumption will be satisfied even under conditions that endanger the instruments.

[87] As described above, the large material contrast at the planetary surface usually assures that waves are refracted strongly downward. While this simplifies computations within the subsurface, continuity of tangential E and H implies that measurements can still be biased by the presence of horizontal wavelengths. Intuitively, vertical incidence will be satisfied when the horizontal source wavelength is much greater than the vertical diffusion wavelength $2\pi\delta$. The effect of finite horizontal wavelength can be incorporated simply by rewriting (4) in terms of wave number rather than impedance,

$$\rho_a = \omega\mu/k^2, \tag{23}$$

and relaxing the assumption that the vertical component dominates, so that now $k^2 = k_h^2 + k_z^2$, where k_h and k_z are the horizontal and vertical wave numbers, respectively. *Madden and Nelson* [1985] calculated the apparent resistivity this way as a function of both frequency and source wavelength for alternative whole-Earth conductivity structures. They assigned a cutoff frequency to each wavelength where the apparent resistivity differed from its value under an infinite horizontal wavelength by 20%; frequencies above this cutoff may be used in MT soundings. *Madden and Nelson* [1985] considered a worst case geometry of a line source in the ionosphere, corresponding to the equatorial or auroral electrojets. A line source has an exponential spectrum with a $1/e$ cutoff wavelength of $2\pi d$, where d is the source height. Taking d = 150 km, the cutoff wavelength is ~900 km. *Madden and Nelson* [1985] found that the corresponding cutoff frequency for their Earth-conductivity models was ~0.01 Hz. Away from line sources, where wavelengths might approach 10^4 km or greater, the cutoff is $<10^{-5}$ Hz.

[88] The same approach was applied to the end-member Mars-conductivity models 1 and 6c (Figures 13 and 14, respectively). Assuming that ionospheric source heights are roughly comparable, a 1000-km source wavelength results in a 20% error in apparent resistivity at a frequency of ~1 Hz for the anhydrous model. The drier conditions of Mars result in smaller vertical wave numbers, which introduces more error for the same horizontal wavelength. The error is negligible for frequencies $>10^{-5}$ Hz if the source wavelength is 3000 km. For the shallow-brine conditions the very large vertical wave numbers allow the plane-wave assumption to be satisfied under almost all practical conditions: $>3 \times 10^{-5}$ Hz at 1000-km wavelength.

[89] As mentioned above, the strong crustal magnetic anomalies of Mars may themselves be significant EM sources. The concentrated anomalies in Terra Cimmeria [*Acuña et al.*, 1999] appear to have characteristic wavelengths of order several hundred kilo-

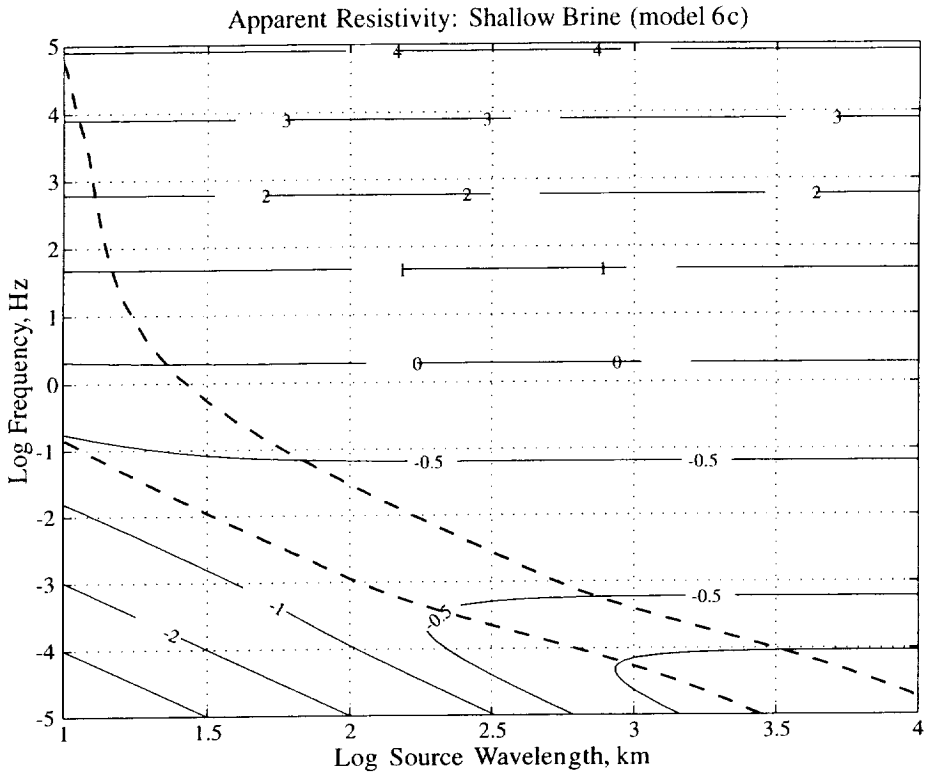

Figure 14. Effect of source-field structure on MT and GDS measurements for shallow-brine model. Contours are log apparent resistivity. Low-frequency cutoff for MT (lower dashed curve) is now more favorable, and high-frequency cutoff for GDS (upper dashed curve) is less favorable than for anhydrous case.

meters. Using the same models and criteria at 300-km wavelength, the low-frequency cutoff could be as low as 2×10^{-4} Hz for the shallow-brine model but as high as 5 kHz for the anhydrous model. As these sources will likely also be ULF, radiation will not be trapped in the ionospheric waveguide and therefore will be sensed only locally. Strong caution is called for in interpreting these signals.

[90] Two other kinds of natural- or distant-source measurements operate similarly to the magnetotelluric method. In geomagnetic depth sounding (GDS), finite spatial wavelengths of the source field are exploited so that the apparent resistivity can be computed from the vertical B_z and horizontal B_h components of the magnetic field as

$$\rho_a = \omega\mu(B_z/kB_h)^2, \tag{24}$$

where B_z and B_h are the vertical and net horizontal components of the magnetic field, respectively [*Gough and Ingham*, 1983], and k is again the total wave number. In contrast to MT, GDS is not a single-station method; it requires a 2-D spatial array to determine k_h in order to produce a 1-D sounding. However, GDS needs only three-component magnetic field measurements without regard to the electric field. Whereas MT has a low-frequency cutoff to eliminate source-structure effects, GDS has a high-frequency cutoff so that these structures can be measured. In the absence of lateral heterogeneity (i.e., assuming a 1-D sounding), a vertical component of the magnetic field will exist only if there is a finite source wavelength. Assume that $B_z > 0.1$ B_h for a reliable measurement. In practice, B_z of several tens of percent B_h is common [see *Gough and Ingham*, 1983]. This criterion corresponds to an equivalent error in ρ_a of just 1%, so in comparison to the MT criteria, the cutoff frequencies will be at conservatively higher values. For the Earth-conductivity model used by *Madden and Nelson* [1985], the GDS criteria developed here would restrict measurements to <1 Hz at 300-km wavelength. Such constraints generally pose no obstacles to even short-period terrestrial GDS studies. For Mars the anhydrous model is the most favorable for GDS: all frequencies <3 kHz will have sufficient field structure for a source wavelength of 300 km. Under the shallow-brine model, measurements would be restricted to <3 mHz at the same wavelength. The range of possible subsurface conditions on Mars carries a six order-of-magnitude uncertainty in the useable frequency range of GDS.

[91] A more serious constraint on GDS is the need for a dense 2-D network to decompose spatial variations into a wave number spectrum. Because the method assumes a 1-D structure, arrays are made as compact as possible, with station separations of ~10 km and the entire array perhaps ~100 km across. Such constraints will strongly affect the utility of GDS on Mars.

[92] The third approach to EM sounding using natural or remote sources is to measure the electric field wave tilt E_h/E_z. For a TM (vertically polarized) wave with grazing incidence, appropriate to distant lightning or a transmitter, the impedance is just [*McNeill and Labson*, 1991]

$$Z = \eta_0|E_h/E_z|, \tag{25}$$

where $\eta_0 = 377\ \Omega$ is the impedance of free space. The wave acquires a horizontal component to the E field because it is refracted nearly vertically into the ground, essentially converting to horizontal polarization there. This results in a small forward tilt,

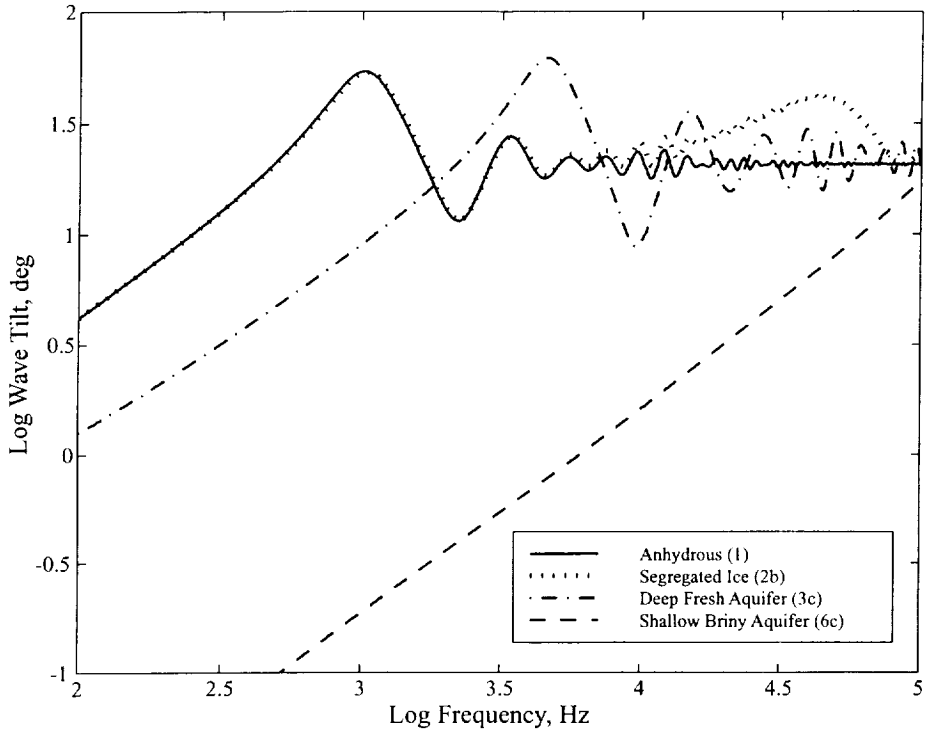

Figure 15. Sounding by electric field wave tilt for representative models. This set of calculations is for TM waves, appropriate to most cloud-to-ground lightning strikes. Downward refraction into the ground of the near horizontally propagating wave causes a forward tilt to the net field. Asymptotic value of 21 degrees for several models is the dielectric limit for the assumed relative permittivity of 7.

which, if measured as a function of frequency, can be used to perform soundings. Wave tilts for representative models with a vertically polarized source presented above are shown in Figure 15: small wave tilts are observed for conducting interiors. The tilt of TE (horizontally polarized) waves can also be measured; here the boundary conditions produce larger tilts for conducting interiors [*Singh and Lal*, 1981]. Wave tilt is an attractive measurement because soundings can be performed from a single station, like MT. However, greater knowledge of source structure is required (TM or TE wave), and a robust measurement using the E field alone is more difficult than when using the E and B fields or the B field alone.

[93] Finally, it is possible in principle to perform single-station soundings using the magnetic field only. Using the same assumption as MT that horizontal gradients are small, Amperes law can be used to show that the impedance can be formed from a quantity that includes the vertical derivative of the horizontal magnetic field. Such measurements have been attempted using SQUID magnetometers (N. Harthill, personal communication, 1997) but were only marginally successful owing to the very small gradients to be measured.

8. Artificial-Source Methods

8.1. Slingram and CSAMT

[94] Active EM methods operate in either the frequency or time domain. In frequency-domain EM (FDEM), a continuous-wave (CW) source field is emitted from a grounded wire or ungrounded loop. Contact impedances are very high for the high resistivity at the surface of Mars, so loop sources must be used (this also eliminates familiar "DC" electrical methods). The most widely used FDEM technique is the moving loop-loop, or Slingram method [e.g., *McNeill*, 1990]. The transmitting and receiving coils are maintained at a fixed separation and orientation. The primary field dominates the signal at the receiver, but the small secondary field from the ground can be measured as a small phase shift with respect to the primary field, or it can be measured directly if a second source coil is geometrically positioned to "buck out" the primary field at the receiver. Slingram methods require careful control of coil position and orientation so the small secondary fields can be accurately extracted.

[95] When the receiver is in the near field of the transmitter (generally within a distance of about one skin depth), the depth of exploration is a function of conductivity and distance from the source but not of frequency [e.g., *Zonge and Hughes*, 1991]. In this regime, geometric soundings are performed by changing the spacing of the transmitter and receiver. Slingram systems generally operate in the geometric sounding domain. "DC" electrical methods are also geometric soundings. In contrast, the transmitted source can be approximated as a plane wave in the far field, and parametric soundings (those utilizing the skin depth for differential penetration as a function of frequency) can be performed. In parametric sounding, subsurface resistivity structure can be inverted as a function of frequency, typically with the geometric factors eliminated through some kind of ratio. Geometric soundings require relatively large transmitter-receiver separations or array lengths, typically several times the depth to the target, with commensurately poor lateral resolution. For this reason alone, parametric methods are generally preferred for deep soundings and may be especially relevant to resource-limited subsurface exploration of Mars.

[96] Parametric soundings could be made on Mars with a simple FDEM loop-loop system. The distance necessary to attain the far zone is considered to be a few (typically three) skin depths [*Zonge and Hughes*, 1991]. As described above, however, the uppermost crust of Mars may be very resistive, and therefore conductive

materials may be distant from the sensors. Airborne surveys will add additional free space in between the instruments and the target. The mutual coupling of two horizontal loops at an arbitrary distance above a conductive half-space [*Wait*, 1955, 1956] may be used to investigate the transmitter-receiver separation required to attain the far field under these conditions. When the distance above the conductive half-space is small compared to the skin depth, the latter closely approximates the transition distance (or a sizeable fraction thereof). When the distance is large compared to the skin depth, the former approximates the transition distance. For a distance above a conductor of 300 m, representative of surface instruments on Mars and a shallow aquifer, offsets of hundreds of meters to kilometers are required to attain the far field. Slingram soundings will not be very sensitive to water at 300 m if the geometrical regime is met for separations only within 100 m or so, and parametric soundings have a large "dead zone" around the transmitter.

[97] Artificial-source, frequency-domain, parametric soundings are commonly performed as controlled-source audiomagnetotelluric (CSAMT) surveys that measure the horizontal components of both E and H. The E/H ratio eliminates the source-receiver distance as a variable in the inductive far field, and the exploration depth is a function of frequency and conductivity. However, CSAMT faces the same constraint as parametric loop-loop FDEM: soundings cannot be performed until the transmitter and receiver have achieved some relatively large separation. If a compact system is desired (see below), useful signals will be limited to a few hundred meters' distance at VLF. When the frequency is increased to, say, 1 MHz (MF), adequate signal can be obtained with a compact FDEM system, but the response is now propagative instead of inductive. Indeed, interferometric measurements of standing waves between the transmitter, receiver, and reflective targets were the basis of the Apollo Surface Electrical Properties (SEP) experiment. Modern ground-penetrating radars will provide better measurements of dielectric properties.

8.2. Time-Domain Electromagnetics

[98] Time-domain electromagnetic (TDEM) methods measure the transient response of the Earth to a step- or pulse-like transmitted waveform; the method is also called pulsed-induction. A static magnetic field is established in the Earth while the transmitter current is on. When this field is changed (usually by abrupt extinction), the EMF generated according to Faraday's law causes eddy or secondary currents to flow in the ground. At the instant of transmitter turnoff, eddy currents reproduce the static magnetic field but then decay rapidly. These changing currents induce new currents in the ground at greater depth; the net effect in a homogeneous half-space is diffusion of an equivalent current filament into the ground at an angle of 47°, which has led to visualization of the system as a diffusing smoke ring [*Nabighian*, 1979]. The diffusion depth $d = \sqrt{2t/\sigma\mu}$ is entirely analogous to the skin depth in the frequency domain, and therefore TDEM can be used to perform parametric soundings. Because TDEM measurements are made at a sequence of times following transmitter turnoff, these systems can behave as wideband receivers. The transition from near to far field can be accomplished simply by measuring the response at later times, rather than requiring transmitter-receiver separation. In other words, the early-time (near-field) depth of investigation is geometric, whereas the late-time (far-field) depth of investigation is parametric.

[99] The wideband characteristic of TDEM has been a key advantage in sounding through near-surface conductive layers on Earth, again wherein measuring the response at later times is equivalent to using a lower frequency and hence achieving a greater depth of penetration. TDEM has higher sensitivity to the geoelectric section than FDEM (proportional to $\sigma^{3/2}$ rather than s [*Spies and Frischknecht*, 1991]). Because measurements are made during transmitter off time, results are remarkably insensitive to geometrical detail; for example, loops can be somewhat irregular in shape and draped on terrain without adversely affecting interpretation. Measurements can be made using the same loop as transmitter and receiver (coincident-loop) or with a separate receiver. The latter is often placed in the middle of the transmitter and is therefore called central-loop. When the target is deep compared to the coil size, the results are insensitive to the relative positions of the coils. Disadvantages of TDEM include higher peak power necessary to generate strong transmitted pulses and susceptibility of wideband systems to ambient noise.

8.2.1. Russian TDEM. [100] The conclusion that TDEM would be useful on Mars was reached independently by the Russians in the late 1980s (of course, critical information that shallow water might actually exist was not then known). A TDEM system was developed for the Mars 94 mission (E. Fainberg, personal communication, 2000), which was ultimately canceled. A 20- to 30-m single-turn loop was to have been laid out by a rover, which was also to have carried and powered the TDEM system. Derivatives of this system have been subsequently commercially marketed as the TEM-FAST (AEMR, Holland). Below, the response of a Mars 94 system is computed using published TEM-FAST parameters. Layout of the loop by the rover would have placed strong demands on earlier rover capability. There were other potential shortcomings to the Mars 94 (TEM-FAST) system, including the coincident-loop design (which is susceptible to extraneous responses from magnetically polarizable soils), the response of early time gates (self-inductance?), and the actual noise floor [*Blackhawk Geoservices Inc.*, 1999]. Nonetheless, the spaceflight inheritance of the TEM-FAST has perhaps made it the smallest commercially available TDEM system, with dimensions of 29 × 27 × 6 cm and a weight of 2 kg, not including the loop; the flight prototype apparently was smaller and lighter (E. Fainberg, personal communication, 2000). The present system does require an external PC and battery.

8.2.2. Strawman designs. [101] Artificial-source soundings would be most appropriate on Mars in the event that natural sources are weak or absent, so some rough TDEM considerations are presented here to complement the natural-source investigations described above. The key parameter describing receiver performance is the noise level, which could be dominated by self-noise or by the environment. The latter can include the platform (lander, rover, airplane, balloon) and natural sources. Three possibilities are quantitatively considered: (1) a best case in which the internal system noise of the combined transmitter and receiver is the limiting factor, (2) an intermediate case in which noise levels are characteristic of terrestrial measurements in the presence of "culture," and (3) a worst case in which the platform has radiated magnetic emissions up to the maximum allowed for military electromagnetic interference. Separate consideration is given below to coherent "noise" introduced by energizing eddy currents in the platform itself. For the low-noise end-member, consider the BF-6 magnetic antenna manufactured by Electromagnetic Instruments, Inc. (EMI), and assume the measurements are fed to an EMI MT-1 receiver. As described below, there are certain advantages to direct measurement of B using a magnetic antenna rather than recording dB/dt using a simple induction coil. The combined coil and receiver have a noise floor $B_0 < 10^{-5}$ nT/$\sqrt{\text{Hz}}$. It is not unusual for the noise level to approach the instrument floor away from cultural interference on days with minimal spherics. For the intermediate case a noise floor of 10^{-3} nT/$\sqrt{\text{Hz}}$ is adopted, which is equivalent to terrestrial noise levels of 10^{-3} nT [*Spies and Frischknecht*, 1991] for a typical TDEM receiver noise bandwidth of ~1 Hz. For the high-noise end-member, MSFC-SPEC-521B (RE04 Magnetic Field Radiated Emissions, 30 Hz to 50 kHz) permits 3000 nT at frequencies <1 kHz at a distance of 1 m.

[102] Now the effective noise bandwidth ν of a TDEM system is approximately $1/4\tau$, where t is the RC time constant for an analog gate integrator or the product of gate width and a recursion-filter

constant for digital processing [*Becker and Cheng*, 1988]. The product of the number of samples N and the receiver-gate width Δ must greatly exceed τ; a value of $\tau = N\Delta/5$ is consistent with the settling time of the digital recursion filter [see *Becker and Cheng*, 1988]. Because the integration time $t_0 = N/f_T$, where f_T is the transmitter pulse frequency, the time constant can be expressed as $\tau = f_T t0\Delta/5$, so the noise bandwidth is

$$v = 5/4t_0 f_T \Delta. \tag{26}$$

Further simplification can be achieved by specifying the ratio of gate-to-pulse width, $f_T\Delta$. Commercial TDEM systems typically have $f_T\Delta \sim 0.01$ [e.g., *Becker and Cheng*, 1988]. Small $f_T\Delta$ will best resolve the subsurface response with a single transmitter pulse rate (as the gate spacing is relatively smaller) but sacrifices narrower bandwidth for operational simplicity. This is partly alleviated by logarithmically increasing the gate spacing and width with time. Most TDEM systems also allow a few different transmitter frequencies to further expand the measurement range; results from different transmitter frequencies can be combined if the response spans more than one setting. A transmitter system that could sweep a greater number of base frequencies could have larger $f_T\Delta$ and hence a narrower noise bandwidth, especially if the desired response was contained in, say, a single decade of frequency rather than two or more. Only a factor of ~ 3 ($f_T\Delta = 0.1$) on either side of the early-to-late time transition may be necessary to determine aquifer depth and conductance, but conservatively a full decade each way ($f_T\Delta = 0.01$) will be used. By choosing a pulse rate that places the transition logarithmically midway in the receiver interval, it is assumed that an optimum transmitted frequency can be sought at a resolution of several frequencies per decade.

[103] If the transmitter could be made more compact, say, a foldable or detachable coil no more than a few meters in diameter, the entire system could be more easily deployed or even be incorporated into mobile platforms. For the present strawman, consider the Geonics EM61. This compact TDEM system was originally designed for detecting drums and other debris on hazardous waste sites to a depth of a few meters and has since seen wide application in the detection of unexploded explosive ordnance (UXO). Derivatives of this instrument measure multiple time gates and spatial components necessary for in situ discrimination of UXO from scrap [e.g., *Grimm et al.*, 1997]. The standard EM61 uses a 1-m-diameter, square transmitter coil with 32 turns and 6 A. The coil diameter could be increased to 2.5 m and the current decreased to 1 A and maintain the same moment, if current and power are more limited than size.

8.2.3. Model. [104] The frequency-domain solution for the secondary magnetic field from a horizontal loop on a layered half-space [e.g., *Ward and Hohmann*, 1988] may be inverse-Fourier transformed to derive TDEM results similar to those shown above for vertically incident plane waves. This solution actually builds directly upon the plane-wave results as it uses the zero-order Hankel transform of the oblique-incidence reflection coefficient, which, in turn, follows directly from the plane-wave impedance. Such work will be deferred and instead only a demonstrative example will be presented for the simple approximation when the subsurface target can be approximated as an infinite, thin, horizontal plate in free space with conductivity σ and thickness h. In this scenario the response depends only on the conductance $S = \sigma h$ of the target. The vertical magnetic induction for a vertical-dipole (horizontal-loop) transmitter with coincident receiver above the conductive plate is simply [*Kaufman*, 1994]

$$B_z = -\frac{\mu M_T}{2\pi(bt + 2d)^3}, \tag{27}$$

where M_T is the transmitter moment (current × turns × area), $b = 2/\mu S$, t is the time after transmitter turnoff, and d is the distance of the sensor above the plate. The EMF in the receiver coil then can be derived by simple time differentiation of (27):

$$V = M_R \frac{dB_z}{dt} = \frac{3b\mu M_T M_R}{2\pi(bt + 2d)^4}, \tag{28}$$

where M_R is the receiver moment (turns × area). In early time, $bt \ll 2d$, so $B_z = \mu M_T/16\pi d^3$ and $V = 3\mu b M_T M_R/32\pi d^4$. The magnetic field (or induction) on the plate is a static image of the dipole primary and falls off as $1/d^3$, whereas the voltage drops as $1/d^4$. The early-time magnetic field is then a direct indicator of the distance to the conductive plate, independent of the plate conductance. However, the voltage also varies inversely with conductance: thicker or more conductive plates actually result in smaller signals immediately after transmitter turnoff. As the early-time responses depend on distance, they are geometric soundings. In late time, $bt \gg 2d$, so $B_z = \mu M_T/2\pi(bt)^3$ and $V = 3\mu b M_T M_R/2\pi(bt)^4$. The magnetic field decays as $1/t^3$, and the voltage decays as $1/t^4$. The response now varies with time, so this is the parametric-sounding regime. The late-time response is very sensitive to the plate conductance. Clearly, measurements distributed over early and late times (or simply the transition zone between the two) can measure both the plate's depth and conductance.

[105] The maximum depth at which the conductive plate can be detected may be derived by solving the early-time forms of (27) and (28) for d. The noise level must then be specified in units of magnetic induction or voltage, depending on the receiver system. The noise level multiplied by a specified signal-to-noise ratio (SNR) gives the actual detection level. For magnetic field measurements the dependence of the exploration depth upon all relevant parameters may be summarized as

$$d \propto a^{2/3} I^{1/3} (\mathrm{SNR} \cdot \mathrm{B_0})^{-1/3} (t_0 f_T \Delta)^{1/6}. \tag{29}$$

Transmitter diameter has the greatest influence on exploration depth yet may be the most strongly constrained for operation on Mars. Integration time may be one abundant resource compared to terrestrial exploration but has only a weak influence: a 64-fold increase in stacking time is necessary to double the depth of exploration. The transmitter current term, which includes multiturn windings, has an intermediate influence and may be able to improve sounding depth at modest cost.

[106] The layered conductivity models given above are further simplified for uniform aquifers of finite thickness. As an upper limit to the resistivity of aquifers on Mars, assume just 2% porosity and groundwater in equilibrium with very little clay in rocks (0.03 g/L total dissolved solids (TDS)). The net resistivity is $\sim 10^4$ Ω-m. As a lower limit, take 20% porosity and brine-saturated pore water, yielding a net resistivity of 0.25 Ω-m. A nominal case might be 10 Ω-m, from 10% porosity and groundwater in equilibrium with heavy clay in rocks (10 g/L TDS).

[107] The plate model can first be tested for the Mars 94 TDEM as inferred from its commercial successor, the TEM-FAST 32. SNR = 10 was chosen to be consistent with the conservative calculations below. Assuming that the noise floor is determined by the instrument itself and not the environment or the spacecraft, the Mars 94 TDEM using a 30-m coincident loop could have detected water at a depth of ~150 m for a nominal-resistivity aquifer 100-m thick. The integration time is that required to achieve 1 μV noise level. Exploration depths of 30 m to >1 km follow from the range of aquifer conductivities given above for aquifer thicknesses 10–1000 m.

[108] With the conservative design parameters and strawman compact transmitter and receiver given above, water may be detected to a depth of 480 m for an integration time of just 10

Table 3. TDEM Performance

Configuration	Noise[a]	Integration Time	Exploration Depth, m
Small, low-power	low	10 min	480
(2.5-m diameter Tx, 1 kg, 6 W)	terrestrial	10 min	100
	low	1/2 sol	980
	terrestrial	1/2 sol	210
Large, low-power	low	1/2 sol	3600
(100-m diameter Tx, 1 kg, 8 W)	terrestrial	1/2 sol	800
	low	10/2 sol	5300
	terrestrial	10/2 sol	1100
Large, high-power	low	1/2 sol	9800
(100-m diameter Tx, 25 kg, 150 W)	terrestrial	1/2 sol	2100
	low	10/2 sol	14000
	terrestrial	10/2 sol	3100

[a]Low = 1×10^{-14} T/$\sqrt{\text{Hz}}$, terrestrial = 1×10^{-12} T/$\sqrt{\text{Hz}}$. Conversion to measureable signal conservatively assumes SNR = 10, $f_T \Delta = 0.01$ (see text).

min under low ambient noise (Table 3). Continuous stacking for a half sol doubles the exploration depth (980 km). This integration time follows from operations in which power is drawn continuously from solar panels during daylight hours or, alternatively, running the system on batteries throughout the night, when most other science instruments are shut down. Under terrestrial noise conditions, the maximum depth of investigation is 100 m for a 10-min stack and 210 m for a half-sol operation. These results are very conservative; if SNR = 2 and $f_T\Delta = 0.1$, for example, the half-sol exploration depths are 2500 m and 500 m for the low- and terrestrial-noise scenarios, respectively. The transmitter loop for this compact sounder would weigh ~1 kg and consume ~6 W continuous power [see *McDermott*, 1992].

[109] The experiment would fail utterly under the specified high-noise scenario, as integration times in excess of 1 m.y. would be necessary to detect water to just 40-m depth. The system can be improved by separating the source and receiver, but the offsets become comparable to the depth of investigation before useful measurements can be made on reasonable timescales; in this case, CSAMT may be a more suitable sounding method. The EMI from the platform is therefore the critical factor affecting noise and hence the success of a compact TDEM sounder. EMI from eddy currents in the platform is another issue (see below). Platform EMI could also affect natural-source measurements, so in either case it would be advisable to deactivate nonessential subsystems during EM measurements and to provide a modest separation between receivers and the platform. It may be necessary to alternate TDEM with other activities anyway, as the TDEM itself will generate strong EMI for the rest of the platform.

[110] If deep sounding to detect water at a depth of several kilometers is desired, the compact transmitter would likely have to be abandoned in favor of a large loop. Surface mobility in the 2007 generation of rovers is expected to be in the range of several kilometers. Therefore a fixed path of, say, 400 m (to lay out a square loop 100 m in diameter) would require dedicating only a small fraction of total mission mobility. Alternatively, it may be possible to pyrotechnically deploy a square or triangular loop of this dimension; recall that the results are relatively insensitive to loop shape, although the loop efficiency is optimized with a circular loop. A system with a 100-m, single-turn, 1-A transmitter loop can detect water under low-noise conditions to depths approaching 4 km with a half sol of integration. Under terrestrial-noise conditions the half-sol estimate is just 800 m. The mass and power of the large loop are not very different from those of the compact loop, but the system is much more efficient because of the large transmitter area. Increased margin can be obtained by increasing the output of the loop to, say, 20 amp-turns (~25 kg, 150 W), which nearly triples the exploration depths. These latter figures obviously place much larger demands on mission resources.

[111] These calculations provide simple proof of concept for Mars TDEM sounders. Long integration times are the simplest way to avoid high mass and logistical problems but may constrain mission operations, particularly through TDEM-generated EMI. The EMI from the platform to the TDEM must also be assessed. Other design considerations include transmitter-receiver separation (to eliminate sensitivity to soil magnetic polarization), period and waveform of the transmitted pulse, control of transmitter turnoff time, and the number, location, and width of receiver gates. All told, a compact system with a mass of several kilograms and power consumption of several watts should be capable of detecting and characterizing water to distances of up to several hundred meters, and a system of perhaps several tens of kilograms and 100 W could detect water to a depth of several kilometers.

8.2.4. Platform induction. [112] EM receivers are generally located as far as practical from support equipment (e.g., in towed airborne "birds"), but relatively close platform proximity may be unavoidable in some Mars-exploration scenarios. The primary magnetic field will induce eddy currents in metallic closed paths on the platform, such as wiring, electronics boxes, structures and mechanisms, and foil insulation. The secondary fields from these conductors can completely obscure the ground response. Partial remedies include twisting wire pairs, restricting the dimensions of any closed current path (inserting insulating spacers, eliminating large closed loops), and substitution of dielectrics for metal as much as possible. Qualitatively, smaller metal components will have both smaller induction amplitudes and faster decay rates, hence the value of dielectric separation. Nonetheless, it will probably be necessary to measure the response of the platform to the sounder and subtract this self-response from the received signal, as must be done for some compact TDEM equipment [*Grimm et al.*, 1997]. This can be done prior to launch and in situ with low-amplitude pulses.

[113] An order-of-magnitude estimate of the minimum separation between receiver and platform can be made by considering the eddy currents induced in a hollow sphere [see *Ward and Hohmann*, 1988]. Receiver separations of order several meters appear to be sufficient, assuming that metal components are of order 10 cm in diameter and 1 mm thick, that the transmitter is ~1–2 m away from these components, and that the subsurface response can be extracted from 20–40 dB of coherent platform noise. As the secondary magnetic field of a compact target falls off at least as $1/d^6$, great improvements are possible with relatively small separations. For the deep sounder the recommended central-loop design can be adapted to minimize platform induction.

8.2.5. Nuclear magnetic resonance. [114] EM methods have been demonstrated in this paper to be very sensitive to water in an otherwise dry Martian crust, but it was also noted that humid clays or conductive iron oxides could also give strong responses that could also be confused with water. The only

geophysical method that can unambiguously detect liquid water is nuclear magnetic resonance (NMR), which exploits excitation and measurement of nuclear precession at a specific Larmor frequency for hydrogen in water. The technique relies on a background field to provide a reference direction about which nuclear magnetic moments precess and a transient orthogonal field to tip the moments out of equilibrium. The subsequent precession and decay is observed from the changing magnetic field. Borehole NMR has been very successful because, like its medical counterpart, strong permanent magnets provide high bulk nuclear magnetic moment and hence high signal. Surface-deployed NMR uses the planet's static magnetic field as the reference [*Goldman et al.*, 1994; *Trushkin et al.*, 1995; *Weichman et al.*, 1999], and a loop for the transient field. The method thus shares many operational characteristics with TDEM, and indeed, the data can be considered jointly [*Goldman et al.*, 1994]. The principal difference is that the NMR system is operated only at the Larmor frequency, which must be determined in situ. However, the millionfold or greater reduction in the reference field from medical and borehole applications yields only very small signals, and so reliable, widespread application has been elusive. On Mars, NMR could probably be tested only in the presence of relatively strong magnetic fields at the surface, likely at a major magnetic anomaly. Even then, subsurface transient fields of $\sim 10^{-7}$ T necessary to strongly tip protons would require hundreds amp-turns in a 100-m loop to detect water at <100 m depth. Deeper exploration is achieved most simply by increasing the loop size to maintain the same tipping geometry and increasing the pulse duration. In order to probe to depths of hundreds of meters, a very large loop, high power, and long integration times would be called for in the standard practice. Alternative solutions to these large resource requirements have not been demonstrated for terrestrial exploration, and so surface NMR for deep groundwater exploration on Mars is not forthcoming.

9. Discussion: Instruments and Platforms

9.1. Magnetic Field Sensors

[115] The most widely used sensor for measurement of magnetic fields from spacecraft is the fluxgate magnetometer. This robust instrument, dating from WW II, measures the ambient vector field from differences in the saturation of ferrite cores under imposed equal and opposite magnetizing fields (see *Campbell* [1997] for a review). The latter are produced by windings around the cores, and as the driving current is usually switched at frequencies ranging from hundreds of hertz to a kilohertz or so, the upper limit to frequency measurement of a fluxgate is typically 10–100 Hz, although some commercial fluxgates have bandwidths up to several kHz (e.g., Bartington Instruments, http://www.bartington.-com, 2001). If aquifers on Mars are briny, the models presented here indicate that some of the diagnostic information on aquifer depth and conductance (thickness) could be inferred from frequencies <10 Hz, using standard fluxgate magnetometers in spatial arrays (GDS) or in combination with electric field measurements (MT). The higher-frequency band in which fresher water must be distinguished will not be visible to most fluxgates, particularly if such water is shallowly distributed. Fluxgate magnetometers for space exploration typically have masses of order 1 kg and power consumption of order 1 W. Compact fluxgates manufactured for surveillance have masses of a few tens of grams and require a few tens of milliwatts, but performance is about an order of magnitude poorer.

[116] In practice, fluxgates are generally not used for EM measurements on Earth because of their relatively high noise floor; instead, induction coils are the norm for broadband measurement of time-varying fields. The linear $B(f)$ response of an induction coil can be flattened by incorporating a feedback loop, thus converting the sensor to a magnetic antenna. A few different, specialized coils can span the frequency range 10^{-5} to 10^{5} Hz and measure essentially all useful natural energy in this band. Magnetic antennae for terrestrial EM exploration have masses of a few to several kilograms and consume several hundred milliwatts: clearly, there are significant mass costs to improved performance. Coils, too, can be made more compact, again at the price of reduced performance [e.g., *Becker*, 1967].

[117] There are numerous other sensors to measure magnetic fields, but these are either unsuited to space exploration or are not yet at the necessary technology readiness. Proton or alkali-vapor magnetometers are also relatively large and power-consumptive yet measure only the total field, not its vector components. Superconducting quantum interference devices (SQUIDs) have the lowest noise floor but require bulky refrigerated dewars. Lorenz-deflection magnetometers also use an AC drive signal that limits bandwidth.

[118] One technology that shows promise for making broadband measurements with a compact sensor is magnetoresistance, in which the resistance of thin layered films varies with the vector magnetic field. So-called giant magnetoresistance (GMR) devices are now commonly used in industry, particularly in disk-drive read/write heads. Better performance, however, is achieved using spin-dependent tunneling (SDT) [e.g., *Moodera et al.*, 1999]. These devices minimally consist of two ferromagnetic thin films separated by a very thin insulating barrier. A voltage is applied across the stack, and current flows across the barrier by quantum-mechanical tunneling. When the layer magnetizations are aligned by the ambient magnetic field, electron-spin alignment allows a larger current to flow than when the fields are antialigned. Under intermediate states a near-linear relation exists between resistance and the ambient field in the direction parallel to the ferromagnetic magnetization axis. Partially under a grant to Blackhawk Geoservices from the NASA Planetary Instrument Definition and Development Program (PIDDP), Nonvolatile Electronics, Inc., has developed a generation of SDT sensors with low-frequency performance comparable to a compact (surveillance) fluxgate but with a noise floor of 10 pT/$\sqrt{\text{Hz}}$ extending to as high as 100 kHz (M. Tondra, personal communication, 2000). This is still a few orders of magnitude poorer than standard magnetic antennae; while SDTs may soon perform comparably to full-sized fluxgates (with much lower mass and power requirements (10 g, 10s mW)), it is unclear if they will be able to replace induction coils for low-field measurements.

9.2. Electric Field Sensors

[119] Electric field measurements for geophysical EM sounding are usually made with grounded electric dipoles, using either metal rods or an electrolyte in a porous pot. As the contact impedance can be very large indeed even for dry ground on Earth, purely galvanic measurements will be impractical on Mars. At higher resistance, capacitative coupling between the lead wires and the ground also becomes significant. Actively driven electrodes are therefore necessary under conditions of high contact impedance on Earth [e.g., *Wannamaker et al.*, 1996], and improvements to this technique have recently been made under the same PIDDP sponsorship by Geometrics, Inc. (J. Johnston, personal communication, 2000).

[120] Dipole antennae have been used to measure ambient electrical fields in airborne systems to frequencies as low as ~10 Hz (A. Barringer, personal communication, 2000), albeit with low efficiency because the antenna length is far below its resonant value. High-altitude near-DC measurements are commonly performed using a double Langmuir probe; indeed, the electrical conductivity of Earth's stratosphere is comparable to that of the lower atmosphere of Mars [*Cummer and Farrell*, 1999; *Delory et al.*, 2001]. However, this sensor also functions as a capacitatively coupled short antenna up to VLF [*Holzworth and Bering*, 1998]. New high-impedance, low-capacitance pre-amps promise to

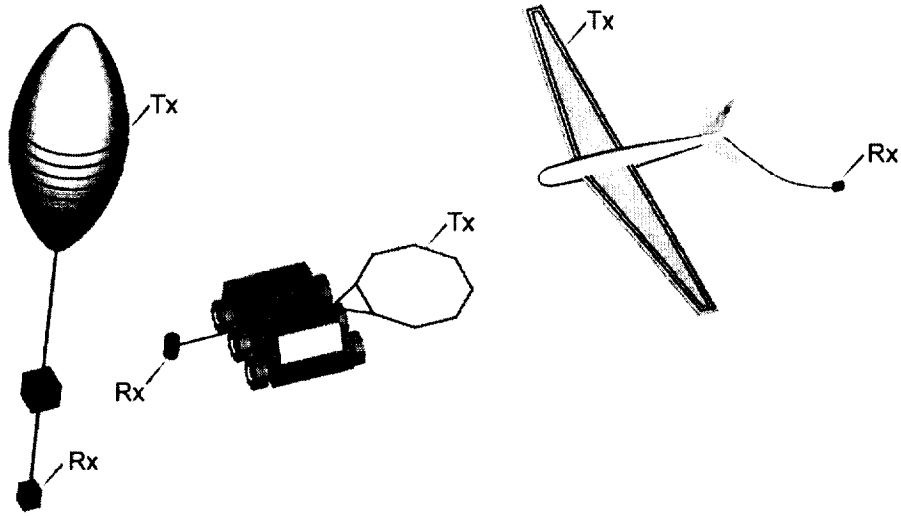

Figure 16. Low-frequency EM platform concepts for Mars. Separation of the sensors from platform noise is desirable for either natural- or artificial-source soundings. Receivers are best located in a separate "bird" for airborne platforms. For a rover or fixed ground station a boom may not provide sufficient isolation; detachment or ballistic deployment may be necessary. Transmitter coils for active airborne soundings can be accommodated by wrapping wire around balloon itself or airplane wings; loop on rover or ground station can be inflatable. Also, rover could lay out large loop for deep sounding.

improve both the bandwidth and noise floor of such measurements (G. Delory, personal communication, 2001).

9.3. Mission Scenarios

[121] Plausible missions involving geophysical investigations of the subsurface may be grouped into three categories: (1) single-station lander, (2) multiple, networked landers, and (3) single airborne vehicles. For each geometry, both natural- and artificial-source methods, including electric and/or magnetic field measurements, can be considered.

[122] Single-station landers, possibly with rovers, are most attractive in terms of overall resource allocation and consistency with the current Mars Program. Among the passive methods, measurement of the electric field wave tilt would be the simplest, requiring only a three-component dipole antenna. The ESA Netlanders will measure the vertical E field over a broad range of frequencies (J. Berthelier, personal communication, 2001). Without the horizontal components, there is no sounding capability, but the experiment will doubtless provide pioneering information on natural electromagnetic fields at the Martian surface.

[123] As magnetometers will likely be included in many single-station scenarios, a combined magnetotelluric and wave-tilt experiment would provide complementary information both on the nature of natural fields and on sounding. Recall that single-station magnetometers cannot provide soundings without E field measurements, so the electric field system should add the vertical component and thus provide an independent sounding through wave tilt. The horizontal components of E and H are used for the principal MT results; the cross spectra and vertical H field yield important information on lateral heterogeneity. The key constraint is bandwidth compatibility between the magnetic and electric field sensors and the ultimate constraints implied by source structure.

[124] As described above, TDEM is the only artificial-source method for which the transmitter and receiver can be closely spaced and still provide relatively deep soundings. For shallow soundings (to hundreds of meters' depth), both the transmitter and receiver would optimally be rover-mounted, although both could be fixed to the lander if resources were more limited. The rover configuration will ultimately need the most structures-and-mechanisms engineering because it would probably require both transmitter and receiver that can be repeatedly deployed and stowed. For the transmitter coil a polygonal configuration of flexible "shock poles" (Figure 16) could be either completely restowed or simply rotated to the vertical plane for travel. Inflation and deflation of a balloon coil is also possible. Alternatively, if the rover is relatively large and greater simplicity is desired, then expendable transmitter coils could simply be detached when the rover is ready to move. As discussed above, it may be advisable to attempt to isolate the receiver from the rover; this could be accomplished by a moveable boom or by detaching the receiver and temporarily moving away from it. In the latter case, data and power could be relayed by a hard wire, or the sensor could be self-powered and communicate with the rover by radio link. Layout of a large loop necessary for deep TDEM sounding is well within the expected capability of the upcoming generation of rovers. The main difficulties are spooling out a wire on a closed path over rough terrain and remote (central) deployment of the receiver.

[125] A network of landers could use any of the above techniques to map lateral heterogeneity. The wave-tilt method is again probably the most compact. Alternatively, a simple one-dimensional sounding can be made using magnetometers only. The key constraint is that the stations are numerous and close enough that horizontal wavelengths can be measured. The ESA Netlanders intend to perform GDS, but with just a few stations separated by large distances (>1000 km), only the diurnal wave can be minimally sampled and lateral heterogeneity on this scale could influence interpretation of the soundings. In this case, comparative modeling must be performed, in which one station is chosen as a reference and assigned a conductivity structure. Even so, the response of their fluxgate magnetometers is limited to <10 Hz, which will limit the range of salinity, depth, and thickness of aquifers to which the instruments are sensitive. Because the relatively large number and density of stations required for GDS, this method is not very practical compared to other approaches.

[126] Airborne platforms provide spatial coverage of at least part of a network from a single station. Because of the continuity of

tangential E and H fields at the planetary surface, natural-source soundings can be performed in the air as long as the free-space wavelength is large compared to the altitude. This holds for all but the highest frequencies considered here (>10 kHz) at high altitudes (10 km). Wave-tilt methods were originally developed for airborne exploration. Airplanes are more targetable and may have higher payloads than balloons but will also be significantly noisier. A towed "bird" to separate the sensors from the airframe is almost always used in terrestrial airborne EM and would likely be an important consideration in design of Mars airplanes (Figure 16). Wingtips are probably the next best place, with either the nose or tail (whichever is farthest from the motor) as the third choice for sensor mounting. EM instruments might be configurable on a balloon gondola, but a dedicated bird or subgondola would be optimal.

[127] Artificial sources have been used on both balloons and airplanes; the fixed-wing INPUT system is in indeed widely considered to be the most successful EM system ever. The transmitter is wrapped around the wings (Figure 16) and the receiver is towed in a bird. For a balloon the transmitter consists of a number of turns of thin, flexible wire around the balloon itself. Airborne systems require additional margin in the sounder design, as altitudes of order 1 km must be factored in. Alternatively, a montgolfiere balloon would land at night, allowing measurements to be made closer to the target.

10. Conclusion

[128] Low-frequency electromagnetic sounding has both high sensitivity to groundwater and flexible implementation. Sensor systems for natural-source soundings are relatively compact and can be used in single or networked stations. Although there is probably little doubt that natural time-varying EM signals are present at the surface of Mars, their exact nature, occurrence, and distribution will be important to the amount of information on subsurface water that can be recovered. Artificial-source methods eliminate this uncertainty at increased cost in mass and power, but plausible scenarios for both shallow and deep sounding will not tax their appropriate mission classes. For example, the shallow sounder could be accommodated on a variety of "Scout" platforms, whereas the deep sounder would be a small fraction of the heavy landed payloads now under consideration.

[129] Understanding the electromagnetic properties of Martian crustal materials is key to successful experiment design and interpretation. If improperly modeled, adsorbed water in the cryosphere could lead to erroneous conclusions about the "depth to water" (although aquifer thickness may be discernable at yet lower frequencies). Iron oxides or "stealth" material may cause additional crustal conductivity and dispersion.

[130] Because one or more spacecraft carrying orbital sounding radars will launch for Mars in the near future (Mars Express, 2003; Mars Reconnaissance Orbiter, 2005), some inferences about the presence or absence of water on Mars will likely be made by the time low-frequency experiments can be deployed. Low-frequency methods will be complementary to radar. Unambiguous identification of H_2O from radar will occur only for saturated, high-porosity aquifers or massively segregated ground ice [*Beaty et al.*, 2001]; elsewhere, such identification will be largely interpretative and require "ground truth" from other methods. As the low-frequency methods cannot be used from orbit but provide robust sounding capability, they are the natural follow-up to orbital radars in the search for water on Mars.

Notation

a	transmitter diameter, m.
b	TDEM parameter $2/\mu S$, 1/s.
$A_1, A_2, \ldots$	coefficients for electrical conductivity, S/m.
A_s	specific surface area, m^2/g.
B	magnetic induction, T.
B_0	TDEM noise floor, T.
c	speed of light, m/s.
C	concentration of dissolved solids, g/L.
d	distance or height, m.
d_w	diameter of H_2O molecule, Å.
E	electric field strength, V/m.
f	frequency, Hz.
f_T	TDEM transmitter pulse frequency, Hz.
f_c	waveguide cutoff frequency, Hz.
h	layer thickness, m.
H	magnetic field strength, A/m.
I	TDEM transmitter current, A.
k	wave number, 1/m.
k	Boltzmann's constant
k_m	magnetic susceptibility.
n_{ac}	frequency coefficient for AC conductivity of rock.
N_m	number of adsorbed H_2O monolayers.
m	exponent for Archie's law.
m_w	mass of water molecule, g.
M_T	transmitter moment, $A\text{-}m^2$.
M_R	receiver moment, m^2.
R	reflection coefficient.
S	conductance of a plate, S.
SNR	signal-to-noise (amplitude) ratio, dimensionless.
t	time, s.
t_0	TDEM signal-integration time, s.
T	temperature, K.
$Q_1, Q_2, \ldots$	activation energies for electrical conductivity, eV.
V	EMF, V.
V_u	unfrozen water volume fraction.
W_u	unfrozen water weight fraction.
Z, Z_0	impedance, impedance of free space, ohms.
α	MBLM mixing-law coefficient.
γ	amplitude coefficient for Archie's law, S/m.
δ	skin depth, m.
Δ	TDEM receiver-gate width, s.
$\varepsilon, \varepsilon_0$	electrical permittivity, permittivity of free space.
ε_r	relative electrical permittivity or dielectric constant.
$\varepsilon_I, \varepsilon_{rI}$	electrical permittivity, dielectric constant of ice.
$\varepsilon_{rI}^{0}, \varepsilon_{rI}^{\infty}$	zero- and infinite-frequency dielectric constants of ice.
$\varepsilon_W, \varepsilon_{rW}$	electrical permittivity, dielectric constant of water.
η, η_0	intrinsic impedance, impedance of free space, ohms.
μ, μ_0	magnetic permeability, permittivity of free space.
ν	TDEM noise bandwidth, Hz.
ω	angular frequency, 1/s.
ϕ	porosity, dimensionless.
ρ_a	apparent resistivity, ohm-m.
ρ_s	density of soil, g/cm^3.
σ	electrical conductivity, S/m.
σ'	background-normalized conductivity, dimensionless.
σ_I	electrical conductivity of ice, S/m.
σ_R	electrical conductivity of rock, S/m.
σ_{Rdc}	DC conductivity of rock, S/m.

σ_{Rac}	AC conductivity of rock, S/m.
σ_W	electrical conductivity of water, S/m.
σ_{WR}	electrical conductivity of
ψ	relative saturation of pore space, dimensionless.
τ	RC time constant for TDEM gate integrator, s.
τ_I	relaxation time for ice, s.

[131] **Acknowledgments.** I thank Mark Blohm, Gary Olhoeft, Roger Phillips, George Jiracek, Mike Mellon, Janet Luhmann, Jack Connerney, Mario Acuña, and Greg Delory for helpful discussions on TDEM, electrical properties, magnetotellurics, Martian ice, space physics, and magnetometer and electrometer design. I am also grateful to my PIDDP colleagues Mark Tondra, Cathy Nordman, Dan Reed, Jeff Johnston, and Ken Smith for their engineering expertise. Rand Donohoo and Herman Vialpando contributed to the figures. This work was supported by the NASA Planetary Instrument Definition and Development Program under contract NASW-98109.

References

Acuña, M., et al., Global distribution of crustal magnetization discovered by the Mars Global Surveyor MAG/ER experiment, *Science*, *284*, 790–793, 1999.

Anderson, D. M., and A. R. Tice, Predicting unfrozen water contents in frozen soils from surface measurements, *Highway Res. Res.*, *373*, 12–18, 1972.

Anderson, D. M., and A. R. Tice, The unfrozen interfacial phase in frozen soil water systems, in *Ecological Studies: Analysis and Synthesis*, vol. 4, pp. 107–124, Springer-Verlag, New York, 1973.

Anderson, D. M., E. S. Gaffney, and P. F. Low, Frost phenomena on Mars, *Science*, *155*, 319–322, 1967.

Ballou, E. V., P. C. Wood, T. Wydeven, M. E. Lehwalt, and R. E. Mack, Chemical interpretation of Viking 1 life detection experiment, *Nature*, *352*, 589–594, 1978.

Bandfield, J. L., V. E. Hamilton, and P. R. Christensen, A global view of Martian surface compositions from MGS-TES, *Science*, *287*, 1626–1630, 2000.

Beaty, D., S. Clifford, P. Gogineni, R. Grimm, C. Leuschen, G. Olhoeft, K. Raney, and A. Safaeinili, *Report of the Virtual Instrument Science Definition Team on the Facility Orbital Radar Sounder Experiment for MRO 2005*, JPL White Paper, Jet Propul. Lab., Pasadena, Calif., 2001.

Becker, A., Design formulas for electromagnetic sensing coils, *Geoexploration*, *5*, 81–88, 1967.

Becker, A., and G. Cheng, Detection of repetitive electromagnetic signals, in *Electromagnetic Methods in Applied Geophysics*, vol. 1, *Theory*, edited by M. N. Nabighian, pp. 443–466, Soc. Explor. Geophys., Tulsa, Okla., 1988.

Berryman, J. G., Mixture theories for rock properties, in *A Handbook of Physical Constants*, edited by T. J. Ahrens, pp. 205–228, AGU, Washington, D. C., 1995.

Blacic, J. D., D. S. Dreesen, and T. Mockler, Report on conceptual systems analysis of drilling systems for 200-m depth penetration and sampling of the Martian subsurface, Los Alamos Natl. Lab., Los Alamos, N. M., 2000. (Available at http://www.ees4.lanl.gov/mars)

Blackhawk Geoservices Inc., *Evaluation of a Prototype Transient Sounding System, Proj. 9603 EOD*, Golden, Colo., 1999.

Buselli, G., The effect of near-surface superparamagnetic material on electromagnetic measurements, *Geophysics*, *47*, 1315–1324, 1982.

Brass, G. W., Stability of brines on Mars, *Icarus*, *42*, 20–28, 1980.

Campbell, W., *Introduction to Geomagnetic Fields*, 290 pp., Cambridge Univ. Press, New York, 1997.

Carr, M. H., *Water on Mars*, 229 pp., Oxford Univ. Press, New York, 1996.

Christiansen, P. R., et al., Detection of crystalline hematite mineralization on Mars by the Thermal Emission Spectrometer: Evidence for near-surface water, *J. Geophys. Res.*, *105*, 9623–9642, 2000.

Clark, B. C., A. K. Baird, R. J. Weldon, D. M. Tsusaki, L. Schnabel, and M. P. Candelaria, Chemical composition of Martian fines, *J. Geophys. Res.*, *87*, 10,059–10,067, 1982.

Clifford, S. M., A model for the hydrologic and climatic behavior of water on Mars, *J. Geophys. Res.*, *98*, 10,973–11,065, 1993.

Clifford, S. M., and D. Hillel, The stability of ground ice in the equatorial regions of Mars, *J. Geophys. Res.*, *88*, 2456–2474, 1983.

Chyba, C. F., S. J. Ostro, and B. C. Edwards, Radar detectability of a subsurface ocean on Europa, *Icarus*, *134*, 292–302, 1998.

Cummer, S. A., and W. M. Farrell, Radio atmospheric propagation on Mars and potential remote sensing applications, *J. Geophys. Res.*, *104*, 14,149–14,157, 1999.

Davis, S. S., and R. J. M. DeWeist, *Hydrogeology*, John Wiley, New York, 1966.

Delory, G. T., W. M. Farrell, and M. D. Desch, A global electric circuit on Mars (abstract), *Lunar Planet. Sci.*, *XXXII*, 2150, 2001.

Dunlop, D. J., Theory of the magnetic viscosity of lunar and terrestrial rocks, *Rev. Geophys.*, *11*, 855–901, 1973.

Eden, H. F., and B. Vonnegut, Electrical breakdown caused by dust motion in low-pressure atmospheres: Considerations for Mars, *Science*, *180*, 962–963, 1973.

Fanale, F. P., J. R. Salvail, A. P. Zent, and S. E. Postawko, Global distribution and migration of subsurface water on Mars, *Icarus*, *67*, 1–18, 1986.

Fanale, F. P., S. E. Postawko, J. B. Pollack, M. H. Carr, and R. O. Pepin, Mars: Epochal climate change and volatile history, in *Mars*, edited by H. H. Kieffer et al., pp. 1180–1220, Univ. of Ariz. Press, Tucson, 1992.

Farrell, W. M., M. L. Kaiser, M. D. Desch, J. G. Houser, S. A. Cummer, D. M. Wilt, and G. A. Landis, Detecting electrical activity from Martian dust storms, *J. Geophys. Res.*, *104*, 3795–3802, 1999.

Ferguson, D. C., J. C. Kolecki, M. W. Siebert, D. W. Wilt, and J. R. Matijevic, Evidence for Martian electrostatic charging and abrasive wheel wear from the Wheel Abrasion Experiment on the Pathfinder Sojourner rover, *J. Geophys. Res.*, *104*, 8747–8760, 1999.

Goldman, M., B. Rabinovich, M. Rabinovich, D. Gilad, I. Gev, and M. Schirov, Application of the integrated NMR-TDEM method in groundwater exploration in Israel, *J. Appl. Geophys.*, *31*, 27–52, 1994.

Gough, D. I., and M. R. Ingham, Interpretation methods for magnetometer arrays, *Rev. Geophys.*, *21*, 805–827, 1983.

Grimm, R. E., M. W. Blohm, and E. M. Lavely, UXO characterization using multicomponent, multichannel time-domain electromagnetic induction, *UXO Forum 97*, pp. 134–143, Dep. of Def. Explos. Safety Board, Alexandria, Va., 1997.

Grimm, R. E., H. B. Lynn, C. R. Bates, D. R. Phillips, K. M. Simon, and W. E. Beckham, Detection and analysis of naturally fractured gas reservoirs: Multiazimuth surveys in the Wind River basin, Wyoming, *Geophysics*, *64*, 1277–1292, 1999.

Hanson, W. B., S. Sanatani, and D. R. Zuccaro, The Martian ionosphere as observed by the Viking retarding potential analyzers, *J. Geophys. Res.*, *82*, 4352–4363, 1977.

Hashin, Z., and S. Shtrikman, A variational approach to the theory of effective magnetic permeability of multiphase materials, *J. Appl. Phys.*, *33*, 3125–3131, 1962.

Hoffman, N., White Mars: A new model for Mars' surface and atmosphere based on CO_2, *Icarus*, *146*, 326–342, 2000.

Holzworth, R. H., and E. A. Bering, Ionospheric electric fields from stratospheric balloon-borne probes, in *Measurement Techniques in Space Plasmas: Fields*, *Geophys. Monogr. Ser.*, vol. 103, edited by R. F. Pfaff, J. E. Borovsky, and D. T. Young, pp. 79–84, AGU, Washington, D. C., 1998.

Jiracek, G. R., V. Haak, and K. H. Olsen, Practical magnetotellurics in a continental rift environment, in *Continental Rifts: Evolution, Structure, and Tectonics*, edited by K. H. Olsen, pp. 103–129, Elsevier Sci., New York, 1995.

Kaufman, A. A., *Geophysical Field Theory and Mmethod, Part C, Electromagnetic Fields II*, 332 pp., Academic, San Diego, 1994.

Keller, G. V., Electrical properties of rocks and minerals, in *CRC Handbook of Physical Properties of Rocks*, vol. I, pp. 217–293, CRC Press, Boca Raton, Fla., 1982.

Keller, G. V., Rock and mineral properties, in *Electromagnetic Methods in Applied Geophysics*, vol. 1, *Theory*, edited by M. N. Nabighian, pp. 13–52, Soc. Explor. Geophys., Tulsa, Okla., 1988.

Khurana, K. K., and 6 others, Induced magnetic fields as evidence for subsurface oceans in Europa and Callisto, *Nature*, *395*, 777–780, 1998.

Kieffer, H. H., and A. P. Zent, Quasi-periodic climate change on Mars, in *Mars*, edited by H. H. Kieffer et al., pp. 1180–1220, Univ. of Ariz. Press, Tucson, 1992.

Kivelson, M. G., Pulsations and magnetohydrodynamic waves, in *Introduction to Space Physics*, edited by M. G. Kivelson and C. T. Russell, pp. 330–355, Cambridge Univ. Press, New York, 1995.

Luhmann, J. G., The intrinsic magnetic field and solar-wind interaction of Mars, in *Mars*, edited by H. H. Kieffer et al., pp. 1090–1134, Univ. of Ariz. Press, Tucson, 1992.

Luhmann, J. G., C. T. Russell, F. L. Scarf, L. H. Brace, and W. C. Knudsen, Characteristics of the Mars-like limit of the Venus solar-wind interaction, *J. Geophys. Res.*, *92*, 8455–8557, 1987.

Madden, T., and P. Nelson, A defense of Cagniard's magnetotelluric method, in *Magnetotelluric Methods*, edited by K. Vozoff, pp. 89–102, Soc. Explor. Geophys., Tulsa, Okla., 1985.

Madsen, M. B., S. F. Hviid, H. P. Gunnlaugsson, J. M. Knudsen, W. Goetz, C. T. Pedersen, A. R. Dinesen, C. T. Mogensen, and M. Olsen, The magnetic properties experiments on Mars Pathfinder, *J. Geophys. Res.*, *104*, 8761–8780, 1999.

Malin, M. C., and K. S. Edgett, Evidence for recent groundwater seepage and surface runoff on Mars, *Science*, *288*, 2330–2335, 2000.

Mavko, G., T. Mukerji, and J. Dvorkin, *The Rock Physics Handbook*, 329 pp., Cambridge Univ. Press., New York, 1998.

McDermott, J. K., Power, in *Space Mission Analysis and Design*, 2nd ed., edited by W. J. Larson and J. R. Wertz, pp. 391–409, Microcosm/Kluwer, Torrance, Calif., 1992.

McNeill, J. D., Use of electromagnetic methods for groundwater studies, in *Geotechnical and Environmental Geophysics*, vol. 1, *Review and Tutorial*, edited by S. H. Ward, pp. 191–218, Soc. Explor. Geophys., Tulsa, Okla., 1990.

McNeill, J. D., and V. F. Labson, Geological mapping using VLF radio fields, in *Electromagnetic Methods in Applied Geophysics*, vol. 2, *Application*, edited M. N. Nabighian, pp. 521–640, Soc. Explor. Geophys., Tulsa, Okla., 1991.

McSween, H. Y., Jr., et al., Chemical, multispectral, and textural constraints on the composition and origin of rocks at the Mars Pathfinder landing site, *J. Geophys. Res.*, *104*, 8679–8716, 1999.

Mellon, M. T., and R. J. Phillips, Recent gullies on Mars and the source of liquid water, *J. Geophys. Res.*, *106*, 23,165–23,179, 2001.

Mars Exploration Program/Payload Analysis Group (MEPAG), *Science Planning for Exploring Mars, Part 2: Scientific Goals, Objectives, and Priorities*, edited by R. Greeley, *JPL Publ. 01-7*, Jet Propul. Lab., Pasadena, Calif., 2001.

Moodera, J. S., J. Nassar, and G. Mathon, Spin tunneling in ferromagnetic junctions, *Annu. Rev. Mater. Sci.*, *29*, 381–432, 1999.

Muhleman, D. O., B. J. Butler, A. W. Grossman, and M. A. Slade, Radar images of Mars, *Science*, *253*, 1508–1513, 1991.

Nabighian, M. N., Quasi-static transient response of a conducting half-space: An approximate representation, *Geophysics*, *44*, 1700–1705, 1979.

Olhoeft, G. R., Effects of water on the electrical properties of planetary regoliths, in *Proceedings of the Colloquium on Water in Planetary Regoliths*, pp. 139–142, U.S. Army Cold Reg. Res. Lab., Hanover, N. H., 1976.

Olhoeft, G. R., Electrical properties of a natural clay permafrost, *Can. J. Earth Sci.*, *14*, 16–24, 1977.

Olhoeft, G. R., Low-frequency electrical properties, *Geophysics*, *50*, 2492–2503, 1985.

Olhoeft, G. R., Ground penetrating radar on Mars, in *Proceedings of the Seventh International Conference on Ground Penetrating Radar*, pp. 387–392, Univ. of Kansas, Lawrence, 1998.

Olhoeft, G. R., and D. W. Strangway, Magnetic relaxation and the electromagnetic response parameter, *Geophysics*, *39*, 302–311, 1974.

Palacky, G. J., and G. F. West, Airborne electromagnetic methods, in *Electromagnetic Methods in Applied Geophysics*, vol. 2, *Application*, edited by M. N. Nabighian, pp. 811–879, Soc. Explor. Geophys., Tulsa, Okla., 1991.

Partzsch, G. M., F. R. Schilling, and J. Arndt, The influence of partial melting on the electrical behavior of crustal rocks: Laboratory examinations, model calculations, and geological interpretations, *Tectonophysics*, *317*, 189–203, 2000.

Phillips, R. J., et al., Apollo lunar sounder experiment, in *Apollo 17 Preliminary Science Report*, *NASA Spec. Publ.*, *NASA SP-330*, chap. 22, 22-1 to 22-26, 1974.

Rawer, K., *Wave Propagation in the Ionosphere*, 486 pp., Kluwer Acad., Norwell, Mass., 1993.

Rieder, R., T. Economou, H. Wänke, A. Turkevich, J. Crisp, J. Brückner, G. Dreibus, and H. Y. McSween Jr., The chemical composition of Martian soil and rocks returned by the mobile Alpha Proton X-ray Spectrometer: Preliminary results from the X-ray mode, *Science*, *278*, 1771–1774, 1997.

Russell, C. T., A brief history of solar-terrestrial physics, in *Introduction to Space Physics*, edited by M. G. Kivelson and C. T. Russell, pp. 1–26, Cambridge Univ. Press, New York, 1995.

Schubert, G., and K. Schwartz, A theory for the interpretation of lunar surface magnetometer data, *Moon*, *1*, 106–117, 1969.

Schubert, G., S. C. Solomon, D. L. Turcotte, M. J. Drake, and N. H. Sleep, Origin and thermal evolution of Mars, in *Mars*, edited by H. H. Kieffer et al., pp. 147–183, Univ. of Ariz. Press, Tucson, Okla., 1992.

Scott, W. J., P. V. Sellmann, and J. A. Hunters, Geophysics in the study of permafrost, in *Geotechnical and Environmental Geophysics*, vol 1, *Review and Tutorial*, edited by S. H. Ward, pp. 355–384, Soc. Explor. Geophys., Tulsa, Okla., 1990.

Singh, R. P., and T. Lal, Wave-tilt characteristics of TE-mode waves, *Can. J. Earth Sci.*, *18*, 382–385, 1981.

Soderblom, L. A., The composition and mineralogy of the Martian surface from spectroscopic observations: 0.3 μm to 50 μm, in *Mars*, edited by H. H. Kieffer et al., pp. 557–593, Univ. of Ariz. Press, Tucsona, 1992.

Spies, B. R., and F. C. Frischknecht, Electromagnetic sounding, in *Electromagnetic Methods in Applied Geophysics*, vol. 2, *Application*, edited by M. N. Nabighian, pp. 285–386, Soc. Explor. Geophys., Tulsa, Okla., 1991.

Sukhorukov, A. I., On the Schumann resonances of Mars, *Planet. Space Sci.*, *39*(12), 1673–1676, 1991.

Telford, W. M., L. P. Geldart, and R. E. Sheriff, *Applied Geophysics*, 2nd ed., 770 pp., Cambridge Univ. Press, 1990.

Trushkin, D. V., O. A. Shushakov, and A. V. Legchenko, Surface NMR applied to an electroconductive medium, *Geophys. Prospect.*, *43*, 623–633, 1995.

Uman, M., *Lightning*, 298 pp., Dover, Mineola, N. Y., 1969.

Vozoff, K., The magnetotelluric method, in *Electromagnetic Methods in Applied Geophysics*, vol. 2, *Application*, edited by M. N. Nabighian, pp. 641–711, Soc. Explor. Geophys., Tulsa, Okla., 1991.

Wait, J. R., Mutual electromagnetic coupling of loops over a homogeneous ground, *Geophysics*, *20*, 630–637, 1955.

Wait, J. R., Mutual electromagnetic coupling of loops over a homogeneous ground—An additional note, *Geophysics*, *21*, 479–484, 1956.

Wait, J. R., *Electromagnetic Waves in Stratified Media*, Pergamon, New York, 1970.

Wannamaker, P. E., J. A. Stodt, and S. L. Olsen, Dormant state of rifting below the Byrd Subglacial Basin, West Antarctica, implied by magnetotelluric (MT) profiling, *Geophys. Res. Lett.*, *23*, 2983–2986, 1996.

Ward, S. H., AFMAG—Airborne and ground, *Geophysics*, *24*, 761–789, 1959.

Ward, S. H., and G. W. Hohmann, Electromagnetic theory for geophysical applications, in *Electromagnetic Methods in Applied Geophysics*, vol. 1, *Theory*, edited by M. N. Nabighian, pp. 131–312, Soc. Explor. Geophys., Tulsa, Okla., 1988.

Ward, S. H., G. R. Jiracek, and W. I. Linlor, Electromagnetic reflection from a plane-layered lunar model, *J. Geophys. Res.*, *73*, 1355–1372, 1968.

Weichman, P. B., E. M. Lavely, and M. H. Ritzwoller, Surface nuclear magnetic resonance imaging of large systems, *Phys. Rev. Lett.*, *82*, 45–48, 1999.

Winn, W. P., G. W. Schwede, and C. B. Moore, Measurements of electric fields in thunderclouds, *J. Geophys. Res.*, *79*, 1761–1767, 1974.

Wolf, R. A., Magnetospheric configuration, in *Introduction to Space Physics*, edited by M. G. Kivelson and C. T. Russell, pp. 288–329, Cambridge Univ. Press, New York, 1995.

Zonge, K. L., and L. J. Hughes, Controlled source audio-frequency magnetotellurics, in *Electromagnetic Methods in Applied Geophysics*, vol. 2, *Application*, edited by M. N. Nabighian, pp. 713–809, Soc. Explor. Geophys., Tulsa, Okla., 1991.

Zuber, M. T., et al.,Internal structure and early thermal evolution of Mars from Mars Global Surveyor topography and gravity, *Science*, *287*, 1788–1793, 1999.

R. E. Grimm, Blackhawk Geoservices, Inc., 301 B Commercial Road, Golden, CO 80401, USA. (grimm@blackhawkgeo.com)

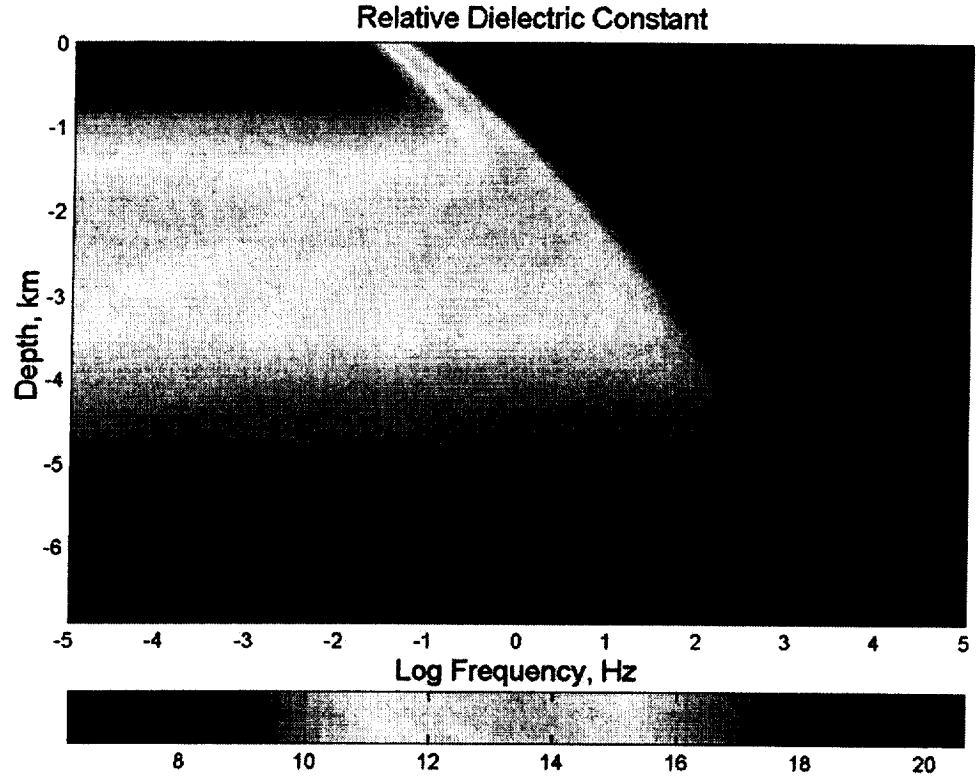
Relative Dielectric Constant
Depth, km
0
-1
-2
-3
-4
-5
-6
-5 -4 -3 -2 -1 0 1 2 3 4 5
Log Frequency, Hz
8 10 12 14 16 18 20

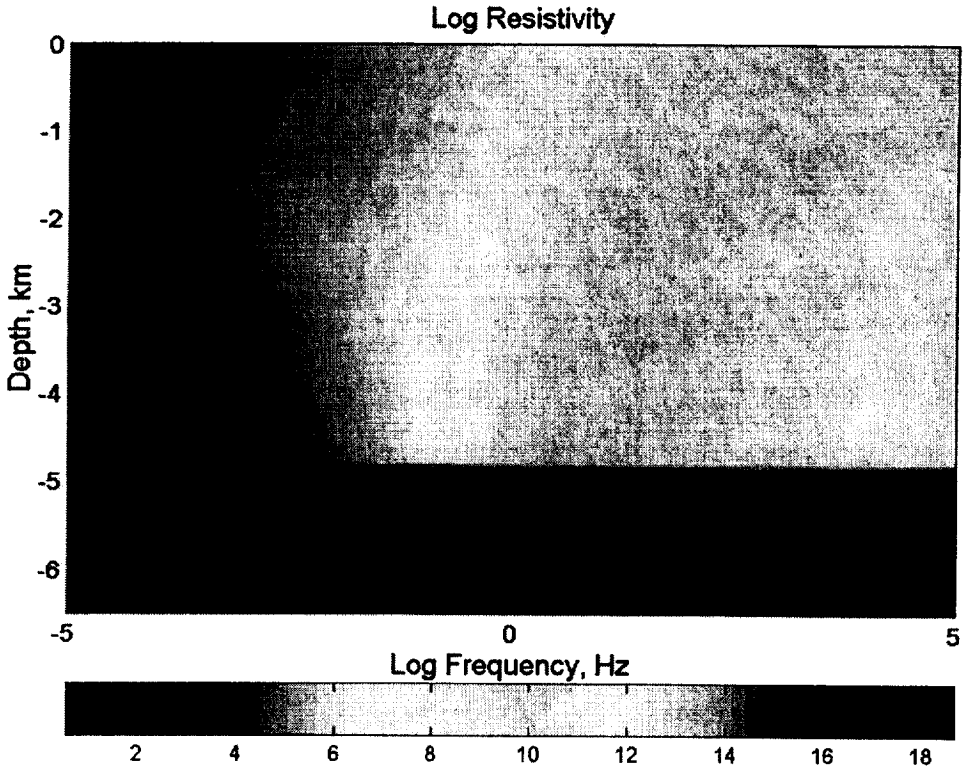
Log Resistivity
Depth, km
0
-1
-2
-3
-4
-5
-6
-5 0 5
Log Frequency, Hz
2 4 6 8 10 12 14 16 18

Figure 2. (top) Relative dielectric permittivity (dielectric constant) and (bottom) electrical conductivity for deep, briny aquifer (model 4c). Porosity decreases exponentially with depth and is everywhere saturated with ice or water; geothermal gradient is 15 K/km. The base of the cryosphere is formally at 6.2 km, but unfrozen water causes strong conductivity in the bottom kilometer of the cryosphere (note that dielectric contrast is modest). Relaxation loss in ice causes frequency- and temperature- (depth-)dependent transition between 0.01 Hz and 10 kHz.

REPORT DOCUMENTATION PAGE

Form Approved
OMB No. 0704-0188

1. AGENCY USE ONLY *(Leave blank)*	2. REPORT DATE	3. REPORT TYPE AND DATES COVERED
	28 JANUARY 2002	**FINAL: 28 JULY 1998 TO 27 JUL 2001**

4. TITLE AND SUBTITLE
SOLID-STATE MULTIMISSION MAGNETOMETER (SSM3): APPLICATION TO GROUNDWATER EXPLORATION ON MARS

5. FUNDING NUMBERS
NASW-98109

6. AUTHORS
DR. ROBERT E. GRIMM
PRINCIPAL INVESTIGATOR

7. PERFORMING ORGANIZATION NAME(S) AND ADDRESS(ES)
BLACKHAWK GEOSERVICES, INC.
301 B COMMERCIAL RD.
GOLDEN, C0 80401

8. PERFORMING ORGANIZATION REPORT NUMBER
9804-NAS-001

9. SPONSORING/MONITORING AGENCY NAME(S) AND ADDRESS(ES)
NATIONAL AERONAUTICS AND SPACE ADMINISTRATION
PLANETARY INSTRUMENT DEFINITION AND DEVELOPMENT PROGRAM
300 E STREET SW
WASHINGTON, DC 20546

10. SPONSORING/MONITORING AGENCY REPORT NUMBER

11. SUPPLEMENTARY NOTES

12a. DISTRIBUTION/AVAILABILITY STATEMENT

12b. DISTRIBUTION CODE

13. ABSTRACT *(Maximum 200 words)*

Report describes work to develop solid-state magnetometers using magnetoresistive thin films, low-frequency electric-field measurements, and methods for electromagnetic detection of water and ice in the subsurface of Mars.

14. SUBJECT TERMS
magnetometer, magnetic fields, electric fields, spacecraft, Mars

15. NUMBER OF PAGES
1

16. PRICE CODE

17. SECURITY CLASSIFICATION OF REPORT:	18. SECURITY CLASSIFICATION OF THIS PAGE:	19. SECURITY CLASSIFICATION OF ABSTRACT	20. LIMITATION OF ABSTRACT
UNCLASSIFIED	**UNCLASSIFIED**	**UNCLASSIFIED**	